UNIVERSITÀ DEGLI STUDI DI ROMA "TOR VERGATA"

DIPARTIMENTO DI FISICA

DOTTORATO DI RICERCA IN FISICA

PH.D. THESIS

Low energy electron and positron measurements in space with the **PAMELA** experiment

CANDIDATE:

Valeria Di Felice

SUPERVISOR:

Prof. Mirko Boezio

COORDINATOR:

Prof. Piergiorgio Picozza

A.A. 2009/10

Author's address:

Dipartimento di Fisica
Università degli Studi di Roma "TorVergata"
Via delle Ricerca Scientifica, 1
00133 Roma
Italia

Introduction

This thesis describes the study of electrons and positrons in the cosmic radiation. New measurements of the positron fraction at the top of the atmosphere between 200 MeV and 3.0 GeV are presented, together with the electron spectrum up to 20 GeV. The measurement was conducted with the space borne PAMELA experiment from July 2006 to December 2008, that is a period of minimum solar activity and negative solar magnetic field polarity. PAMELA provides the first long term observation of the low energy positron abundance during this particular solar and heliospheric state. The great amount of collected statistics allows to study the variation of the particle intensity at Earth with energy and time, and to investigate effects depending on the particles sign of charge. During approximately 860 days of data collection about 16300 positrons and 178000 electrons were identified. The major sources of background, constituted by cosmic protons and locally produced pions, have been studied. The derived electron spectrum clearly shows the effect of the solar modulation below few GeV. The detected positron fraction has been found to be in accordance with predictions from theoretical models that describe the transport of particles in the heliosphere taking drift effects into account.

I.1   Outline of the thesis

To put the subject of the thesis into context, an overview of the main topics concerning the study of cosmic ray is given in Chapter 1. Aspects related to the detection of cosmic rays particles and antiparticles and their role in the understanding of our Universe are considered. Particular emphasis is given to the effect of the heliospheric magnetic field on the propagation of charged particles below ~ 15 GV, and how it changes their energy spectra and intensities respect to the interstellar ones. A review of theoretical models describing the transport of particles in the heliosphere is also given and some of their predictions concerning the expected spectra detectable at Earth and charge sign dependent modulation are presented.
Chapter 2 gives a description of the PAMELA instrument. Each subdetector is presented in detail. The remaining chapters describe the physics analysis and the results. Chapter 3 deals with the electron and positron identification. The use of each PAMELA detector and

the selections developed to distinguish positrons among the vast quantity of cosmic rays detected by the instrument are described. The calorimeter provides most of the rejection power against the hadron background. Some effort has been put in developing selections that could exploit the different behavior of leptons and hadrons in the detector, even at this low energies where the particle showers are not well developed. Simulations have been used to define the calorimeter selection cuts. The main contamination sources for the selected positron sample are also presented here: an estimate of the residual contamining protons and pions in the final sample is given and taken into account. The possibility of a contamination of reentrant albedo particles in the positron sample has been also considered and excluded.

The efficiency of the selection procedure has to be taken into account when reconstructing the number of particles traversing the instrument. Simulation and flight data have been used to estimate the overall instrument efficiency and the entity of possibly introduced biases ; this is described in Chapter 4.

All parts of the analysis are put together in Chapter 5 where the number of detected electrons and positrons is corrected for the detection efficiencies and instrumental effects deriving the electron spectrum and the positron fraction. The results are then discussed in comparison with previous measurements and theoretical models.

Contents

Chapter 1

Cosmic ray physics

A brief overview of the main topics concerning the study of cosmic rays, subject of investigation of the PAMELA experiment, is given in this chapter. Some emphasis is put on the antiparticle component of cosmic rays and their detection in space.

Antiparticles are generally believed to have secondary origin, being produced by spallation of primary cosmic rays nuclei (mainly protons) on the interstellar gas. After the production, before reaching the Earth, these antiparticles will travel through the interplanetary space suffering interaction with the turbulent magnetic fields of the Galaxy, inside the heliosphere and with the Earth magnetic field; this will change their energy distribution depending on time, position and particle charge, species and initial energy distribution.

Any signature, possibly pointing out non-standard antiparticle production mechanisms, would appear as a distortion of the expected secondary flux. It is therefore of paramount importance to calculate the expected secondary antiparticle flux and to give a robust estimation of the associated theoretical uncertainties in order to interpret the experimental data in the correct way.

At low energies ($\leq$ tens of GeV) the heliospheric magnetic field affects the propagation of charged particle, changing their spectra in shape and intensity respect to the interstellar one. The study of this effect is essential for a better understanding of the solar environment, that is involved in modeling the background of possible primary signals, and interesting on its own right. Several aspects related to solar modulation are described in the second half of this chapter.

1.1   Cosmic ray history

Cosmic rays (CRs) consist of energetic charged particles incident on Earth from outer space. They were discovered by Hess in 1912 after measurements carried out on board of balloons by means of a leaf elettroscope detecting the electric charge rate. He observed a ionization effect that, after a little decrease with the altitude, increased again, and he concluded that there was a very penetrating radiation coming through the atmosphere from above. Millikan confirmed his results and called this radiation *cosmic rays*, name that has been preserved even when Compton showed that they were made by charged particles. The CR study has a special place in physics, not only on its own right but because of the pioenering role that cosmic ray research has played in the study of elementary particles and their interactions: about one century ago they offered a means to study physical processes at energies exceeding by more than three orders of magnitude those available from natural radioactivity and it took four decades of technological efforts to reproduce CR energies in accelerators. Nowadays, after almost 100 years since their discovery, the study of the cosmic radiation is still considered a tool that cannot be renounced for particle physics and astrophysical investigations.

1.2   Composition and energy spectrum

Three aspects of the primary radiation have been investigated, that have provided information about their origin, acceleration and propagation, and about the interplanetary space that surrounds us:

- its detailed composition

- the energy distribution of the particles

- any deviation from isotropy.

The charged primary particles of the cosmic rays consist principally of protons (86%), α-particles (11%), electrons (2%) and heavier elements up to uranium (1%). As will be discussed later on, antiprotons and positrons, generally believed to be of secondary origin, have also been measured in the cosmic radiation.
The study of CR elemental composition allows to obtain information about the propagation and life history of the charged particles in our galaxy. As shown in Fig. 1.1, the chemical composition of the CR nuclei exhibits remarkable similarities to the Solar System abundances[1]. A big difference is clearly visible for Li, Be and B (and similarly for Sc,

---

[1]The odd-even effect is associated with the fact that nuclei with Z and A even are more strongly bound than those with odd A and/or odd Z because of the *pairing energy $\delta(A)$* term, present in the nuclear binding energy formula (Sitenko A. G., 1972).
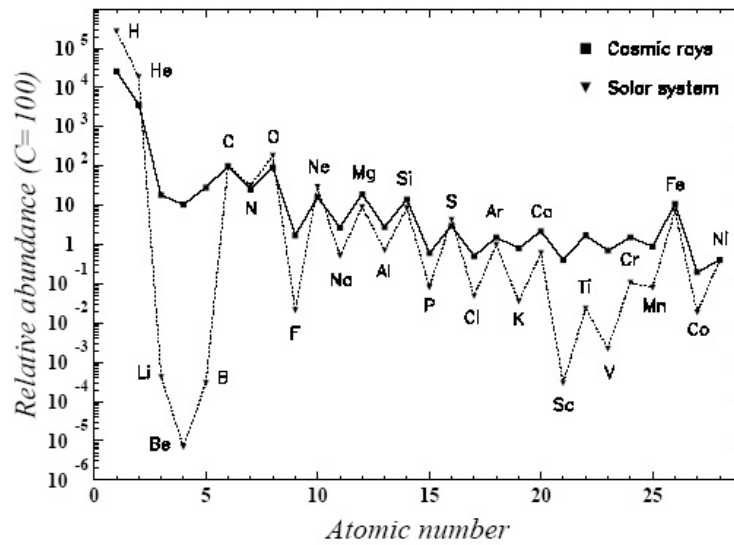
Figure (1.1) *Cosmic ray nuclear abundances for elements with $Z = 1 - 28$ as measured at Earth, compared with the Solar System ones. The abundance normalization value is relative to Carbon and equal to 100.*

Ti, V and Mn); the majority of this elements in the cosmic radiation is produced by spallation of primary nuclei (e.g. C) on interstellar H. If the spallation cross sections are known, a measure of secondary/primary abundances can give an indication about the quantity of matter traversed from the production to the measure time. Secondary radioactive isotopes measurements provide information about the time spent in our Galaxy. Thus, cosmic ray secondary to primary ratios are sensitive to the propagation in the Galaxy and their measure is widely used in models in order to constrain as much as possible the propagation parameters and reduce the theoretical uncertainties on the predictions.

The differential energy spectrum of cosmic rays is shown in Fig. 1.2. It spans more than ten orders of magnitude in energy and more than twenty in flux. Obviously this vastness requires a big diversification in the detection techniques used to measure it, on the other hand it offers the possibility to study several aspects of particle and astroparticle physics and, hopefully very soon, astronomy.

In the lowest energy range cosmic rays of solar origin can be detected at Earth and solar modulation effects on galactic CRs can be studied.

As the energy increases balloon- and satellite-borne experiments like BESS, PAMELA, AMS and others, are able to measure the antimatter component of cosmic rays. The typical instrument set-up consists of a magnetic spectrometer associated to detectors for hadronic and electromagnetic separation.

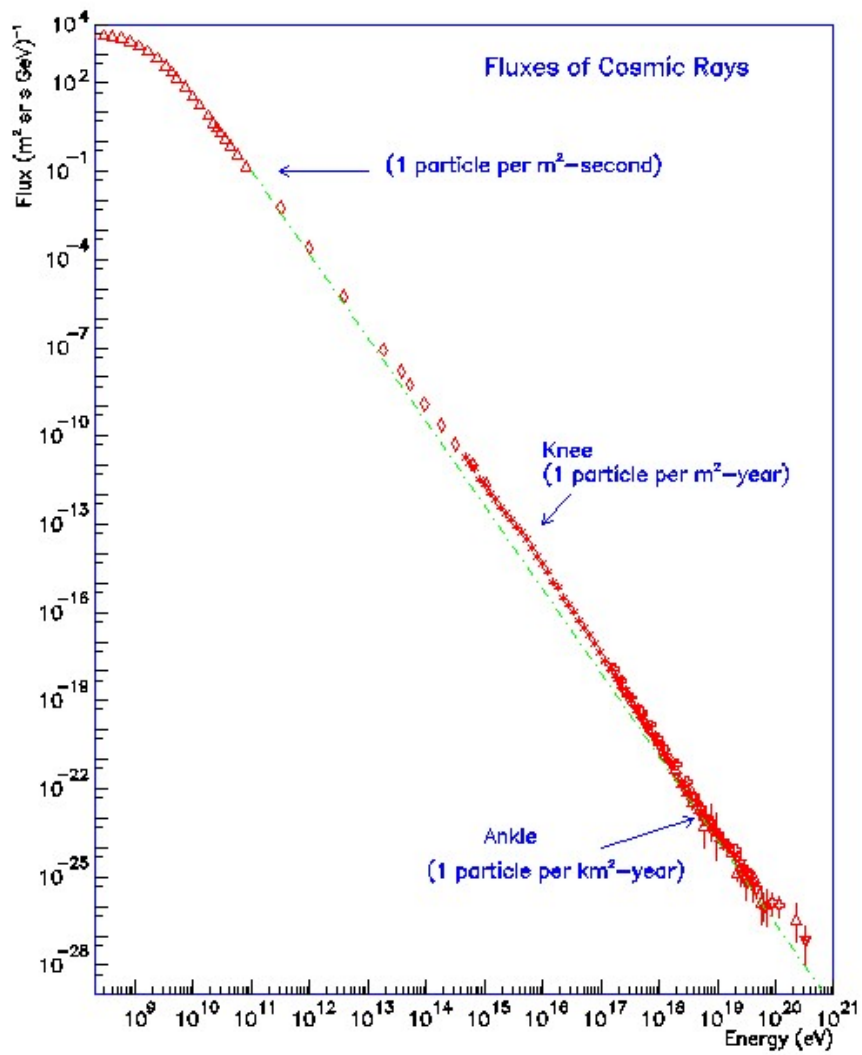Above few GeV the spectrum can be described by a power law in energy with spectral

Figure (**1.2**)   *All particle differential energy spectrum.*

index ~ -2.7 up to the so-called 'knee' (energy $\sim 10^{14}\ eV$), then it becomes steeper with an index of about -3.0 before apparently flattening off again above 10^{18} eV. The origin of this feature is still under investigation but it may suggest that more than one astrophysical process is responsible for cosmic ray acceleration.

Below the knee the statistics is still enough abundant to allow balloon experiments like CREAM, ATIC, TRACER and others to investigate the elemental composition of cosmic rays.

At energies $> 10^{18}$ eV the incoming flux is reduced to ~ 1 particle per km^2 per year, thus the investigation of ultra high energy cosmic rays (UHECRs) requires huge ground-based detectors able to gather enough statistics despite of the extremely low particle rate. The AUGER experiment is exploring the UHECR spectral region trying to give an answer to the debated issues related to the GZK[2] cutoff feature and possible spatial anisotropies.

The spatial distribution of the bulk of cosmic rays appears to be isotropic due to the effect of the 3 μG galactic magnetic field on charged particles propagation: their trajectory, while travelling through the Galaxy, is not a straight line but they are bent with a gyroradius that depends on their energy. Energetic particles with energy lower than 10^{18} eV have less than 1 kpc gyroradius, approximately comparable with the dimensions of the disk and the galactic halo, so that the bulk of the primary radiation is considered to be of galactic origin. However, the fact that the spectrum extends to very high energies ($> 10^{20}$ eV) indicates that some at least of the radiation must be of extra-galactic origin, since the interstellar magnetic field could not contain such particles inside our local Galaxy. It is only at this very high energies that we can hope to trace back to the CR sources just looking at their incoming direction, similarly to what we are used to do with photons, eventually beginning a CR astronomy.

1.3 Antimatter in space

As previously anticipated, antiprotons and positrons can be detected in cosmic rays and produced in accelerators, yet, less than 100 years ago antimatter was just a speculation.

In 1928, Paul Dirac wrote an equation, which combined quantum theory and special relativity, to describe the behaviour of the electron. He formulated his 'hole theory' in order to interpret the negative energy solutions of this equation asserting that for every particle that exists there is a corresponding antiparticle, exactly matching the particle but with opposite charge. For the electron, for instance, there should be an "antielectron" identical in every way but with a positive electric charge.

In 1932 Carl Anderson was studying showers of cosmic particles in a cloud chamber and saw a track left by "something positively charged, and with the same mass as an elec-

---

[2]Greisen, Zatsepin and Kuzmin

tron". After nearly one year of effort and observation, he decided the tracks were actually antielectrons, each produced alongside an electron from the impact of cosmic rays in the cloud chamber. He called the antielectron a "positron", for its positive charge. Confirmed soon after by Occhialini and Blackett, the discovery gave Anderson the Nobel Prize in 1936 and proved the existence of antiparticles as predicted by Dirac.

It was necessary to wait 22 years before the antiproton discovery, by Segre' and co-workers in accelerator experiment, and one year more for the antineutron, while first observation of antiprotons in cosmic rays dates back to 1979 in balloone-borne experiments by Golden *et al.* (1979) and Bogomolov and et al. (1979) that started a wide program of direct antimatter research, as will be discussed in section1.3.2.

1.3.1   A matter-antimatter asymmetric Universe?

The discovery of the cosmic background radiation by Penzias and Wilson in 1965 provided the evidence that the early Universe was a hot expanding plasma of matter, antimatter and photons. In the simple Big Bang model, the plasma in the very early Universe contains approximately the same number of baryons, anti-baryons and photons. As the Universe expands, the density of particles and antiparticles falls, annihilation process ceases, effectively freezing the ratio baryon/photon at 10^{-18}. Actually, in the present Universe the observed baryon/photon ratio is about 3×10^{-9} as from microwave background. This model is not able to account for the observed baryon/photon ratio when no mechanism for separating matter and antimatter exists, nor to give any condition for such separation. Such a mechanism has been suggested by Sakharov in 1967 in a famous JEPT letters (Sakharov, 1967): he pointed out the conditions necessary to achieve a baryon-antibaryon asymmetry assuming a symmetrical initial condition for the Universe (B[3]=0):

- B violating interactions

- Deviation from thermal equilibrium

- CP and C violation

At present, proton decay is predicted by Grand Unified Theories (GUTs) but it has never been discovered, CP violation occurs in nature but at a level too low for the baryogenesis, thermal non-equilibrium arises in standard models of the Big Bang. Then, the baryonic symmetry or asymmetry of the Universe remains a question open to experimental observations. This topic can be investigated either 'indirectly', by measuring the spectrum of

---

[3]Baryonic number.

the cosmic diffuse gamma, or 'directly', by searching for anti-nuclei and by measuring antiprotons and positrons energy spectra.

Following the Dirac speculation about a completely new Universe made out of antimatter[4], it is possible to imagine a Universe containing regions of antimatter and matter. In this scenario hadronic matter and antimatter annihilate at the domain boundaries, including in the products neutral pions that subsequently decay in two gamma-rays that should make a contribution to the extragalactic diffuse background gamma radiation. An accurate study of the experimental Cosmic Diffuse Gamma spectrum indicates that the antimatter/matter fraction is less than 10^{-15} in the Galactic molecular clouds, than 10^{-10} in the galactic halo, and than 10^{-5} at the level of a cluster; so, if antimatter exists, it is separated at least at the level of 50-100 Megaparsec (Cohen *et al.*, 1998; Adams *et al.*, 1997).

In 1979 the teams of Golden *et al.* (1979) in USA and Bogomolov and et al. (1979) in Russia identificated the first antiprotons in cosmic rays, leading to fervent activity and theoretical speculations: they found that the measured antiproton spectrum largely exceeded the expected antiproton flux produced in the interactions of CR's with the interstellar matter (Fig. 1.4). Various theoretical interpretations were developed, as primordial antimatter coming from antimatter domains in a baryonic symmetric Universe, evaporation for Hawking effect of primordial mini black holes, exotic particles annihilation. In the light of these results, despite the non incouraging constraints from gamma-ray sky surveys, the idea that the Universe is globally symmetric became actractive again. There are indeed natural theoretical frameworks for such cosmology; as an example, several authors recently suggested that very small bubbles with very high baryon asymmetry could exist, possibly produced by the presence of a stochastic or dynamical violation of CP (Dolgov, 2008).

1.3.2   The search for antimatter in the cosmic radiation

As anticipated in the previous section, the observation of the cosmic radiation holds out the possibility of directly detecting a particle of antimatter which has escaped as a cosmic ray from a distant antigalaxy, traversed intergalactic space filled by turbulent magnetic field, entered the Milky Way against the galactic wind and found its way to the Earth.In particular, the apparent baryon-asymmetrical Universe scenario could be probed by searching for antihelium in the cosmic radiation, since this is not thought to be produced in secondary processes, while the detection of antinuclei with $Z > 2$ in CRs would

---

[4]The famous Dirac sentence, part of his Nobel Lecture speech, is:" We must regard it rather as an accident that the Earth (and presumably the whole Solar System), contains a preponderance of negative electrons and positive protons. It is quite possible that for some of the stars it is the other way about, these stars being built up mainly of positrons and negative protons ".
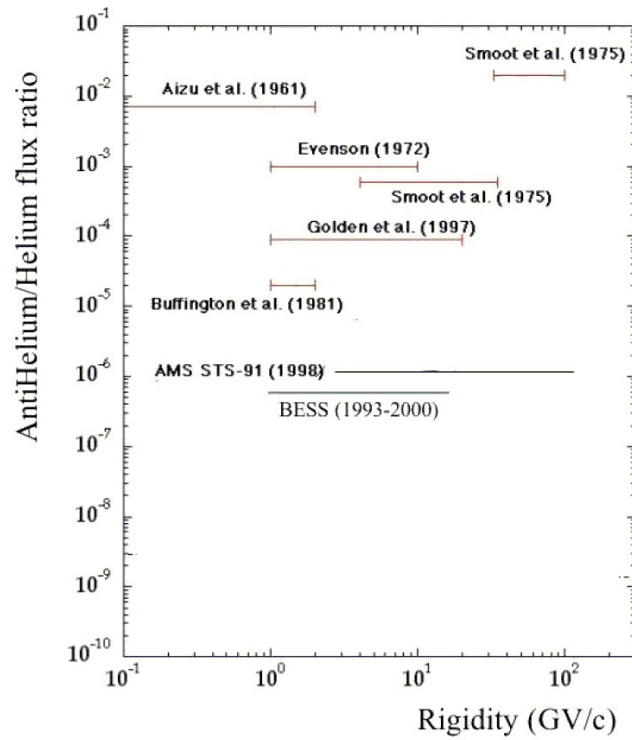
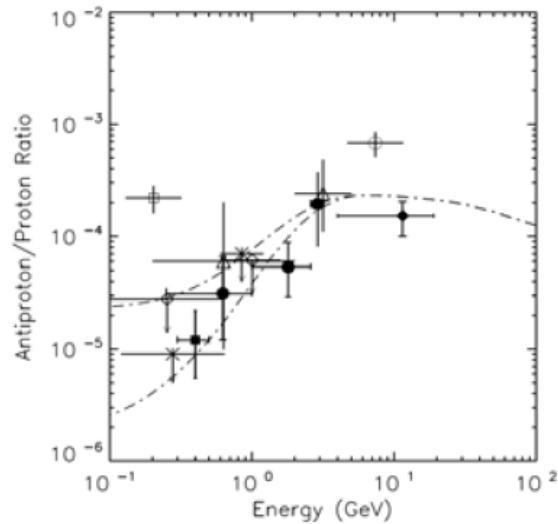**Figure (1.3)**   *Experimental limits for the $\bar{H}e/He$ ratio.*

Figure (1.4)   *First measurements of the $\bar{p}/p$ ratio.   Data points refer to balloon experiments by the teams of Golden et al. (1979) (open circles) and Bogomolov and et al. (1979); Bogomolov et al. (1990) (open triangles).*

provide direct evidence of the existence of antistellar nucleosynthesis in antimatter domains or lumps.The experimental limits obtained up to now for the $\bar{He}/He$ are presented in Fig. 1.3.

The first results obtained on balloons were received by the scientific community with excitation and triggered the subsequent missions: in 1970s the technology at the base of the space transportation system was enough advanced for transporting large detectors to space and NASA promoted a CR program in space in which the search for antinuclei and the observation of the energy spectra of CR antiparticles were considered of primary importance. Thus the long history of space exploration searching for antimatter began, leading to perform several balloon-borne experiments focused on CR antiparticles detection, like those of the WiZard, BESS and HEAT collaborations, and the AMS-01 flight on board of the Space Shuttle.

The first historical results concerning an antiproton excess were not confirmed by the following experiments. The BESS collaboration performed several balloon flights, providing antiprotons measurements over an extended period of time. Their data show clearly the effect of the changing solar activity on p and $\bar{p}$ fluxes and an evident charge-sign-dependent solar modulation effect in the $\bar{p}/p$ ratio measured before and after the most recent (2000) reversal of the solar magnetic field (Asaoka *et al.*, 2002). More details about solar modulation will be given in Sec. 1.4 as essential part in the frame of the investigation that aims at a better understanding of the background posed by the production of secondary antiparticles in the interstellar space, in order to investigate possible primary sources.

The mentioned possibilities for the scientific investigation definitely add interest to the investigation and detection of antimatter in space, and push the experimentalist to build instruments capable to extend the explored energy range and increase the collected statistics.

The PAMELA experiment is optimized to measure the antimatter component of cosmic rays with an unprecedented precision and in a wide energy range, partially still unexplored.

1.3.3 Dark Matter

During the years the research of antimatter (antiprotons, positrons, antideuterium) has acquired significance as possibly providing an answer to another question: *what is the Universe made of?* A number of observational probes point to the existence of a nonbaryonic, non visible, matter, the Dark Matter.

Evidence for the existence of Dark Matter comes from a number of astrophysical and cosmological probes. The first one dates back to 1933 when Zwicky observed a large velocity dispersion of the members of the Coma galaxy cluster.At a different scale, the galactic one, the most convincing and direct evidence for dark matter existence comes

from the observations of the rotation curves of the galaxies, indicating that stars rotate 'too fast' to be bound by Newtonian gravity if all matter is visible. The Big Bang Theory, the measurements of light nuclei produced in primordial nucleosyntesis and the the study of the cosmic microwave background (CMB) radiation indicate that baryonic matter density cannot be more than 4% in a flat Universe.

Neutrinos are not a valuable candidate being relativistic at the time of decoupling: cold[5] dark matter (CDM) is required by the standard model of cosmology, where structure formed through gravitational amplification of small density perturbations, that is strongly supported by studies of the CMB radiation.

The CMB is known to be isotropic at the 10^{-5} level and to follow with extraordinary precision the spectrum of a black body corresponding to a temperature T = 2.726 K. The analysis of the small CMB anisotropies enables accurate testing of cosmological models and allows to put constraints on cosmological parameters. The density of CDM can be derived from the 5-year WMAP (Wilkinson Microwave Anisotropy Probe) data (Komatsu and et al., 2009):

$$\Omega_{CDM}h^2 = 0.1131 \pm 0.0034 \tag{1.1}$$

where h is the Hubble constant today in units of $100 \ km \ s^{-1} \ Mpc^{-1}$, with the estimate $h = 0.705 \pm 0.0134$.

The existence of dark matter does not find an explanation in the framework of the Standard Model (SM) of particle physics; this is only one among several reasons that indicate the SM as a low-energy limit of a more fundamental theory. A wide variety of SM extensions have been hypothesized, leading to a proliferation of dark matter candidates. Most of the proposed models contains WIMPs (Weakly Interacting Massive Particles) as DM particles. Various extensive reviews of particle dark matter exists (Bertone *et al.*, 2005) and (Bergström, 2009) and references therein, as well as a recent book (Bertone, 2009).

The most popular dark matter candidate is the lightest stable particle in R-parity conserving supersymmetric[6] models, the neutralino χ. Neutralinos should pervade the Milky Way halo and be concentrated at the galactic centre. As they mutually annihilate as Majorana particles ($\bar{\chi} = \chi$), they should produce high energy photons and antimatter cosmic rays. The search for the annihilation products represents a tool for dark matter indirect measurement[7]. Using simple models of thermally produced dark matter, equation 1.1 corresponds

---

[5]In this context, cold means matter moving with non relativistic velocities when structure formed in the Universe.

[6]Supersymmetry is an extension of the Standard Model describing a complete, spontaneously broken, symmetry between fermions and bosons.

[7]Other indirect measurements involve neutrinos and gammas. On the other hand, direct dark matter

to an average of the annihilation rate at the chemical decoupling of (Jungman *et al.*, 1996):

$$\langle \sigma_A \, v \rangle = 2.8 \times 10^{-26} \; cm^3 s^{-1} \tag{1.2}$$

Neutralinos can annihilate into gauge boson pairs via several processes (Jungman *et al.*, 1996), as well as in fermions. Figure 1.5 shows the tree level diagrams for neutralino annihilation into fermion pairs describing the exchange of Higgs and Z^0 bosons and sfermions. The amplitudes of all tree level diagrams to fermion pairs are proportional to the final state fermion mass, but the annihilation rate into light fermions is not high due to helicity suppression. Fig. 1.6 illustrates the consequent production of antiparticles, gammas and neutrinos.

An other example of extension of the Standard Model is provided by extra dimensions
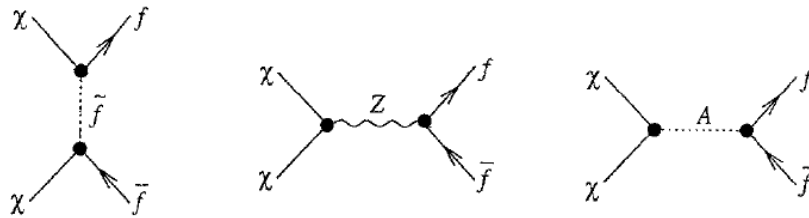
Figure (1.5) *Tree level diagrams for neutralino annihilation into fermion pairs. From (Jungman et al., 1996)*
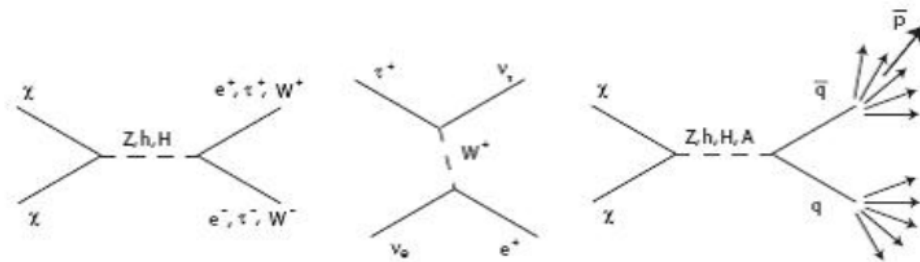
Figure (1.6) *Antiparticle production from neutralino annihilation.*

theories: following an early idea of Kaluza, searching for a fundamental theory with a unified description of all interactions, theories with unified extradimensions describe a

---

detection is usually performed in underground facilities looking for the interaction of WIMPs with matter, e.g. by recording the recoil energy of nuclei, as the particles scatter off them. A significant contribution to the dark matter study is also expected from new generation high energy experiments at accelerators, that aim to produce new physic particles.

scenario in which all particles and fields can propagate to extradimensions. The lightest of all the states corresponding to the first excitations of the particles of the SM, the lightest Kaluza-Klein particle, is a stable boson that can annihilate in SM particles (Cheng *et al.*, 2002).

As previously mentioned, among the SM particles possibly produced as final state of DM candidates interactions, a special place is reserved to antiparticles. Figures 1.7 and 1.8 show the state of the experimental measurements of antiparticle to particle ratios before the PAMELA experiment. In order to have a more organic picture of the antiparticle component of cosmic rays it is desirable that a single experiment could provide measurements in a wide energy range, possibly extending the explored one at higher energies with a better resolution and improved statistics.

Large fluctuations in the low energy measurements are present in both plots; this depends on the interaction of charged particles with the solar environment, that modulates CR spectra and intensities. Experimental data from direct and indirect measurements induced several authors to consider a light ($m_\chi \leq 50 \; GeV$) DM candidate scenario as reasonable (e.g. Goodenough and Hooper (2009); Bottino *et al.* (2008)). In this case the knowledge of the expected secondary antiparticle flux at low energy would be important in order to distinguish between light DM signal and background. The extent of the solar modulation effect on particles detected at Earth depends on the heliospheric conditions and on the charged particles characteristics. Several detailed theoretical models exist, that try to describe it (see section 1.4.4).

Accurate CR measurements are crucial to constrain the model parameters and reduce the related uncertainties, allowing for a better prediction. This work of thesis intends to study the low energy positron and electron signals with the PAMELA experiment, from 200 MeV to 2.6 GeV, that could be used for the fine-tuning of the current models.

1.3.4   Antiparticle secondary production and propagation

As pointed out in the previous section, models predict the production of antiparticles from dark matter annihilation; they could also come directly from astrophysical sources. Moreover, besides these primary mechanisms, secondary antiparticles are produced by spallation of cosmic rays within the interstellar gas. The latter production process yields a nearly equal amount of particles and antiparticles, hence, particles have to be mainly of primary origin, if considered that CR e^+ and $\bar{p}$ abundances are orders of magnitude less than the respective particles .

Any observed distortion respect to the expected purely secondary flux at Earth could indicate a non-standard production mechanism and the presence of a primary source of antiparticles. For this reason, many efforts have been done in order to theoretically constrain the expected secondary antiparticle flux at Earth, taking into account all the uncertainties
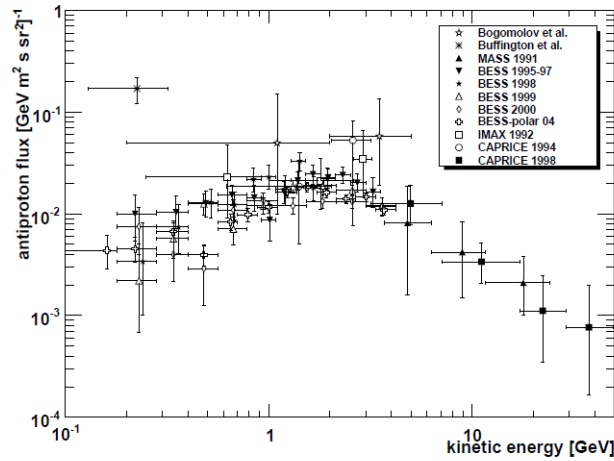
Figure (1.7)   *Antiproton to proton flux ratio experimental data before PAMELA*
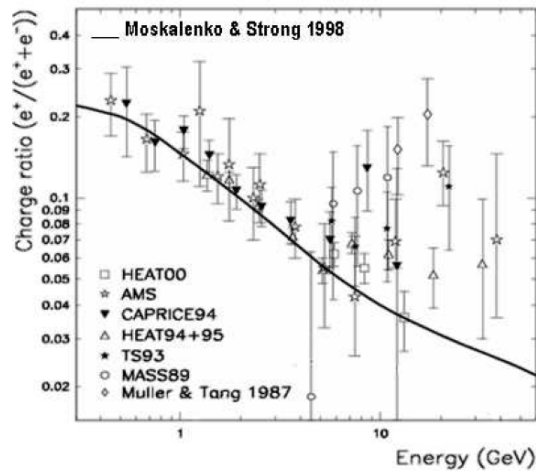

Figure (1.8)   *The positron fraction $e^+/(e^+ + e^-)$ experimental data available before*
                    PAMELA. The black curve represents the expectation from the secondary
                    production model by Moskalenko and Strong (1998).

connected to the calculation and carefully evaluating their impact on the final predicted flux. The expected fluxes can be calculated from the observed cosmic ray nuclei fluxes, using the relevant physics and solving the diffusion equation.

Antiprotons and positrons production occurs by means of nuclear reactions between two colliding nuclei (cosmic rays protons on interstellar (IS) hydrogen or helium and cosmic rays alpha on IS proton or helium), yielding many hadrons, mostly pions whose radiative decays are the principal source of the galactic diffuse γ-ray emission.

Secondary antiprotons can be produced according to the reaction:

$$p + A \longrightarrow \bar{p} + X \tag{1.3}$$

where A is the interstellar matter nucleus and X is anything consistent with charge and baryon number conservation. The fragmentation products then decay and produce $\bar{p}$; spallation reactions also produce antineutrons which in turn decay and contribute to the $\bar{p}$ signal. The fundamental process is obviously $pp \to pp\bar{p}p$, a threshold reaction that can produce $\bar{p}p$ pair at rest in the center of mass system if a kinetic energy $E = 6\ m_p$ is available.

Analogous reactions rule the secondary positron production, yielding many charged pions and other mesons, for which e^+ are the final products of the decay chain. In the case of proton-proton collisions at energies well below about 3 GeV the main channel for e^+ production involves the excitation of a Delta resonance, which then decays into pions:

$$p + H \longrightarrow p + \Delta^+ \longrightarrow \begin{cases} p + \pi^0 \\ n + \pi^+ \end{cases} \tag{1.4}$$
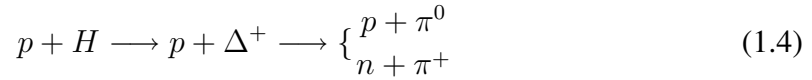
The charged pions decay into muons which subsequently decay into positrons. At higher energies direct production of charged pions proceeds with the process:

$$p + H \longrightarrow p + n + \pi^+ \tag{1.5}$$

Kaons may also be produced:

$$p + H \longrightarrow X + K^\pm \tag{1.6}$$

their decay produces muons (63.44%) and pions (20.92%) (PDG).

Before reaching the solar neighborhood a charged particle, travelling in the Galaxy from its source, is affected by several processes. Scattering by magnetic fields leads to a random walk in both real space (diffusion) and momentum space (diffusive reacceleration). Particles may also be spatially convected away by the galactic wind (which induces adiabatic losses), and lose energy as they interact with either interstellar matter or the electromagnetic field and radiation of the Galaxy. Moreover, before reaching the Earth charged particles travel through the heliosphere and, if the energy is low enough, undergo solar

modulation and are finally affected by the Earth magnetic field. All this processes are strongly dependent on particle energy, species, charge and on position in space and time. Moskalenko *et al.* (2002) shows how data with improved statistics allow to test models of CR propagation and heliospheric modulation[8]. The following general transport equation describes these dependences:

$$\frac{\partial N_i}{\partial t} = \nabla \cdot (D\nabla N_i) - \frac{\partial}{\partial E}[b_i N_i] - \nabla \cdot u N_i + Q_i - p_i N_i + \sum_{k \geq 1} N_k p_{k \rightarrow i} \qquad (1.7)$$

where $\frac{\partial N_i}{\partial t}$ denotes the density of particles of type i per unit energy and Q_i is the source term. The terms on the right side represent, respectively, diffusion, energy changing processes (ionisation, reacceleration), convection with velocity u, the source term, losses due to collisions or decay, and secondary production. The transport through the magnetic turbulences is described by the diffusion coefficent D, while the last term describes energy losses. By numerically solving the transport equation, calculated antiparticles fluxes can be evaluated together with the associated theoretical uncertainties that refer to several origins: first, the CR nuclei measurements have their experimental uncertainties which then affect the predictions of induced secondary fluxes; second, various models of the nuclear cross-sections are available, implying a range of theoretical variations; third, uncertainties in the propagation parameters involved in the diffusion equation (they are not directly measured, but their values can be constrained by comparing the calculation results with the observation of primary-to-secondary nuclei ratios that are very sensitive to their variation (Maurin *et al.*, 2002).

Above few GeV the propagation of positrons (and electrons) in the Milky Way is dominated by space diffusion and energy losses and it differs from that of the nuclei in several respect, although the space diffusion is an essential ingredient common to all cosmic ray species: e^+ and e^- suffer mostly from inverse Compton and syncrotron energy losses (Moskalenko and Strong, 1998) whereas (anti-)protons are most sensitive to the galactic wind, nuclear interactions and energy losses by ionization as they cross the Milky Way disk. An important test for CR propagation models is their ability to reproduce both the antiproton-to-proton flux ratio and the secondary-to-primary nuclei ratio.

Though the secondary positron production can be considered homogeneous throughout the disk[9], positrons reaching the Earth are mostly created locally, especially at high energy (Delahaye *et al.*, 2009): as it is shown in Fig. 1.9, more than a half of the 100 MeV positrons come from less than 2 kpc because of very efficient energy losses that reduce

---

[8]Widely used models are based on the simple force-field approximation. More complex and realistic modeling takes into account drift effects. Details about solar modulation will be given in Sec. 1.4.

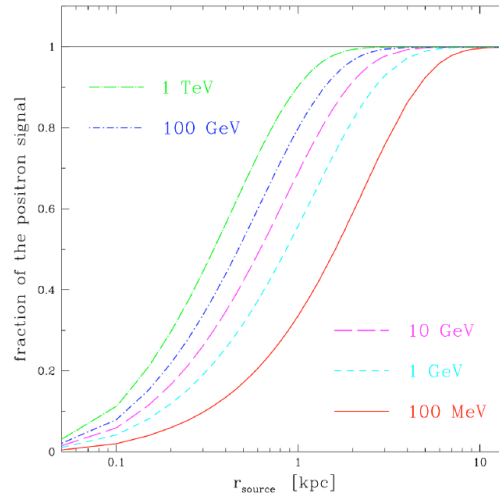[9]The interstellar gas is located mainly in the galactic disk.

Figure (1.9)   *Fraction of the positrons detected at the Earth which are produced whithin a disk of radius r_{source}.   The larger the energy, the closer the source (Delahaye et al., 2009).*

the e^+ horizon strongly as the energy increases. Antiprotons are not so affected by energy losses and their mean free path in interstellar space is much larger than what traversed by cosmic rays in the Galaxy.

1.4   The solar environment

The Sun is the central body and energetic engine of our Solar System. Its magnetic field, embedded in the solar wind (SW), is also the source of the biggest of the solar system magnetospheres, the heliosphere, and of the related modulation of the galactic cosmic rays.

The Sun represents a fairly typical star in our Galaxy, classified as G2-V spectral type, mainly composed by hydrogen ($\sim$ 90%), helium ($\sim$ 10%) and traces of heavier elements, with a radius of $r_0 \approx 700000 \ km$, a mass of $m_0 \approx 2 \times 10^{33} \ g$, a luminosity of $L_0 \approx 3.8 \times 10^{26} \ W$ and an age of $t_0 \approx 4.6 \times 10^9 yrs$. The Sun lies in a spiral arm of our Galaxy at a distance of $8.5 \ Kpc$ from the galactic center and at 1 Astronomical Unit (AU)[10] from the Earth.

Because the Sun is a gaseous body there is no physical surface. The visible solar surface over the convective zone is called photosphere, a thin layer (about $500 \ km$ thick) observable in white light. Above the photosphere are two transparent layers: the chromosphere,

---

[10]1 AU corresponds approximately to 149.6×10^6 km.

visible during the eclipses, which extends some $10000\,km$ above the photosphere and the corona which is observable beyond chromosphere for more than $10^6\,km$.

The Sun is governed by a very strong magnetic field which is generated with a strength of $B \approx 10^5\,G$ in the thin layer between the radiative and convective zone inside the star, and emerge at the solar surface in active regions. The differential rotation of the solar surface, due to its gaseous consistence, is thought to give rise to the so-called solar dynamo, which flips the magnetic polarity of the Sun every ~ 11 years or returns to the same magnetic configuration every ~ 22 years. The 11-years periodicity is refeared to as *solar activity cycle*. The periodicity is also visible in the records of the sunspot[11] numbers that are widely used to monitor the solar activity. Fig. 1.10 shows the periodic variation of the solar activity in terms of sunspot numbers.

Experimental observations indicate that during solar activity minimum conditions the solar magnetic field is approximately dipole-like with a magnetic dipole axis almost aligned to the solar rotation axis, while during the declining phase of the solar cycle the dipole is more tilted. The angle between the Sun's rotation axis and the magnetic axis is known as the *tilt angle* α. Even thought the Sun has a complex magnetic field, the dipole term nearly always dominates the magnetic field. As the solar activity approaches its maximum, when the polarity reversing happens, the dipolar shape seems to be not representative any more of the Sun's magnetic field that seems rather to be destroyed and produced again in the opposite polarity.
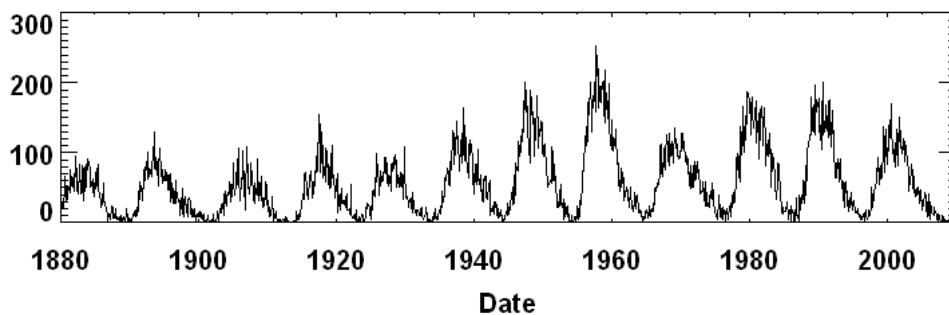
Figure (1.10)   *Number of sunspots (http://www.spaceweather.com).*

The temperature of the highly ionized gas of the corona is very high so that it is not gravitationally bound to the star and constantly blows away from the Sun surface to maintain the hydrostatic equilibrium. The supersonic solar plasma expanding into space is

---

[11]Sunspots are regions of the solar surface cooler than the others, associated to strong magnetic fields and visible on the photosphere as dark areas of irregular shape.

called the *solar wind*.

The solar wind is an excellent thermal and electrical conductor. The electrical conductivity of the plasma is so high that the solar magnetic field is frozen into the solar wind flow as it expands away from the Sun (Parker, 1964, 1965). According to the Parker's solar wind model, due to the Sun rotation, magnetic field lines are bent in the form of an Archimedean spiral in the Sun's equatorial plane, and in helices wrapped about the rotation axis of the Sun out of the equator (see Fig. 1.11). Their inclination relative to the radial direction is $\sim 45°$ in the equatorial plane at Earth.
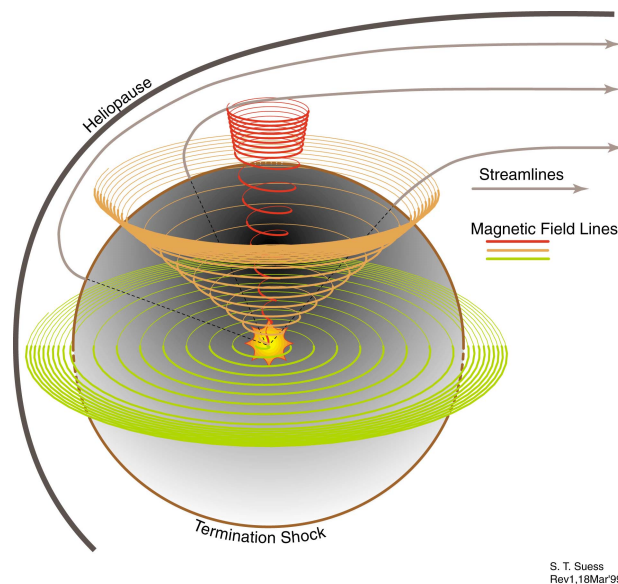

Figure (1.11)   *Parker field magnetic lines, bent into Archimedean spirals due to the Sun rotation. They are drawn here at solar latitudes of 6, 45 and 84 degree respectively (http://science.nasa.gov/ssl/pad/solar/suess).*

The solar magnetic field transported into the interplanetary space by the solar wind forms the heliospheric magnetic field (HMF) or interplanetary magnetic field (IMF), that has been observed beyond the most distant planets of the Solar System and is mostly responsible for the modulation of cosmic rays in the *heliosphere*, the region of space filled by the plasma originating from the Sun and transported outward.

The solar wind is prevented to expand indefinitely by the local interstellar medium that fills the interstellar space and confines the solar plasma in the heliospheric cavity. When the solar wind density is too low to compensate the pressure of the interstellar medium, the solar wind slows down abruptly and the supersonic plasma velocity decreases to subsonic speeds creating a shock, the so-called solar wind termination shock (TS). Voyager 1 encountered the TS on December 16, 2004 at a distance of 94 AU from the Sun and entered the heliosheet, the boundary layer between the termination shock and the heliopause, that

separates the solar wind from the interstellar plasma. Beyond the heliopause the interstellar flow is diverted around the heliosphere and a shock that slows it probably exists. The different plasma regimes are schematically illustrated in Fig. 1.12.
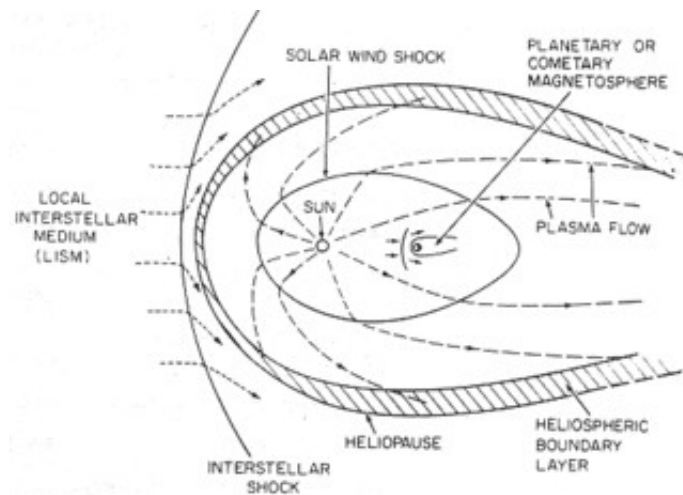 Since 1970s several missions have ventured torwards the outer space, like Pioneers, Voy-

Figure (1.12) *Schematic view of the heliosphere.*

agers and the Ulysses spacecraft that is, up to now, the only probe for the exploration the high latitude regions of the heliosphere.

In 1976 observations made by Pioneer 11 spacecraft up to about $16°$ above the solar equatorial plane have shown that the IMF has the sign of the solar magnetic field of the appropriate pole. The HMF field lines of the two heliospheric hemispheres are separated by a the *heliospheric current sheet* (HCS), which is effectively the extension of the solar magnetic equator into the solar wind. Because the magnetic and rotation axes of the Sun are not aligned the rotation of the Sun causes a warped or wavy current heliosheet three dimensional structure that is shown in Fig. 1.13, the so called 'balerina skirt'; a larger tilt angle corresponds to a larger latitudinal extend of the HCS.

The coronal magnetic field can be calculated from photosperic field observations with a potential field model, producing the source surface field maps that are shown in Figure 1.14 as determined by the Wilcox Solar Observatory (WSO website). The solar polar magnetic field strenght is shown as contours for the source surface at $2.5\ r_0$ for $360°$ for a solar minimum and maximum condition respectively in the upper and lower panel. The different shaded grey represent different polarities (blue, light shading shows the positive regions), while the neutral line is black.
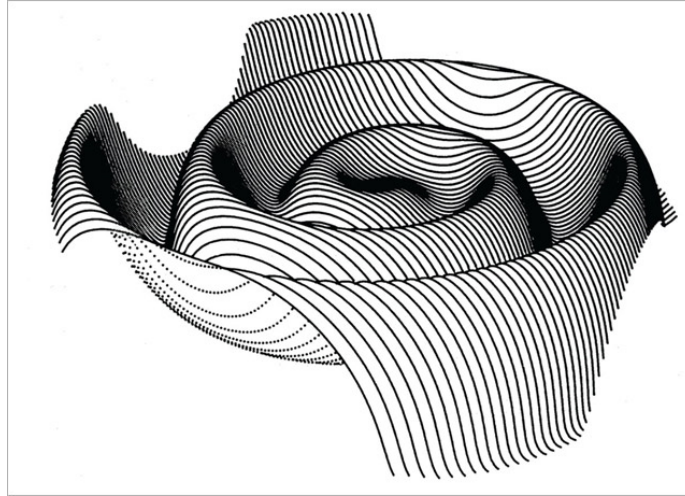
Figure (1.13)   *Drawing of the warped neutral current heliosheet.*

1.4.1   Charged particles in the heliosphere

Within the heliosphere, energetic charged particles of different origin can be identified. Some of them are produced inside the heliosphere, at the Sun site, while others come from the outer space. In the latter case, as already mentioned, the interplanetary magnetic field affects their passage modulating their intensities. Furthermore, some evidence has been found for particle acceleration processes, in many cases in association with shock waves, throughout the heliosphere.

Depending on their origin, CRs that reach the Earth are usually divided among: (1) galactic cosmic rays, (2) solar particles, (3) anomalous cosmic rays.

Galactic cosmic rays (GCRs) enter the heliosphere and travel through it towards the Earth. Their main characteristics have been recalled in Section 1.2. Their study is very interesting from a modulation point of view since they are the main subjects of solar modulation.

Solar Energetic Particles (SEPs) are produced and accelerated by solar events. Since their first observation, when Forbush studied the large solar events of February and March 1942, they have been observed with neutron monitors, riometers and with detectors on balloons and spacecraft. This allowed an extensive study of their time profiles, spectra and abundances. Today it is still an open question whether the particle acceleration is caused by a solar flare or due to shock waves driven by coronal mass ejections.

Moreover, an additional source of charged particles inside the heliosphere is represented by Jupiter: when Pioneer 10 came within 1 AU of the planet it became clear that the jovian magnetosphere is a continuous source of MeV electrons (Chenette *et al.*, 1974) and, later, more data became available with the Ulysses flyby. The fact that the source of jovian electrons is not central in the heliosphere and that it can be considered point-like from a
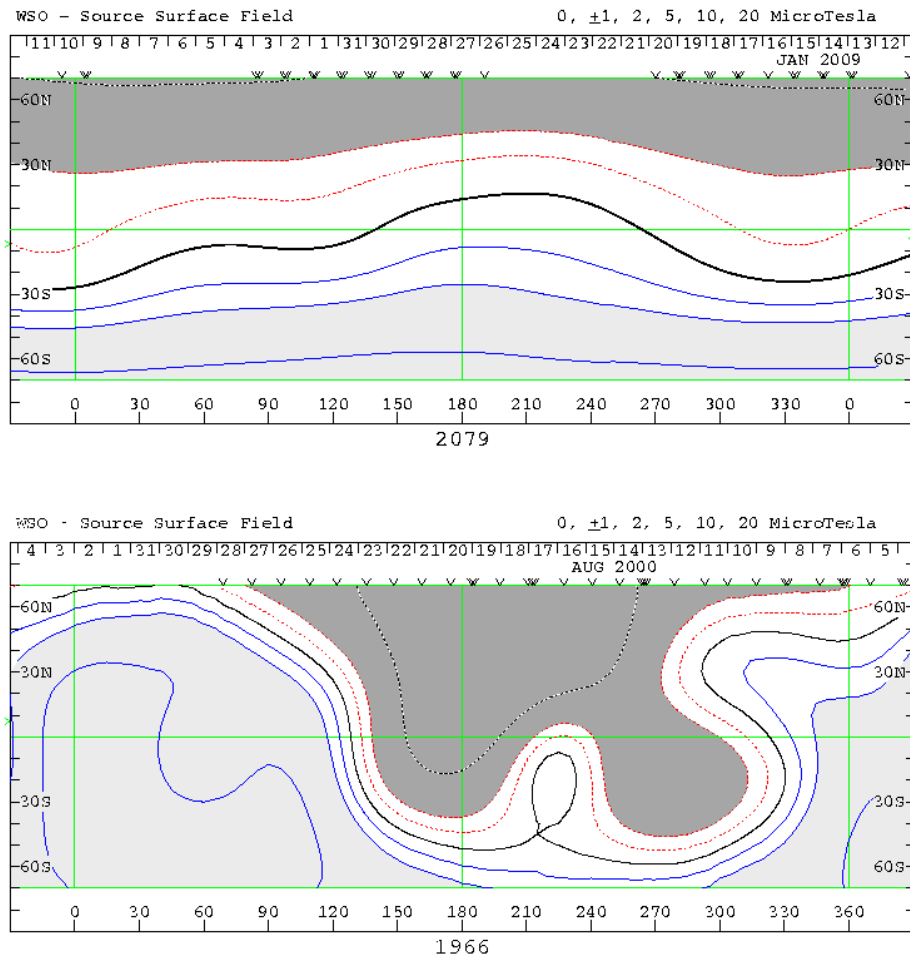
Figure (1.14) *Computed source surface field map for southern and northern hemisphere. The different shades of grey correspond to different polarities. The upper panel refers to solar minimum during January 2009 while the lower panel corresponds to increased solar activity conditions (August 2000).*

modeling point of view, makes jovian electrons a useful and effective tool for the study of the heliosphere.

Anomalous cosmic rays (ACRs) are believed to come from interstellar neutral particles, which have entered the heliosphere, subsequently ionized by the solar wind or the UV radiation and finally accelerated to energies larger than 10 MeV/nucleon, probably at the termination shock. They present characteristic energy spectra that show a different slope at energies of tens of MeV respect to the all particles spectrum.

Anomalous cosmic rays, like galactic cosmic rays, are modulated by the turbulent heliospheric magnetic field. The next section deepens the role of the heliosphere in the propagation of GCRs.

1.4.2   Galactic CRs and solar cycle

As mentioned, it became evident that the Sun has a quasi-periodic ~ 11 years cycle called solar activity cycle. Every 11 years the Sun moves through a period of fewer and smaller sunspots called 'solar minimum' and a period of increased sunspot numbers and dimensions called 'solar maximum'. The Sun's magnetic field follows as well this periodicity varying its intensity of a factor ~ 2. Moreover the tilt angle changes with time going from $\sim 10°$ during solar minimum periods, when the magnetic dipole axis is almost aligned to the rotational one, to a maximum level during the solar maximum activity, when the magnetic field inverts its polarity.

Neutron monitor (NM) data indicate that the solar activity has an influence on cosmic rays: NMs can measure at Earth neutrons generated by galactic cosmic rays impinging the atmosphere and producing showers. Figure 1.15 shows the clear anti-correlation among CR intensities and the solar cycle. Beyond the 11-year cycle in anti-phase with solar activity (e.g. sunspot numbers), a 22-year cycle is evident, which does not follow so directly from inspection of solar activity indices. It is related to the inversion of the solar magnetic field, that returns to the same polarity each 22 years: depending on whether the orientation of the projection of the magnetic dipole on the solar rotation axis (A) is positive or negative, we refer to as the A+ and A- state.

By comparing data at Earth to data taken in the outer heliosphere we obtain a further convincing evidence that the Sun is the source of the modulation. Like the 1 AU count rate the Voyager 2 count rates shown in Fig. 1.16 are modulated with the solar cycle, but with an amplitude that depends on the spacecraft distance from the Sun. This and the effect that the modulation is delayed in the outer heliosphere indicate the Sun as the modulation origin.

Solar modulation is effective on low energy particles (below about 10 GeV), and affects
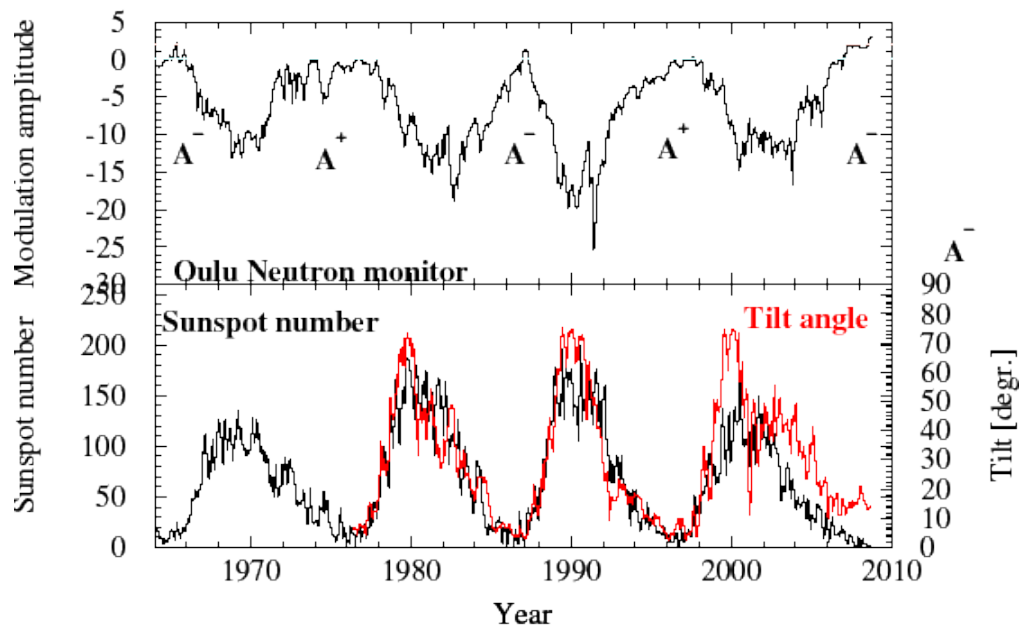
Figure (1.15) *CRs intensities as measured by Oulu NM in clear anticorrelation with the solar activity. The sunspot number as well as the tilt angle are used to monitor the solar cycle.*
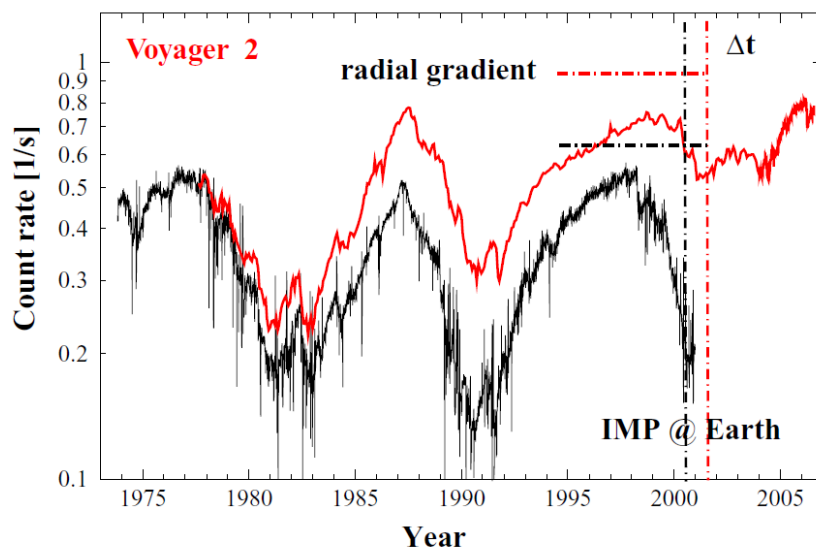
Figure (1.16) *Count rates of > 70 MeV protons as measured by detectors on board of Voyager 2 while traveling towards the outer heliosphere and by IMP at Earth. Data indicate that the intensity is higher in the outer heliosphere because of the reduced solar modulation (Heber and Potgieter, 2006).*

not only on the galactic CR intensities, but even their spectral shape. For each CR species, the particle fluxes measured at Earth are deformed respect to the local interstellar ones, depending on the solar activity; this explains the low energy difference between, e.g., the old results from CAPRICE94 (Boezio *et al.*, 2000), HEAT95 (Barwick *et al.*, 1997) and AMS-01 (Alcaraz *et al.*, 2000).

1.4.3   Experimental evidence of a charge-sign dependent solar modulation

Neutron monitors data reflect the modulation effect of the solar wind on galactic protons, the most abundand component of cosmic rays: they present the characteristic periodic shape given by a more peaked profile during A- epochs and a flattish one during A+ solar cycle phases. This behaviour seems to indicate a different response of CR protons to different magnetic field orientations. Moreover, also Earth-measured electrons show a similar anti-correlation but the opposite peak-flat recurrence. Despite electromagnetic theory has an absolute symmetry under simultaneous interchange of charge sign and magnetic field direction, it seems that a charge dependent mechanism works in solar modulation: negative and positive particles behave differently under the same HMF configuration, while, once fixed the charge-sign, particles behave differently during different polarity epochs.

First indications that solar modulation effects depend on the CR sign of charge arose when comparing the helium flux versus the electron flux and the electron flux alone as a function of time for alternate solar cycles (Garcia-Munoz *et al.*, 1987; Tuska *et al.*, 1991). More recent Ulysses proton and electron measurements confirm this behaviour (Heber *et al.*, 2002, and references therein).

Charge sign dependent solar modulation effects have been clearly seen in the antiparticle to particle ratios both in the hadronic and in the leptonic channel. The BESS balloon-borne experiment have had the chance to measure the antiproton to proton ratio during a period of maximum solar activity, just before and after the most recent (2000) reversal of solar magnetic field. Data from Asaoka *et al.* (2002) are reported in Fig. 1.17. They show that low energy $\bar{p}/p$ values refering to the 2000 (A- epoch) measurements are increased respect to those performed during the opposite polarity cycle (1997 and 1999). The antiproton-to-proton flux ratio below 2 GeV measured by PAMELA shows good agreement with earlier measurements during similar periods of solar activity (Hofverberg, 2009).

  Similar low energy differences have also been observed in the positron fraction between measurements performed during different phases of the solar activity. Several balloon-borne experiments have detected electrons and positrons and have provided the data that
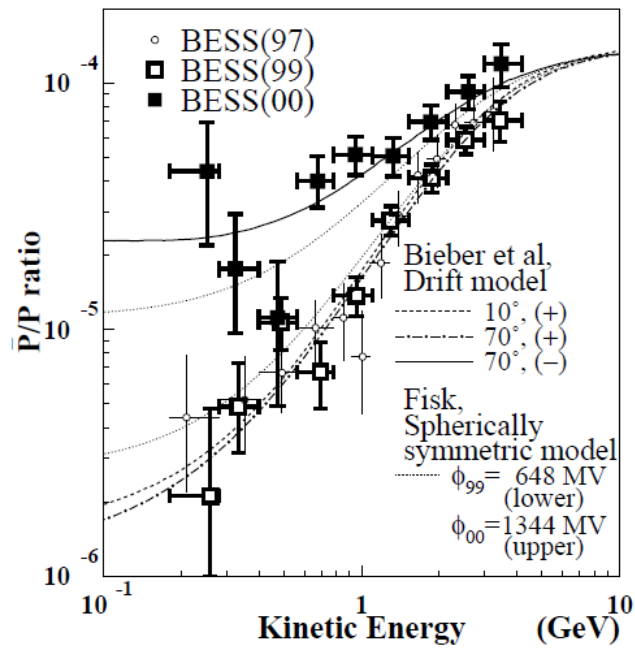
Figure (1.17) *The $\bar{p}/p$ ratio measured by BESS in 1999 and 2000 with the previous data in 1997. Theoretical calculation by several solar modulation models are also reported.*
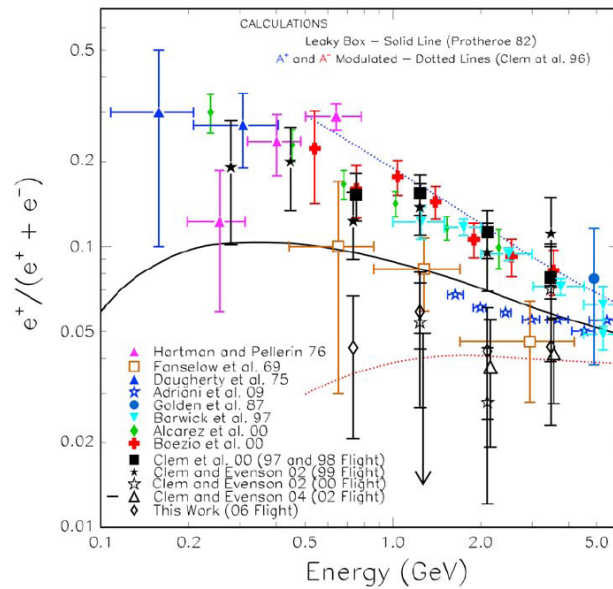
Figure (1.18) *Summary of the observed positron fraction for different epochs of solar magnetic polarity. Lines are the modulated abundance calculations (Clem and Evenson, 2009).*
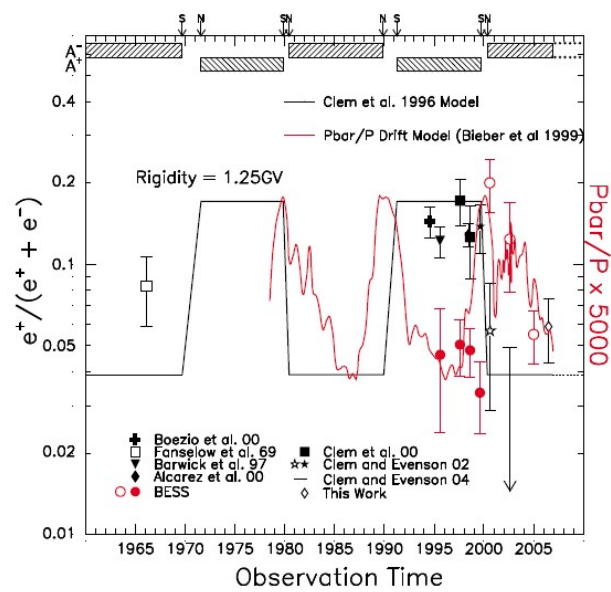
Figure (1.19)   *This figure from* Clem and Evenson *(2009) displays in black the positron fraction observations with rigidities* ~ 1.25 *GV, while in red the* $\bar{p}/p$ *at the same rigidity. Solid simbols refer to data taken in the A+ state, while open symbols refer to A-. The solid lines are the related predictions from a phenomenological model (*Clem et al.*, 1996).*

are reported in Fig. 1.18. A compilation of the existent measures is given in Table 1.1. Before the PAMELA launch, the only available data acquired during an A- solar minimum were those from Fanselow *et al.* (1969) and, more recently, from the 5-days long flight of the AESOP instrument in June 2006 (Clem and Evenson, 2009). One of the aims of this work of thesis is to extend to lower energies the experimental data for the positron fraction from PAMELA (Adriani *et al.*, 2009) and compare it with the existent ones. Measurements of the cosmic ray positron abundance at $\sim 1.25\ GV$ ordered in chronological order are in Figure 1.19. This plot clearly reveals the significant decrease of the positron fraction between 1999 and 2000 from the level remained relatively constant during the prior magnetic polarity (1990s), while the $\bar{p}/p$ ratio behaves differently.

| Reference	Platform type	Experiment observation period
(Adriani *et al.*, 2009)	spacecraft	July 2006 - February 2008
(Fanselow *et al.*, 1969)	balloon	five 1-day-duration flights, 5 July,
		5 August 1965; 10, 15, 26 June 1966
(Daugherty *et al.*, 1975)	balloon	two 1-day flights, July 1972
(Hartman and Pellerin, 1976)	balloon	two 1-day flights, 15 July, 3 August 1974
(Golden and et al., 1987)	balloon	20 May 1976
(Barwick *et al.*, 1997)	balloon	23-24 August 1995
(Alcaraz *et al.*, 2000)	spacecraft	2-12 June 1998
(Boezio *et al.*, 2000)	balloon	8-9 August 1994
(Clem *et al.*, 2000)	balloon	1 September 1997 and 29 August 1998
(Clem and Evenson, 2002)	balloon	16 August 1999
(Clem and Evenson, 2002)	balloon	25 August 2000
(Clem and Evenson, 2004)	balloon	13-14 August 2002
(Clem and Evenson, 2009)	balloon	2-6 June August 2006

Table (1.1) *Experimental low energy positron fraction data available before* PAMELA *.*

In order to provide a realistic description of the modulation which galactic cosmic rays undergo when they enter the heliosphere and travel through it, and to explain the observed charge-sign dependent effects, a lot of theoretical work has been done during the last 40 years. A strong input from experimental data taken in different magnetic epochs for oppositely charged particles is necessary in order to constrain the model parameters and reduce the uncertanties of the predictions.

1.4.4   Solar modulation models

Much effort has been put in developing solar modulation models that could account for the observed characteristics of the CR propagation in the heliosphere, reproducing any observable overall variation in the galactic CR intensity due to changes in the heliospheric conditions.

A widely used description is the hystorical force field model by (Gleeson and Axford, 1968). It is based on the assumption of a spherically symmetric heliosphere, whose corresponding Fokker-Plank equation has a solution given by the expression:

$$J(r, E_t, t) = J(r_{tm}, E_t + \Phi_p)[\frac{E_t^2 - m_r^2 c^4}{(E_t + \Phi_p)^2 - m_r^2 c^4}] \tag{1.8}$$

where $J(r_{tm}, E_t + \Phi_p)$ is the undisturbed CR intensity beyond the solar wind termination shock, Φ_p is a modulation parameter completely determined by the modulation strength called *force field energy loss*.

In this approximation the solar wind is assumed to affect the differential particle spectrum in a spherically symmetric way, resulting in an isotropic modulation effect. Despite its lack of capability in explaining any charge dependent modulation effect nor in introducing any possible anisotropy in the heliospheric transport, several authors use this model to calculate the expected secondary production background (see Sec. 1.3.4). This approach could, in principle, lead to the introduction of uncertainties that are, at low energy, of the order of the variation observed in the interested energy range (see Figures 1.18 and 1.17). More complex models explicitly take into account gradients and curvature drifts and neutral sheet drift in the HMF, and introduce anisotropies in the CR propagation.

Jokipii *et al.* (1977) pointed out that, although drifts were explicitly contained in standard transport theories, they had been neglected in previous models of galactic CR modulation. Their simulation for a simple Parker magnetic field shows that the order of magnitude of drift related effects, respect to the other modulation causes, is such that it cannot be neglected: the geometry of the magnetic field generates drift velocities which are greater than the solar wind velocity over much of the inner heliosphere. Note that the drift velocity direction is opposite for oppositely charged particles. The drift velocity pattern is described in the right panel of Fig. 1.20 for positive particles in different polarity epochs: positively charged particles are expected to drift into the inner heliosphere over the solar poles and out along the heliospheric current sheet during A+ epochs and to behave in the opposite manner during A- epochs. Several numerical steady-state drift models have been developed in the early 1980's, progressively increasing in sophistication during the time (Potgieter, 2008, and references therein), arriving to develop reliable 3D steady state, as well as 2D time dependent, models[12]. A common issue to all of them is the need of

---

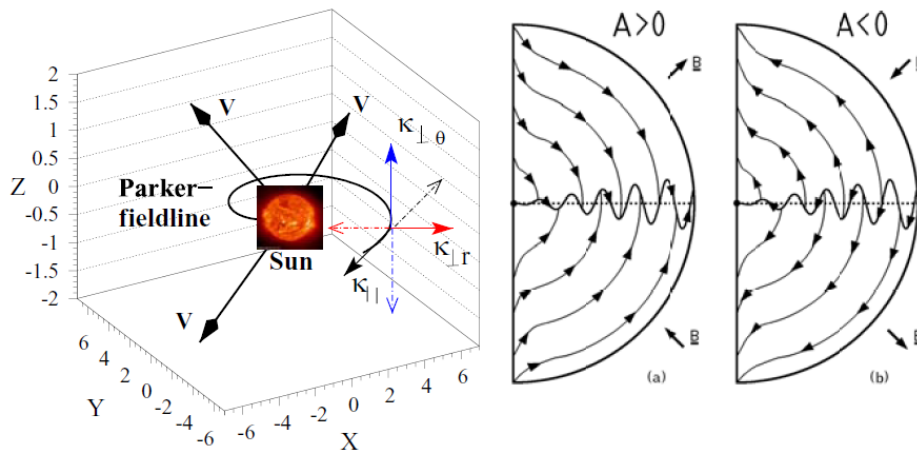[12]Issues related to computation do not allow yet to run a 3D time dependent model.

Figure (1.20) *Left: the Parker spiral and the different elements of the diffusion tensor. The arrows **V** indicate the velocity of the radially expanding solar wind. Right: The global drift pattern of positive particles during A+ and A- solar magnetic epoch, together with the neutral current sheet (Heber and Potgieter, 2006).*

basic information about the large scale heliosphere as input, in order to give a reasonable description of the galactic CR modulation over a 22-year cycle. The physical structure of the heliosphere is important as well as the knowledge about the solar wind profile and the HMF: data from Pioneer, Voyager and Ulysses missions are crucial in this sense. In particular, before the Ulysses launch in 1990, very little was known about the latitudinal dependence of the model parameters.

Besides a realistic description of the heliosphere, the local interstellar spectra (LIS) for different particles are needed as initial conditions at the simulated outer heliospheric boundary. Little is known about the unmodulated spectra and a lot of theoretical work has been done about. From the experimental point of view, contrary to the expectations, after the first Ulysses polar passage it became clear that it is impossible to determine the local interstellar spectrum in the inner heliosphere, so that it is necessary to wait for the Voyagers results, when they will leave the heliosphere and reach the interstellar space.

Modulation models are based on the numerical solution of the cosmic ray transport equation (Parker, 1965) for the omnidirectional distribution function $f(\mathbf{r}, p, t)$ of CRs with momentum p, at position $\mathbf{r}$ and time t:

$$\frac{\partial f}{\partial t} = \nabla \cdot \left(\mathbf{K}^{(s)} \cdot \nabla f \right) - \mathbf{V} \cdot \nabla f - \langle \mathbf{v_D} \rangle \cdot \nabla f + \frac{1}{3} \left(\nabla \cdot \mathbf{V} \right) \frac{\partial f}{\partial \ln p} + Q(\mathbf{r}, p, t) \quad (1.9)$$

where $\mathbf{V}$ is the solar wind velocity and $Q(\mathbf{r}, p, t)$ a source function.

Terms on the right-hand side represent the four mechanisms that seem to dominate the modulation of cosmic rays in the heliosphere: respectively, diffusion, convection, drifts (gradient, curvature and current sheet) and adiabatic energy losses. The last term is a source term (e.g. it could represent the jovian e^- source).

Diffusion is caused by irregularities of the HMF that scatter charged particles imparting them a random walk ruled by the diffusion tensor **K**. Parker (1964) succeeded in showing that a charged particle moving in large-scale field containing small-scale irregularities is most effectively scattered by irregularities which have a scale comparable to the gyroradius of the particle. In the IMF case, the scale of the irregularities appears to have dimension of $10^5 - 10^7 \ km$ so that protons with kinetic energy larger than $\approx 100 \ MeV$ and less than $\approx 10 \ GeV$ are more scattered.

Diffusion is ruled by the diffusion tensor **K**:

$$\mathbf{K} = \begin{bmatrix} k_{\parallel} & 0 & 0 \\ 0 & k_{\perp\theta} & k_A \\ 0 & -k_A & k_{\perp r} \end{bmatrix} \tag{1.10}$$

$\mathbf{K}^{(s)}$, that appears in equation 1.9, is the symmetric part of the diffusion tensor, consisting of diffusion coefficients parallel ($k_{\parallel}$) and perpendicular ($k_{\perp\theta}$ and $k_{\perp r}$) to the mean background HMF (see Fig. 1.20, left panel); the antisymmetric part contains the drift coefficient k_A that is related to the pitch angle averaged guiding center drift velocity $\langle \mathbf{v_D} \rangle$. The effective radial diffusion coefficient is given by $k_{rr} = k_{\parallel}cos^2\psi + k_{\perp r}sin^2\psi$, with ψ the angle between the radial and the averaged HMF direction; thus, while $k_{\parallel}$ dominates the radial diffusion in the inner heliosphere and in the polar regions, $k_{\perp\theta}$ dominates in the middle to outer regions of the heliosphere (Potgieter, 2008). If perpendicular diffusion is assumed to be isotropic $k_{\perp r} = k_{\perp\theta}$.

One of the main obstacles in solving the Parker equation is insufficient knowlegde of the spatial, rigidity and especially the temporal dependences of the elements of the diffusion tensor (DCs). In order to improve the situation a lot of work has been done in different directions: some authors try to formulate an 'ab initio' theory, in which the DCs are determined on the basis of scattering and turbulence theory and plasma physics; other approaches are partly based on fundamental theory but constraint by CR observations and others are primarily based on compatibility studies between simulation models and CR observation.However, all these models need to be tested against CR observations. As an example, an important prediction from drift-dominated modulation models was the expectation that protons would have large positive latitudinal gradients in A+ solar magnetic epoch. In contrast to the expectations, the Ulysses spacecraft measured a highly modulated spectrum over the poles. This result suggested that drifts were overestimated and that the diffusion perpendicular to the HMF could be anisotropic, significantly larger in the polar direction that in radial/azimuthal direction of the heliosphere. Thus, current

models employ the enhancement of the perpendicular diffusion by assuming[13] $k_{\perp\theta} > k_{\perp r}$. From (1.9) follows that the effect of the drift term introduces, through $\langle \mathbf{v_D} \rangle$, a dependence on the polarity of the HMF in the variation of the CR distribution function f, and therefore different density gradients depending on the drift effect importance. Moreover, if the density gradients are small, drift effects on modulation will also be very small, even if the drift velocities are quite large. Large values of $k_{\parallel}$ or $k_{\perp}$ will therefore automatically reduce drift effects even if k_A is kept unchanged.

The second term of the Parker equation (1.9) represents the outward convection caused by the radially directed SW velocity. As already mentioned, experimental data are necessary to give a representation of the heliospheric conditions as close as possible to the reality. An important contribution in this sense was the confirmation that $\mathbf{V}$ is not uniform over all latitudes but that it is divided into the fast and slow wind regions during solar minimum conditions (McComas *et al.*, 2000).
A part from the convection caused by the solar wind, the divergence of $\mathbf{V}$ is equally important because it describes the adiabatic energy changes of CRs. If $(\nabla \cdot \mathbf{V}) > 0$, CR ions experience large energy losses resulting in a characteristic spectral shape below few hundred MeV in the inner heliosphere. Beyond the TS $(\nabla \cdot \mathbf{V})$ may be mostly negative, that translates into an adiabatic heating, that could have interesting effects for anomalous cosmic rays (ACRs), such as an increasing intensity in the heliosheath that Voyager 1 should be able to measure in the next future (Langner *et al.*, 2006). Note that, at low energy, protons are much more affected by adiabatic energy losses than electrons, because of their higher masses.

The present understanding of the mechanisms of global modulation in the heliosphere, as described by the Parker equation, is considered essentially correct. A further effort has to be done in order to understand how the relative contribution of the mentioned mechanisms change and what causes these changes over a solar cycle: for recent years, an important aspect of theoretical and modelling studies has been to establish and understand the relative roles of the major modulation mechanism over a complete 22 year cycle.
Several model predictions have found confirmation in experimental data, on the other hand data continuously provide inputs to the models.
Figure 1.21 shows the computed CR proton intensities at Earth, at three energies, as a function of the tilt angle α (Potgieter *et al.*, 2001). Note that the tilt angle of the HCS has become a prime indicator of solar activity from a drift point of view: the wavy HCS is one of the most successful physical effects in CR solar modulation and it plays an important role in CR modulation (Smith, 2001), thus α can be considered still the best proxy for solar activity from a CR point of view. The plots show how the proton intensities differ

---

[13]This assumption is in apparent competition with the effect of a different configuration for the HMF, proposed by Fisk (1996), that is complex to be implemented in modulation models (Burger, 2005) but could have a significant effect in terms of latitudinal gradients.
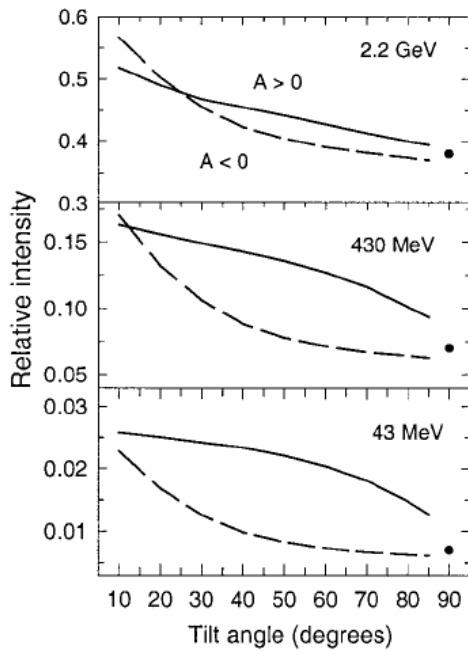
Figure (1.21) *Cosmic ray proton intensities at Earth as a function of tilt angle α computed for different energies by a steady-state drift model. The solid circles indicate the intensity for the non-drift case (Burger, 1999).*
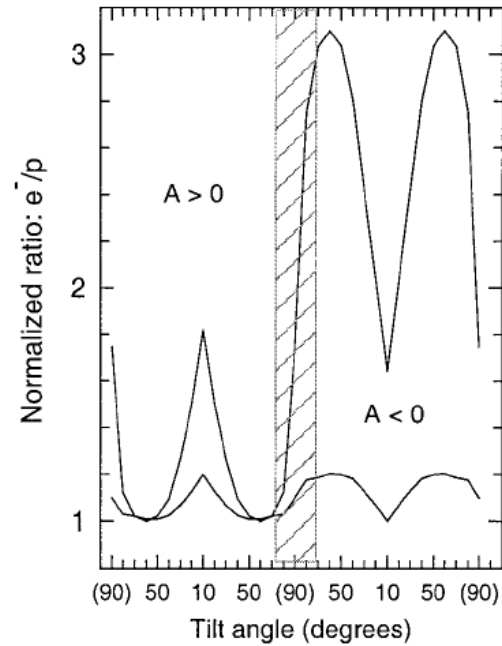
Figure (1.22) *Computed normalized ratio of CR electron to proton intensities at Earth for 1 GV (upper line) and 3 GV (bottom line) as a function of tilt angle. The shaded area represents the period of maximum modulation.*

for the two polarity epochs as a function of changing HCS. The tilt dependence is strong for the A- cycle when $\alpha <\sim 30°$, but for the A+ cycle it is the strongest with $\alpha >\sim 60°$, depending on the energy. It reflects the fact that positive particles tend to enter the heliosphere from the poles, during the A+ epochs, and leave it going along the current sheet because of drift. For the same reason drift explains the characteristic peaked-flattish shape of NM data: protons respond promptly to tilt angle variations when they drift along the HMF (A-) leading to a more peaked profile. For CR electrons the A+ and A- dependence would simply reverse.

One of the strongest predictions of drift models is that charge-sign dependent modulation should occurr. Potgieter *et al.* (2001) show the basic features of the normalized electron to proton ratio, reported in Fig. 1.22, with the remarkable 'W'-like shape of the ratio during the A+ cycle in contrast to the 'M'-like shape during the A- cycle. These features are clearly visible in observations made during the past (Heber and Marsden, 2001). However, note that a deviation of the normalized ratio of electrons to protons from unity does not necessairly indicate that drifts cause the charge-sign dependence: adiabatic energy losses are vastly different for electrons and protons at low energies. Moreover, helicity might also play a role (Burger *et al.*, 1997).

Recent measurements of the e/p ratio have been performed by the Ulysses spacecraft during the current solar minimum (Heber *et al.*, 2009) that, coupled to the model, allow to make some predictions. The data reveal a discrepancy between the measured intensities of $2.5\ GV$ electrons and protons respect to the previous solar minimum (1987). The authors interprete this result as indicating that the 'true' solar minimum conditions were not yet set at the time of the measure, and that indeed current sheet and gradient drifts prevent the GCR flux to rise to typical solar minimum values. Thus, they predict that the $2.5\ GV$ proton flux will still increase if the tilt angle will reach values below $10°$.

In order to reproduce the characteristic features of the GCR modulation during the whole 22-year solar cycle, to correctly interpret the data (e.g. the Ulysses' ones), and to make temporal predictions, a time dependent model is required. Ferreira and Potgieter (2004) combined time-dependent global changes in the HMF over 11-year cycle (Cane *et al.*, 1999) with time-dependent drifts, naming this approach the compound model, that turned out to be remarkably successful over a period of 22 years when applied at Earth and along the Ulysses and Voyager 1 and 2 trajectories.

By comparing the model results to the Ulysses data of 1990s there is indication that, while during the solar minimum activity drift effects are at their largest, they reduce with increasing solar activity and that, during extreme solar maximum conditions, the heliosphere becomes *diffusion (non-drift)* dominated (Ndiitwani *et al.*, 2005).

Thus, solar minimum activity periods are ideal to study drift because the 'footprint' of this effect is not hidden by the others. Drifts are effective in the energy range between few hundreds MeV and $\sim GeV$, as it is shown in Fig. (1.23) for electrons (Ferreira, 2002).

Models are also able to calculate the modulated particle spectra. Langner and Potgieter (2004) computed them for protons, antiprotons, electrons and positrons at several distances from the Earth and in different heliospheric conditions. Spectra result to have a characteristic shape depending on the assumed LIS and rigidity dependence of the diffusion coefficients. Then, oppositely charge particle ratios can be computed.

Despite the level of global understanding of the processes involved in the solar modula-
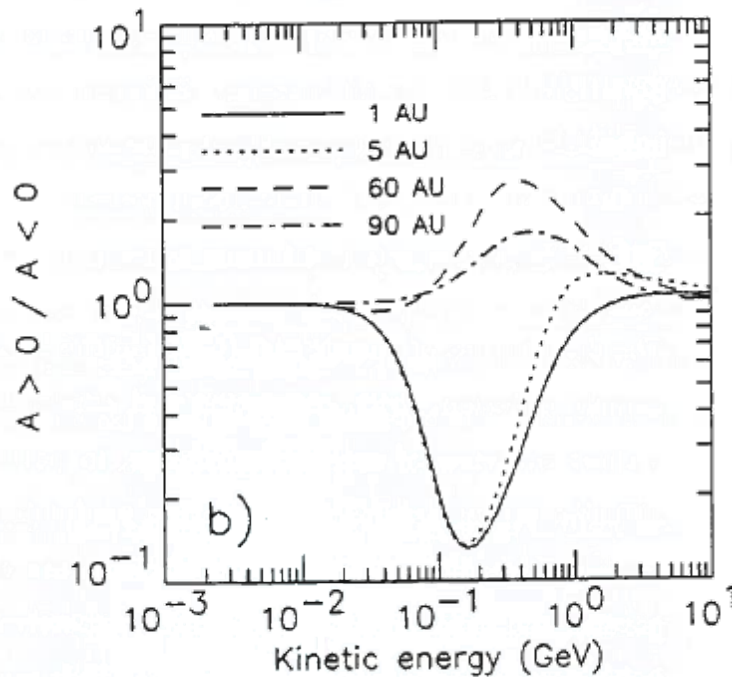
Figure (1.23)   *The ratio of A+ and A- electron spectra as calculated by Ferreira (2002) at several distances from the Earth*

tion still several issues need to be better studied and addressed (Potgieter, 2008), like what to use for the time dependence of the diffusion coefficients on top of what their steady-state energy and spatial dependence are in the inner heliosphere. Moreover improvements are desirable in better understanding how gradient and curvature drifts reduce with solar activity and how significant are the effects of the Fisk type HMF on the global CR modulation.

New experimental data for differently charged particles measured during the current solar minimum could help in improving the current understanding of CRs transport mechanisms in the heliosphere.

Chapter 2

The **PAMELA** Experiment

PAMELA [1] is a satellite-borne experiment designed to make long duration measurements of the cosmic radiation, optimized for the detection of the antiparticle component of cosmic rays (Picozza *et al.*, 2007). It was launched on June 15th 2006 from the Bajkonur cosmodrome on-board of the Resurs DK1 satellite and, since then, it is almost continuously taking data while following an high inclination (70°), elliptical orbit (350 × 610 km) whose period is 90 minutes. The mission lifetime, originally foreseen to be 3 years, has been extended for two additional years. The satellite orbital characteristics, the mission long duration and the instrument set-up make **PAMELA** particularly suited to study particles of galactic, heliospheric and trapped origin at 1 AU (Astronomical Unit).

2.1 Mission overview and scientific goals

The **PAMELA** (PAMELA official web page) experiment is the most recent endeavour of the Wizard Collaboration which has successfully built and flown a number of balloon experiments (MASS89, MASS91, Tramp-Si 93, CAPRICE94 and CAPRICE98) and a satellite experiment (NINA)devoted to the antiparticle detection in the cosmic radiation. The **PAMELA** collaboration consists of a number of European groups: The Royal Institute of Technology (Stockholm, Sweden), INFN and Physics Department of University of Rome (Italy), Moscow Engineering and Physics Institute (Russia), INFN and Physics Department of University of Florence (Italy), IFAC (Florence, Italy), INFN and Physics Department of University of Trieste (Italy), INFN and Physics Department of Naples (Italy), University of Siegen (Germany), INFN National Laboratory of Frascati (Italy), INFN and Physics Department of University of Bari (Italy), Ioffe Physical and Technical Institute (St Petersburg, Russia) and Lebedev Physical Institute (Moscow, Russia).

---

[1] Payload for Antimatter Matter Exploration and Light-nuclei Astrophysics.

The instrument is flying on board of Resurs DK1 satellite, thanks to the RIM (Russian-Italian Mission) collaboration, which since 1995 has allowed Italian CR experiments on the Russian space station MIR (SilEye experiments). The PAMELA experiment is not the only scientific device housed on the satellite: the Arina experiment for the detection of very low energy electrons and protons is also taking data while the satellite assolve its primary task, that is taking high resolution images of the surface of the Earth.

PAMELA is housed in a pressurized container (see Fig. 2.1, bottom panel) that keeps stable the environment at ideal working conditions for the instrument: it is filled with nitrogen that is kept at 1 atmosphere pressure and a temperature between $0°$C and $45°$ C. The container is connected to the satellite body (see Fig. 2.1, top panel) with a mechanical arm which can move the container from the parked position, in which it is kept during launch, to the position kept during data acquisition mode where the container points out to space. The part of the container above the instrument constitute a thin additional layer (aluminium 1.7 mm thick) that charged particles encounter before being detected.

PAMELA has been launched on board of the Soyuz FG rocket on the 15th of June 2006 from the Baikonour Cosmodrome[2] in Kazakhstan and will stay in orbit compatibly with the drag exerted by the solar activity. Since this solar minimum is exceptionally quite and long, the satellite has needed only one re-boost out of the three available, since the time of launch.

The satellite is travelling in a semi-polar orbit $70°$ at an altitude between 350 km and 610 km.The PAMELA detector is 1.3 m tall and has a mass of 470 kg. The average power con- sumption of PAMELA is 355 W, which is provided by the solar panels or batteries of the host satellite. Most of the power consumption powers the electronics of the instrument. Data are down-linked to the mass memory of the satellite during acquisition, and radio-linked down to earth when passing the ground center in Moscow, NTsOMZ.

The main scientific objective is the detailed measure of the antiprotons and positron component in CRs that can be performed in the most extended energy range to date and with a significant increase in statistics at high rigidity respect to previous experiments, as illustrated in Tab. 2.1. As discussed in the previous chapter, any observed deviation from the expected secondary spectrum could provide a hint for new physics scenarios, constraints for existing cosmological models or could be read as signals from local sources. Moreover PAMELA is extending the observational limit in the search of antihelium to the $\sim 10^{-8}$ in the antihelium-to-helium ratio and it is searching for exotic matter in the Universe.

Besides the primary objective to study antimatter, many additional scientific goals can be pursued. Light nuclei can be identified at least up to Z = 8. This provides complementary

---

[2]Baikonour Cosmodrome is famous for launching the satellite that brought the first man in space - Jurij Gagarin on the 12th of April, 1961.

data, besides antimatter abundances, to test models for the origin and propagation of CR. Moreover, thanks to the satellite low-cutoff orbit and the mission long duration, PAMELA can study low energy particles (down to 50 MeV) investigating several aspects of the solar and terrestrial environment. Measurements can be extended down to the solar-influenced energy region, providing data about spectra and composition of solar energetic particles and allowing solar modulation of galactic CR over the minimum between solar cycle 23 and 24 to be studied. Finally PAMELA is able to monitor trapped particles while traversing the Van Allen belts, and the variation of geomagnetic cutoff while passing through regions characterized by different latitude.

Particle	Number	statistics (3 years)
Antiprotons	80 MeV - 190 GeV	10^4
Positrons	50 MeV - 300 GeV	10^5
Electrons	50 MeV - 500 GeV	10^6
Protons	80 MeV - 700 GeV	10^8
Electrons + positrons	up to ~ 1 TeV (from calorimeter)	
Light nuclei (He/Be/C)	up to 200 GeV nucleon^{-1}	$10^{7/4/5}$
Antinuclei search	sensitivity of 3×10^{-8} in anti-He/He	

Table (2.1) *Design PAMELA performance.*

2.2 Instruments characteristics

PAMELA consists of a number of sub-detector, able to give information about mass, charge and velocity of the particles, that it can detect with a nominal acceptance of 21.6 $cm^2\ sr$. The core of the apparatus is a magnetic spectrometer, constituted by a permanent magnet and a 300 μm thick silicon microstrip tracker, that can reconstruct the track of the incident particle and measure the rigidity (impulse over charge ratio) with a Maximum Detectable Rigidity (MDR), measured on beam test, of about 1 TV.

A scintillator system (the Time of Flight system - ToF: three layers, each composed by two planes orthogonally segmented in bars) provides a fast trigger signal, that starts the acquisition of the whole system, and allows to measure the time of flight with a ~ 300 ps precision for protons, the arrival direction of the particle, the absolute value of the charge of the incident particles and, less precisely than the tracker, their position. The absolute value of the charge as measured by the ToF can be compared with that by the tracker and its sign is determined by use of the arrival direction of the particle and the bending direction in the 0.43 T magnetic field. This information allow to separate particles from an-
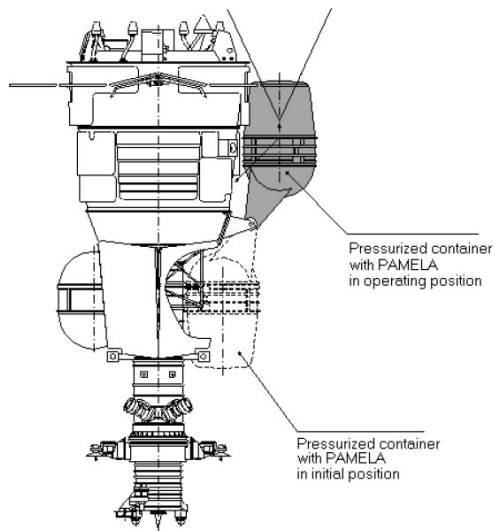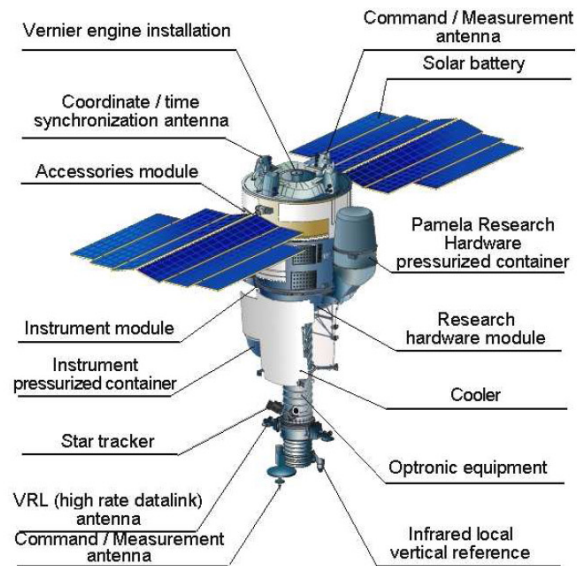
Figure (2.1)   *Resurs satellite (schematic view):* PAMELA *position is shown.*

tiparticles. A silicon-tungsten calorimeter (16.3 radiation lengths, 0.6 interaction lengths) measures the energy released by the incident particle and performs the hadron-lepton separation, providing topological and energetic information about the shower development in the calorimeter. The shower tail catcher scintillator and the neutron detector beneath help in the discrimination. An anticoincidence system is used to reject spurious events in the off-line phase.

The final identification is provided by a combination of velocity measurements by the ToF system, dE/dx measurements by the tracker and ToF system and by the interaction pattern in the calorimeter, as will be explained in detail in Chapter 3.
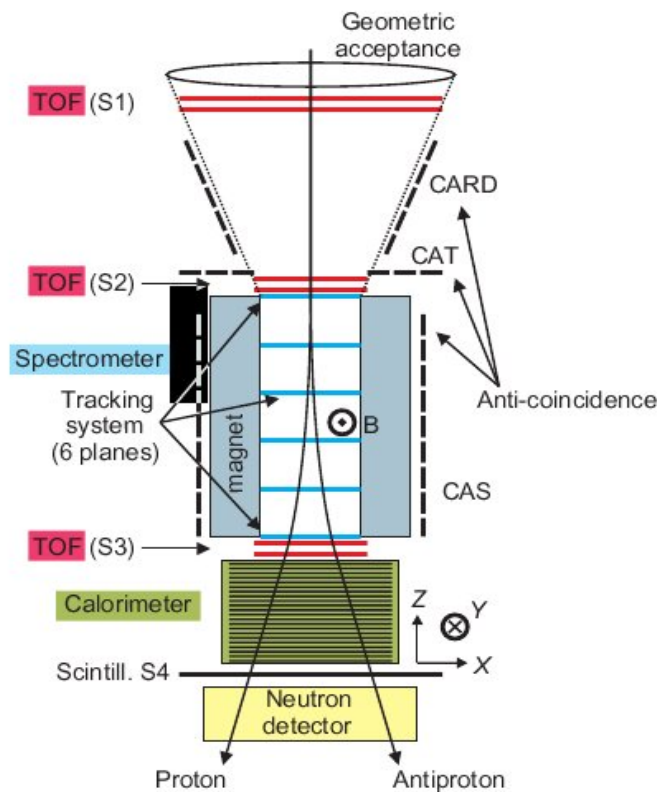
Figure (2.2) *Schematic view of PAMELA*

2.2.1 Time Of Flight system

The Time of Flight (ToF) system of the PAMELA instrument is constituted by layers of plastic scintillator coupled to photomultipliers allowing to perform the following aims:

- It provides a fast trigger signal that starts the acquisition of all the instrument sub-detectors.

- It measures the time of flight of particles passing between planes; this information is combined with track length information derived by the spectrometer to determine particle velocity ($\beta = v/c$).

- It can measure the incoming particle direction allowing the rejection of events associated to albedo particles and the measure of the incident particle sign of charge when this information is combined with the magnetic spectrometer one.

- It can determine particle charge up to $Z < 8$ by measuring ionization energy loss.

- Thanks to its segmentation, it can help the AC system in rejecting multi-particle spurious events.
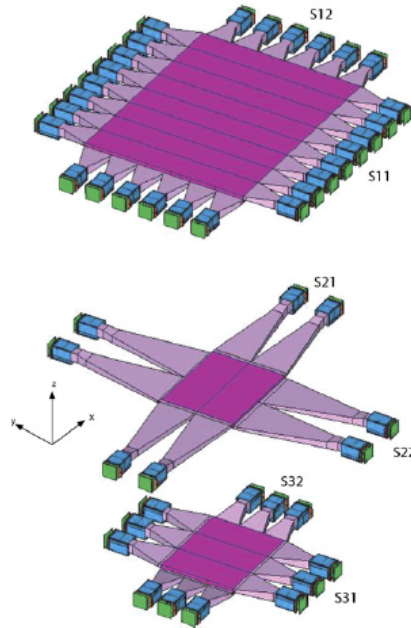
Figure (2.3) *Time of Flight System. From top to bottom: S1, S2 and S3 scintillator planes with their light guides and photomultipliers.*

The ToF system, shown in Fig. 2.3, comprises six layers of fast plastic scintillators (Bicron BC-404) arranged in three planes (S1, S2 and S3) each constituted by 2 layers orthogonally segmented in bars. The sensitive area of each of the two S1 layers is (33×40.8) cm^2 with the first layer divided into 8 bars and the second layer divided into 6 bars. The total sensitive area of the S2 and S3 planes is (15×18) cm^2 segmented into $2 \cdot 2$ and $3 \cdot 3$ orthogonal bars, respectively. The S1 and S3 layers are 7 mm thick while the S2 layers are 5 mm thick. The segmentation of each plane allows redundant studies of the

plane	layer	number of strip	Z (cm)	thickness (mm)	strip X dimension (cm)	strip Y dimension (cm)
S1	S11	8	+53.74	7	5.1	33.0
	S12	6	+53.04	7	40.8	5.5
S2	S21	2	+23.94	5	18.0	7.5
	S22	2	+23.44	5	9.0	15.0
S3	S31	3	-23.49	7	6.0	15.0
	S32	3	-24.34	7	18.0	5.0

Table (2.2) *This table summarizes the main geometric characteristics of the PAMELA Time of Flight system. The X, Y, Z coordinates are in the instrument reference system.*

trigger efficiency and adequate selections for single paddle hits allows the multi-particle events rejection. The ToF system geometry is summarized in table 2.2.

The distance between S1 and S3 is 77.3 cm, enough to allow the rejection of albedo particles with a significance of $\sim 30\ \sigma$.

The β resolution, as measured at beam tests is $\sim 70°$ ps for heavy nuclei and ~ 300 ps for protons. This allows, in combination with the information about rigidity from the magnetic spectrometer, to distinguish anti-protons from electrons and positrons from protons up to ~ 1 GeV, and to separate light isotopes at low energies.

2.2.2   Magnetic spectrometer

The core of the PAMELA instrument is a magnetic spectrometer consisting in 6 double-sided microstrip silicon detector planes uniformly positioned inside the cavity of a permanent magnet. The detector has been conceived to give a very precise measure of momentum $|\mathbf{p}|$ of the incident charged particles by reconstructing the track and measuring its deflection k in the magnetic field $\mathbf{B}$, and of the charge by detecting the ionization energy losses on the Si planes. The magnetic deflection is connected to the particle *rigidity* ρ by the relation $k = 1/\rho$ where ρ is defined as:

$$\rho = \frac{|\mathbf{p}|\,c}{ze} \tag{2.1}$$

where ze is the charge (z has sign, e is the electron charge). The rigidity is the parameter that univocally determines the dynamics of a charged particle in a magnetic field: particles

having different momentum and charge but same rigidity behave in the same manner under the action of the Lorents force. The following relation holds:

$$k \approx 0.3 \cdot \mid \mathbf{B} \mid \cdot \frac{z}{\mid \mathbf{p} \mid} \tag{2.2}$$

It follows

$$\rho \approx 0.3 \cdot \frac{\mid \mathbf{B} \mid}{k} \tag{2.3}$$

The 2.3 implies that, thanks to the knowledge of B and the measure of the magnetic deflection, it is possible to go back up to the incident particle rigidity and therefore, if the charge is known, to its momentum.

The permanent magnet is composed of 5 superposed identical Nd-B-Fe alloy modules shaped as right parallelepipeds with a central rectangular cavity. The cavity is characterized by a $16.14 \times 13.14 \ cm^2$ area a $43.66 \ cm$ height. The dimensions of the magnetic cavity for the PAMELA spectrometer have been chosen for an optimum compromise between a sufficiently high number of particles entering the geometric acceptance of the system and the possibility of achieving a precise measurement of their rigidity: a strong magnetic field in the cavity volume enhances the bending effect on the incoming particles and improves the overall performance of the spectrometer. The field intensity can be increased, once fixed the mass of the magnetic material, by reducing the cross-section of the cavity, with the drawback that in this way the geometric acceptance of the system is reduced and consequently also the number of particles that can be detected.
Each module is obtained by gluing together several magnetized elements, shaped as prisms with triangular section, and arranged in such a way to produce inside the cavity a quasi-dipolar magnetic field B with practically all the strength concentrated along he Y axis (the X and Z components are less than 10% of the Y component) and rather uniform; the presence of a preferential direction of the magnetic field greatly simplifies the algorithms for the reconstruction of the trajectory of the charged particle, whose curvature develops almost entirely in the XZ plane (bending plane). The magnetic field B inside the cavity shows a good uniformity: in the 80% of the volume it does not change by more than 10%. The maximum value of the field is 0.48 T at the centre of the cavity, the average value is 0.43 T. The spatial dependence of the magnetic field inside the cavity was measured with a three-axial Hall probe in 70000 points with steps of 5 mm. Any stray magnetic field outside the cavity can potentially interfere with the satellite instruments and navigation systems; in order to attenuate it, the magnet is enclosed by a ferromagnetic shielding.

The tracking system is constituted by six 300 μm thick silicon sensitive planes inserted inside the magnetic cavity. The high-precision double sided silicon sensors are
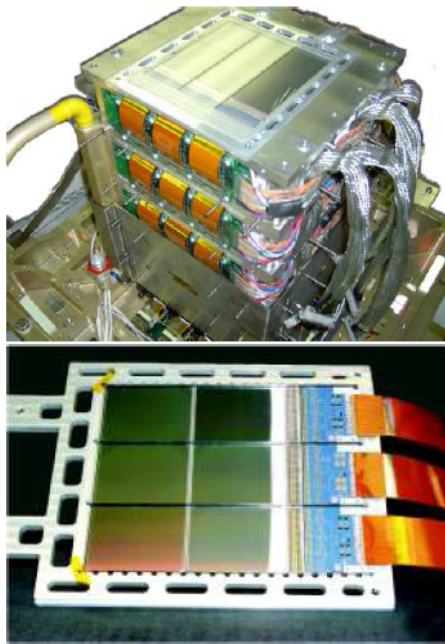
Figure (2.4) *Top: an overview of the magnetic spectrometer showing the top silicon plane. The magnet cavity has dimensions $(13.1 \times 16.1)cm^2$. A cooling loop enters from the left-hand side and the ADC boards mounted on the magnet canister are also visible. The lower part of the magnet canister is covered by a magnetic screen. Bottom: a silicon plane comprising three silicon strip detectors and front-end electronics.*

placed between the 5 magnetic modules and on the top and bottom of the magnetic tower, with equal spacing of 8.9 cm. Each detector plane is divided into three identical independent sections (known as ladders) along the X axis and housed in an aluminium support frame (see Fig. 2.4); each ladder is formed by two rectangular ($5.3 \times 7.0\ cm$) silicon sensors and a hybrid circuit, containing the first stage of the front-end electronics. The three components of a ladder are directly glued together.

The main characteristic of the **PAMELA** tracker planes is the presence of a sensitive layer both on the upper and lower side (or view) of the Si layer, with the implanted strips of one side orthogonal to those of the other, in order to achieve the measurement of both the X and Y coordinates of the crossing point of an incident ionizing particle.

Each silicon sensor (manufactured by Hamamatsu) is formed by a substrate of thickness $300\ \mu m$, with residual n-type doping and high resistivity; on one side 2035 p^+ parallel strips are implanted to form $p^+ - n$ junctions with the substrate, separated each other by a 25.5 m pitch. On the opposite side there are 1024 n^+ strips, with $67\ \mu m$ pitch, alternated to p^+ blocking strips; the $n^+ - n$ contact is of ohmic type. Since the junction view is characterized by a much better spatial resolution, it is used to measure the X coordinate of the impact point of the charged up to a value particle, which is by far the most important for the determination of the curvature of the trajectory, because the particle tends to bend in the XZ plane, normal to the main component of the magnetic field. For this reason the junction view is also indicated as X view or bending view; on the other hand, the ohmic side, measuring the Y coordinate, is indicated as Y side. During standard operation a voltage difference of +80 V (bias) is applied between the n^+ strips of the Y side and the p^+ ones of the X side so as to reverse-bias the $p^+ - n$ junctions and completely deplete the substrate. When an ionizing particle traverses the sensor, the $e^-/hole$ pairs, created in the depletion region, drift along the electric field lines toward opposite directions; holes are collected by the p^+ strips on the X side, e^- by the n^+ ones. From the distribution of the ionization charge collected by the strips it is possible to reconstruct the coordinate of the crossing point in the direction normal to the strips; besides, from the total collected charge on each side it is possible to determine the ionization energy loss of the particle across the Si layer.

The front end electronics system is based around VA1 Application Specific Integrated Circuits which contain 128 charge sensitive preamplifiers connected to shapers and a sample and hold circuit. The signals from VA1 chips are sent over 5 cm long kapton cables to be digitized by Analog-to-Digital (ADC) boards mounted on the magnet canisters.

The spatial resolution for the **PAMELA** spectrometer has been investigated with test beams that show a resolution of (3.0 ± 0.1) μm and (11.5 ± 0.6) μm in the bending and non-bending view respectively. Fig. 2.5 (left panel) shows the resolution in the bending view (Picozza *et al.*, 2007).

As above pointed out the precision in the measurement of rigidity obtainable by a magnetic spectrometer becomes worse for higher values of ρ, since the trajectory of the particle is less affected by the magnetic field and tends to a straight line. This in particular implies that it is more and more difficult to determine the sign of the rigidity, with a higher probability that a particle is wrongly identified as the corresponding antiparticle and vice versa. This effect is known as *spillover*. The quality of the measurement operated by a spectrometer, in the limit of high absolute values of the rigidity, is usually expressed in terms of the maximum detectable rigidity (MDR), defined as the absolute value of ρ for which the relative error in the measurement is equal to 100% or, in other terms, for which $\Delta\rho = \rho_{sp}$. The upper rigidity limit for detecting cosmic ray particles such as protons, helium nuclei and heavier nuclei is directly connected with the MDR, while for antiparticles the situation is complicated by their low abundance in the cosmic radiation and the presence of more abundant background particles: the discrimination of antiparticles from the corresponding particles can be performed up to a value ρ_{sp} for which the spillover background and antiparticle signal are comparable. Fig. 2.5 (right panel) shows the resulting rigidity measurement error versus rigidity obtained from proton test beams: a MDR of 1 TeV can be inferred from this plot.

While at high momentum the measurement error is mainly due to the finite spatial resolution in measuring the impact point on the detecting planes, at low momentum it is mainly dictated by the multiple Coulomb scattering of the particle as it crosses the tracker material. As previously pointed out, the use of double sided Si sensors tends to minimize this effect. Fig. 2.5 shows the rigidity measurement error to rigidity ratio versus rigidity obtained by simulation for electrons at low energies; electrons, because of their low mass, tend to suffer multiple scattering more than protons. The associated error is linked to momentum and velocity by the following relation:

$$\frac{\Delta p_{ms}}{p} \propto \frac{1}{\beta} \tag{2.4}$$

The possible changes of direction caused by multiple scattering in the detector planes must be taken into account for the correct reconstruction of the trajectory in the magnetic cavity, contributing to the overall uncertainty in the measurement of the curvature.

After the launch a software alignment procedure has been applied to the tracker in order to correct the displacements of the 36 sensors that is introduced during construction, shipment and, in particular, the launch, respect to the nominal positions.
Six parameters are defined (three translation coordinates and three rotation angles) whose values are used for the correction. They can be obtained by real data selecting particles with a known deflection and comparing the expected coordinates with the measured coor-
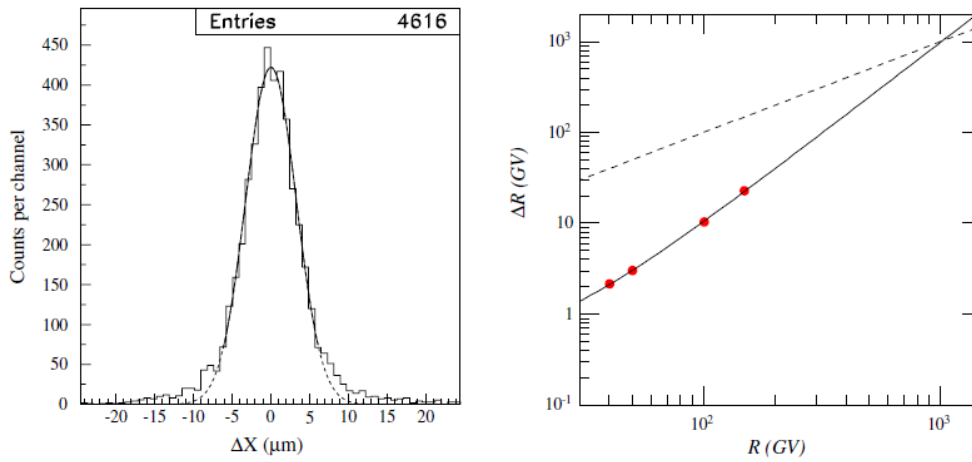
Figure (2.5)   *Left: The spatial resolution of the tracker in the bending view. The line indicates a Gaussian fit. Right: the deflection error ΔR measured by the magnetic spectrometer as a function of R (rigidity) obtained with proton beams. The dashed line is the bisector $\Delta R = R$. The functional form used to describe the experimental ΔR curve is obtained by assuming that two effects contribute to the deflection uncertainty, namely multiple scattering and spatial resolution. The former can be expressed (in the limit $\beta \sim 1$) as $\Delta k_{ms} \propto 1/R$. The latter is defined by $\Delta k_{res} = K$, where K is a constant. The intersection of the two curves gives the maximum detectable rigidity of the spectrometer.*

dinates, then from the residuals of the comparison, a χ^2 can be calculated and minimized. The parameters that minimize the χ^2 are choosen for the alignment. High energy electrons are used to this purpose, being their rigidity independently measured by the calorimeter.

2.2.3   Calorimeter

The electromagnetic calorimeter is used to measure the energy released by interacting e^+ and e^- and reconstruct the spatial development of showers: thus it's possible distinguish between electromagnetic showers, hadronic showers and particles passing straight through the detector.

The main issue of the calorimeter is distinguish positrons over protons background and antiprotons over electrons background. The first of this issues has been subject of this work.
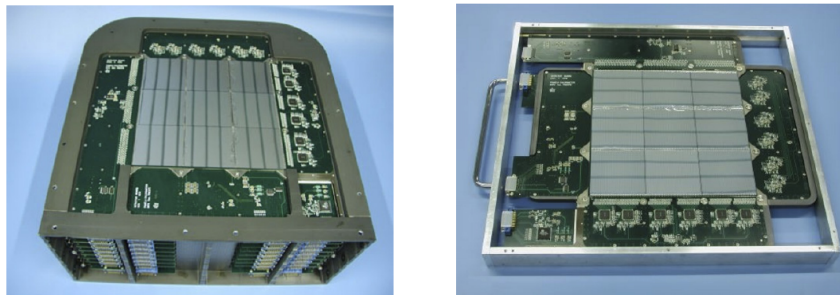

Figure (2.6)   *Left: The PAMELA electromagnetic calorimeter with the topmost silicon plane visible. The device is ~ 20 cm tall and the active silicon layer is $\sim 24 \times 24$ cm^2 in cross-section. Right: Detail of a single calorimeter module comprising a tungsten layer sandwiched between two silicon detector planes.*

The calorimeter is a sampling detector made of silicon sensor planes interleaved with plates of tungsten absorber. Each tungsten layer has a thickness of 0.26 cm corresponding to 0.74 X_0 (radiation lengths). Because the tungsten layers are 22 the total depth expressed in radiation lengths is 16.3. The nuclear interaction length is about 0.6. Each tungsten plane is sandwiched between two layers of silicon detector planes oriented orthogonally to each other.

The silicon sensor planes consists of 3×3 silicon detectors with an area of 8×8 cm^2. The detectors are separated from each other from a non-sensitive area 35 mm wide. Each silicon detector is 380 μm thick and segmented into 32 strips. Each strip is connected along its longitudinal axis with the adjacent strips. Each "long" strip has its own read-out channel so for each plane there are $32 \times 3 \times 2 = 192$; totally they are $192 \times 22 = 4224$.

Two detection planes form a detection module. Each module can be separately inserted into the aluminium frame (see 2.2.3).

The calorimeter can also operate in self trigger mode allowing the stand-alone detection of e$^{\pm}$ with a geometrical factor increased up to 470 cm^2sr with a maximum energy of 2 TeV. At 1 TeV the energy resolution is $\approx 16\%$.

More details about the characteristics of the interactions of charged particles in the calorimeter, and about its usage for distinguishing between hadrons and leptons, will be given in chapter 3.

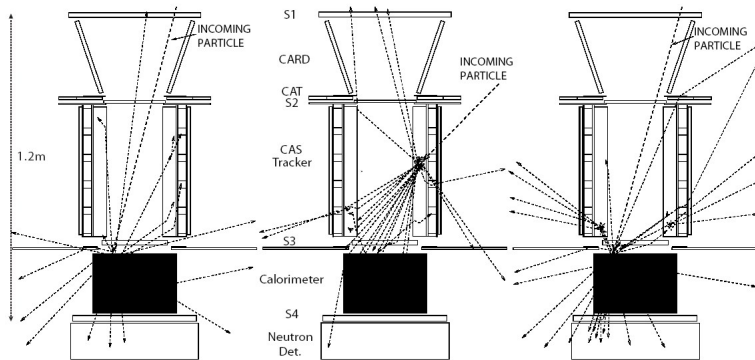## 2.2.4 Anticoincidence system

Figure (2.7)   *Schematic representations of simulated proton interactions in the PAMELA apparatus (non-bending view shown). Left: a good trigger event without anticoincidence (AC) activity, with the lateral AC system (CAS) represented by the outermost rectangles bracketing the tracker. Centre: a false trigger created by a particle entering the apparatus from the side generating a shower and AC activity. Right: Particles backscattered from the calorimeter can also give rise to AC activity for good trigger events.*

The aim of the anticoincidence systems (AC) is to identify, during off-line data analysis, events originating 'false triggers', acting as a veto shield: simulations have shown that the majority ($\sim 75\%$) of triggers in orbit are associated to coincidental energy deposits in the time-of-flight scintillators generated by secondary particles produced in the mechanical structure of the experiment, as shown in Fig. 2.7.

The AC system consists of nine plastic scintillators: as visible in Fig. 2.2, four of them (CAS) cover the sides of the magnet, four (CARD) surround the empty cavity between S1 and S2 and one (CAT) is placed just on top of the magnet, with a rectangular hole corresponding to the acceptance of the experiment. Their efficiency in detecting charged particles is measured to be 99.9%.
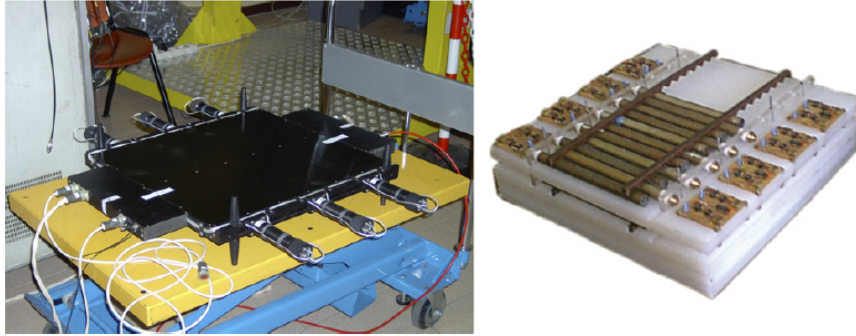
2.2.5   Bottom scintillator

Figure (2.8)   *Left: the shower tail catcher scintillator, S4, showing the six PMTs used for read-out. The scintillator has dimensions (48 × 48) cm^2. Right: The neutron detector partially equipped with ^3He proportional counters. The neutron detector covers an area of (60 × 55) cm^2.*

The shower tail catcher scintillator (S4) improves the PAMELA electron-hadron separation performance by measuring shower leakage from the calorimeter. It also provides a high-energy trigger for the neutron detector.

S4 is a plastic scintillator located below the calorimeter and just above the neutron detector. It is a single scintillator with an area 48.2 × 48.2 cm^2 and 1 cm thick which is read out by 6 photomultipliers (see Fig. 2.8, left).

S4 is used both to detect showers not fully contained into the calorimeter and, when their signals exceed a given value, to trigger a signal for neutron detector reading.

2.2.6   Neutron detector

The neutron detector complements the electron-proton discrimination capabilities of the calorimeter by measuring the neutron over-production that is present in case of hadronic showers respect to electromagnetic ones: in hadronic interactions neutrons are produced as secondaries while they accompany electromagnetic interaction just in case of the excitement of a giant resonance:

$$\gamma +^{74} W \longrightarrow A^* \tag{2.5}$$

the excited nucleus A^* produces a number s of neutrons and k of protons:

$$A^* \longrightarrow A + sn + kp \tag{2.6}$$

The device, shown in Fig. 2.8 (right), is located below the S4 scintillator and consists of 36 ^{3}He filled proportional counters surrounded by a polyethylene moderator in a thin cadmium layer. The moderator is used to slow down neutrons produced by hadronic showers, reducing their velocity v to let them interact with ^{3}He, since the related cross section depends on $1/v$. The associated interaction produces protons as signal carriers, according to the reaction:

$$n +^3 He \longrightarrow p +^3 H + 765 \ KeV \tag{2.7}$$

The cadmium layer prevents thermal neutrons entering the detector from the sides and from below. The 36 counters are stacked in two planes of 18 counters both oriented along the non-bending view. Its size is $60 \times 55 \times 15$ cm^3.

2.3   **PAMELA** data acquisition and trigger systems
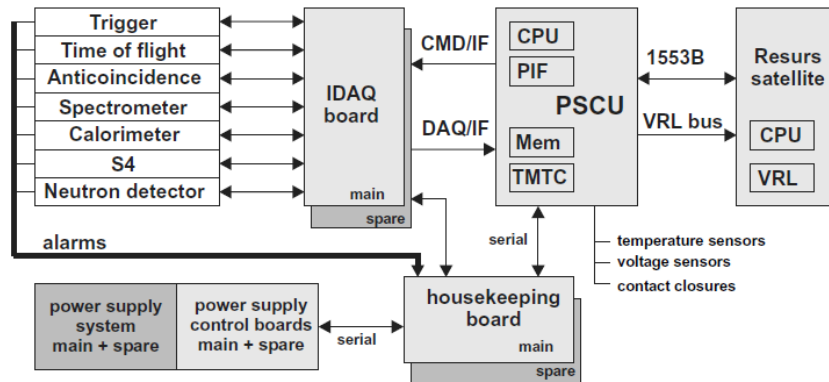
2.3.1   Data acquisition system

Figure (2.9)   *Scheme of the PAMELA data acquisition system. The interfaces (IF) between the IDAQ and the PSCU handle the data acquisition and transfer the commands (CMD) to the IDAQ. The communication between PAMELA and the spacecraft is handled by the 1553B bus and by the link to the VRL module for data download to the Resurs memory.*

A schematic overview of the PAMELA data acquisition (DAQ) system is shown in Fig. 2.9. The PSCU (PAMELA Storage and Control Unit) handles all slow controls, communication with the satellite, data acquisition, storage and downlink tasks. The PSCU contains four subsystems:

- A processor module built around a CPU based on a ERC-32 architecture (SPARC v7 implementation) running the RTEMS real time operating system at 24 MHz. The CPU is custom built by Laben and is fully space qualified. There is no redundant back up. Communication with the Resurs satellite is realised via a standard 1553B data-bus.

- Two redundant 2 GByte mass memory modules. The modules include latch-up detection, allowing operation to be transparently switched to the safe module when a latch-up is detected.

- A PIF (PAMELA interface board) that performs three main tasks: communication with the IDAQ (Intermediate DAQ) system through a DMA (dynamic memory access) controller, handling the interface with the mass memory, and providing the interface with the VRL (Very high-speed Radio Link) module of the satellite.

- A TMTC (Telemetry and Control) board that handles the housekeeping operations of PAMELA , such as alarm, temperature and voltage monitoring (once per second). Such monitoring is performed both directly (ADC inputs and contact closure telemetries) and through a dedicated housekeeping board that communicates through serial data links with the sub detector read-out boards, with the IDAQ board and with the power supply control boards.

Data acquisition from the subdetectors is managed by the IDAQ system at a rate of 2 MByte/s. Upon receipt of a trigger, the PSCU initiates the IDAQ procedure to readout data from the subdetectors in sequence. The resulting data are stored in the PSCU mass memory. Several times a day, the data are transferred to the satellite on-board memory via the 12 MByte/s VRL bus where it is stored prior to downlinking to earth. Approximately 15 GBytes are transferred to ground per day during 23 downlink sessions. The PSCU automatically handles the flow of PAMELA physics tasks and continuously checks for proper operation of the apparatus. At boot, the PSCU manages the operation of the power supply system to power up all subsys tems, initializes all detectors and starts the data acquisition cycle. In parallel, once per second the PSCU checks the TMTC information on voltages and alarms. In case of abnormal conditions the PSCU can perform a hardware reset of the whole system or, if insufficient to solve the problem (e.g. in case of electronics latch-up), powers down and then up PAMELA . The PSCU also checks the temperature environment by reading dedicated temperature sensors distributed in various locations around the instrument. If the readings exceed predefined values (set with dedicated commands from ground) the PSCU powers down PAMELA until acceptable working conditions are reached. The PSCU also handles communication with the Resurs satellite CPU and VRL system. Data is downloaded to the VRL upon receipt of a dedicated command from the Resurs CPU. The scheduling of data downloads from the PAMELA mass memory to the

VRL hard disk system is defined from ground on a daily basis. The PSCU organizes the data acquisition cycle in 'runs'. A run is defined as a continuous period of data taking in which the trigger and detector configurations are constant. These configurations are defined by the PSCU according to information stored in on-board memory or received from ground. The duration of a run is determined by the PSCU according to the orbital position (e.g. inside radiation belts or South Atlantic Anomaly SAA or outside these areas). The orbital position also dictates the trigger configuration, as described in the following section. The orbital position is derived from the 'ascending node' notification issued by the Resurs CPU when the satellite crosses the equator from the southern hemisphere to the northern hemisphere. From this position information, the CPU extrapolates the entry time into high radia tion environments. This can be performed in three ways, chosen from ground

- when the counting rate of the S1 scintillator exceeds a given threshold (changeable from ground with dedicated command);

- according to fixed time periods conservatively chosen and modifiable from ground;

- according to a table with crossing times in absolute Moscow time provided on a bi-weekly basis from ground with a dedicated command.

Additionally, the PSCU can interrupt and close a run if anomalous conditions that require action upon the subsystems (e.g. hardware resets, etc.) are detected. Periodically the PSCU calibrates the detectors, namely the anticounter system, the tracker, the calorimeter and the S4 scintillator. By default, the calibration is performed at the point of lowest CR trigger rate, i.e. the equator, upon receiving an 'ascending node' notification from the Resurs CPU. The frequency of calibrations can be modified from ground.

2.3.2   Trigger system

The PAMELA trigger condition is defined by coincident energy deposits in the scintillator ToF layers. Various configurations can be selected. The default ones used outside and inside radiation environments are:

- (S11 or S12) and (S21 or S22) and (S31 or S32) outside radiation belts and SAA;

- (S21 or S22) and (S31 or S32) inside radiation belts and SAA;

since, according to simulation, the radiation environment will saturate the S1 counting rate but will not affect significantly the S2 and S3 scintillators since they are more shielded.

These trigger configurations can be changed from ground with dedicated commands to the PSCU. A total of 29 configurations have been implemented on the trigger board.
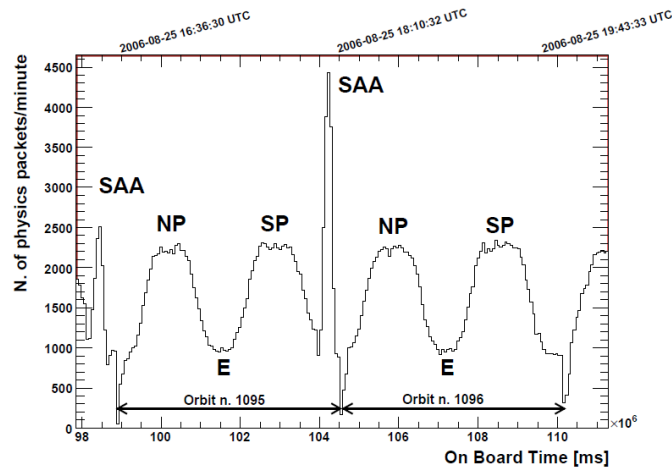
Figure (2.10)   *The PAMELA trigger rate shown in events per minute evaluated during two consecutive orbits (period ∼ 94 min). The trigger rate is strongly dependent on the orbital position: NP, North Pole; SP, South Pole; E, Equator; SAA, South Atlantic Anomaly (SAA).*

Various combination of and or or of the scintillators layers with or without the calorimeter self-trigger and S4 trigger are implemented and the PMTs can be masked on the trigger board by the PSCU.

The calorimeter is equipped with a self-trigger capability. A trigger signal is generated when a specific energy distribution is detected in predetermined planes within the lower half of the calorimeter. The sets of planes used in this configuration can be changed with a dedicated command from ground. This allows PAMELA to measure very high-energy (300 GeV to > 1 TeV) electrons in the cosmic radiation. At present, very few measurements have covered this energy range. Since these events are rare, it is important to have a large geometrical factor. By requiring that triggering particles enter through one of the first four planes and cross at least 10 radiation lengths, the geometrical factor is $600 \; cm^2 \; sr$, i.e. about a factor of 30 larger than the default PAMELA acceptance defined by the magnetic spectrometer.

The trigger rate observed during typical orbits is shown in Fig. 2.10. The maxima at ∼ 2200 events per minute (∼ 35 Hz) correspond to passages over the polar regions (North Pole, NP and South Pole, SP) while the minima (∼ 15 Hz) correspond to equatorial regions (E). The contribution from the South Atlantic Anomaly (SAA) is clearly visible (∼ 70 Hz, maximum). Note that data is taken in the SAA using the second default trigger configuration. The missing acquisition time after the peaks of the SAA corresponds to the detector calibrations upon crossing the equator (about 1 min in duration). Dead and live times are monitored by two clocks that count the time during which the data acquisition

system is busy or is waiting for a trigger, respectively. The dead time varies significantly over an orbit, due to the significant changes in trigger rate shown in Fig. 2.10. Furthermore, if the satellite crosses the SAA the dead time increases. The dead time also depends on the trigger configuration. For an orbit not crossing the SAA the fractional dead time is approximately 26%, i.e. the fractional live time is about 74%. As discussed previously, an automatic procedure changes the trigger configuration when entering radiation environments thus reducing the trigger rate and, consequently, the dead time.

Large solar particle events (SPE) can lead to a high rate of particles hitting the top scintillator. Although very large events such as the one observed on 24th October 1989 could result in rates of ~ 7 MHz on S11, most SPE will occur at solar minimum and will be of much smaller intensity. For example, a coronal mass ejection such as that of 24th September 1997 would result in a S1 rate of less than 100 Hz, much less than that encountered in the SAA (~ 1 kHz). For large events the automatic trigger selection procedure would switch to a configuration without the S1 detector, as currently happens during passages through the SAA. After this, a specific trigger configuration suited to the size and expected temporal evolution of the event can be selected from ground. If the amount of event data exceeds the storage dedicated to PAMELA on-board the Resurs satellite or the daily downlink limit, an on-line event selection is provided by a second level trigger. The second level trigger is not normally activated and must be activated via an uplinked command from ground. Information from the CAS anticoincidence system is used to reject 'false' triggers and information from the calorimeter is used to reduce the impact of particles backscattered from the calorimeter.

2.4   PAMELA first results: $\bar{p}/p$ and $e^+/(e^+ + e^-)$ ratio

Recent data from the PAMELA experiment about antiprotons and positrons are reported in Fig. 2.11 and 2.12. They show a steep increase in the energy spectrum of the positron fraction above 10 GeV up to 100 GeV, compatibly with previous hints from TS93 and HEAT, while they show no excess in the $\bar{p}/p$ energy spectrum, compared with the predicted background.

As pointed out in the previous chapter, a careful estimate of the expected antiparticle secondary production is very important in order to identify possible primary sources of antiprotons and positrons. According to a recent work from (Delahaye *et al.*, 2009), the positron background has been estimated with an uncertainty on the flux that reaches about one order of magnitude. If a realistic *hard* electron spectrum (spectral index $\gamma \approx 3.35$) is considered then a sizeable e^+ excess is present in the PAMELA positron fraction data, suggesting the existence of other primary sources and triggering a wide range of possible
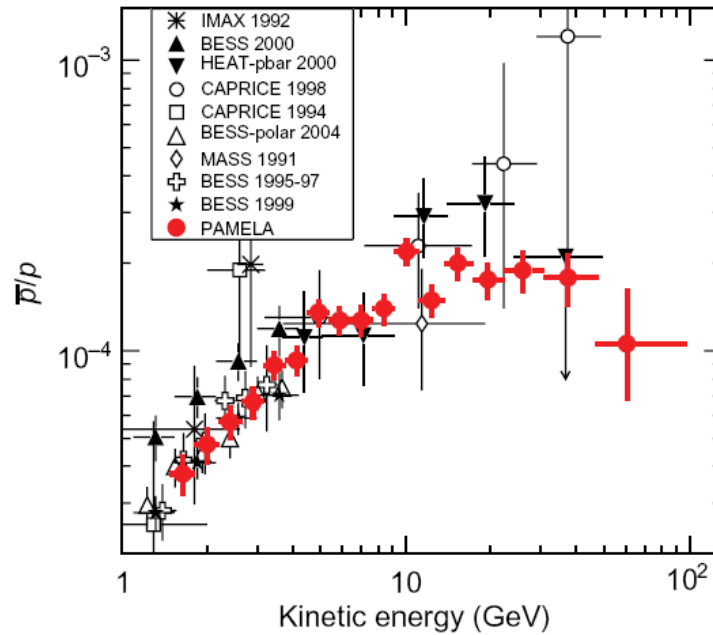
Figure (2.11) *PAMELA antiproton-proton flux ratio compared with previous measurements.*

interpretations[3]. The main characteristic of the picture offered by the PAMELA data is the asymmetry between leptonic and hadronic data. Purely astrophysical sources as pulsars or few nearby supernova remnants (SNRs) can reproduce quite naturally this asymmetry, on the other hand an interpretation in terms of dark matter annihilation or decay is very suggestive. In the following both the scenarios will be presented.

If the PAMELA e^+ and $\bar{p}$ data are interpreted in terms of dark matter, by studying models that can reproduce the experimental results, it is possible to constrain the DM particle mass, annihilation cross section and main annihilation mode. Because of the observed asymmetry between the leptonic and hadronic channel, a simple distinction between DM candidates arises (Pato *et al.*, 2009): leptophilic, that annihilate mainly in lepton pairs, and hadrophilic, whose annihilation final state are gauge bosons or quark pairs and that induce a non-negligible flux of both positrons and antiprotons. As pointed out by Cirelli *et al.* (2009), in case of DM particles dominantly annihilating into leptons there is no strong preference for the DM candidate mass; in the other case the DM particles annihilates into hadrons and their mass is estimated to be $\geq 10\, TeV$.

This is a quite unexpected scenario being not the most suitable for one of the most popular dark matter candidates, the *neutralino*: a very high mass neutralino is not in a favored part

---

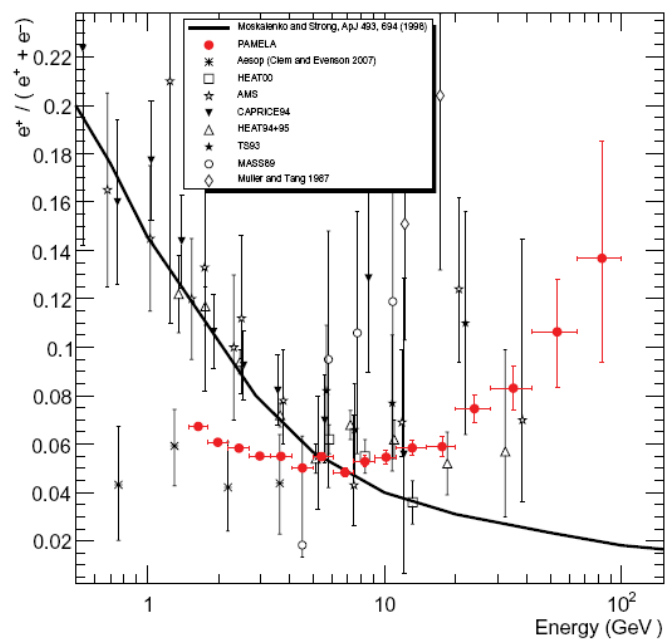[3]An extensive list of references can be found in (Profumo, 2008).

Figure (2.12)   *PAMELA positron fraction compared with other experimental data. The solid line shows a theoretical calculation (Moskalenko and Strong, 1998) for a pure secondary positron production during the propagation of CRs in the Galaxy.*

of the supersymmetric phase space, moreover, as a Majorana particle it cannot annihilate into light fermions with large rates, due to helicity suppression. Bergström *et al.* (2008) suggested a mechanism that could overcome this problem: radiative corrections that could enhance the e^+ DM signal without affecting the $\bar{p}$ one. It has been suggested in addition that new light mass bosons may mediate the annihilation suppressing kinematically the $\bar{p}$ production (Cholis *et al.*, 2008).

Alternatively, in respect of the observed asymmetry, the extradimensions theory provides a suitable DM candidate with the lightest Kaluza-Klein particle. In this scenario the lightest stable particle is a boson with direct annihilation channel into e^+ e^- pairs with no helicity suppression factor.

The order of magnitude that can be inferred by the PAMELA data for $\langle \sigma_A \ v \rangle$ is $\sim 10^{-23} \ cm^3 \ s^{-1}$; this implies that any explanation in terms of dark matter annihilation requires some enhancement mechanism. The positron signal from dark matter annihilation could be 'boosted' by a non-homogeneous dark matter distribution, presenting clumps and overdensities (Bertone *et al.*, 2009) that would enhance the annihilation rate and, consequently, the antimatter signal. A boost factor ranging between 10^2 and 10^4 would be required in order to explain the PAMELA excess, but such a high value is considered strongly disfavoured according to recent analysis (Lavalle *et al.*, 2008).Another possibility can be also considered, in which the boost does not come (or not only) from an enhanced dark matter density but from a larger cross section. Several scenarios have been proposed, invoking mechanisms such as non-thermal production of dark matter in the early Universe (Kane *et al.*, 2009), near resonance effects (Ibe *et al.*, 2009) or the so-called Sommerfeld enhancement (Arkani-Hamed *et al.*, 2009; Pospelov and Ritz, 2009).

It is important to notice that PAMELA measurements can be correlated to other kind of observations since dark matter annihilation can in principle also produce significant fluxes of photons, neutrinos and other secondary particles; moreover positrons lose energy by syncrotron radiation emission during their propagation. As an example, Pato *et al.* (2009) show that radio observations pose severe constraints on models viability; other indications come from direct searches and acceleration experiments. Thus it is very useful to adopt a multi-messenger approach when trying to interpret experimental results.

Besides the interpretation of the PAMELA data provided by exotic models, an other one, based on astrophysical reasoning, has been suggested in several recent works. Many authors consider pulsars as an alternative source of the observed signal (Hooper *et al.*, 2009; Serpico, 2009; Lineros, 2009; Grimani, 2007). Positrons can be produced in the magnetosphere of this rapidly spinning, magnetized neutron stars (see for example Atoyan *et al.* (1995)): electrons can be accelerated in different regions of the pulsar magnetosphere and induce an electromagnetic cascade through the emission of sincrotron radiation gamma rays above the threshold for pair production. Then electrons and positrons can escape the

magnetic field after joining the pulsar wind.

Models usually do not consider possible contributions from pulsars younger than $\sim 10^5$ years, that are likely still surrounded by their nebulae, which confine the e^- and e^+ and prevent them from beeing released in the interstellar medium; moreover, only pulsars less than 1 Kpc away can contribute significantly to the positron energy spectrum (Yüksel *et al.*, 2009), because of energy losses. According to Hooper *et al.* (2009), a significant contribution is expected from the sum of all mature pulsars throughout the Milky Way, as well as from the most nearby mature pulsars. Very recently the Fermi gamma-ray space telescope has revealed 'silent' pulsars, not seen in radio, that increase the set of known sources.

It is clear that, in this scenario, the observed hadron-lepton asymmetry can be explained very naturally. However it has to be noticed that antiparticles data from PAMELA taken alone are not enough to distinguish between the astrophysical and exotic hypoteses, but an additional measurement may help to solve the issue: the signal from nearby pulsars is expected to generate a small but significant dipole asymmetry in the CR electron spectrum, potentially providing a method by which the Fermi gamma-ray space telescope would be capable of confirming a pulsar origin of the observed high-energy positrons (Hooper *et al.*, 2009; Büsching *et al.*, 2008).

It is worthwhile to cite that some papers report an explanation of the excess in terms of a more standard galactic CR origin scenarios. Blasi (2009) suggests that the high energy e^+ could be secondaries produced in hadronic interactions that take place inside the sources, in the same region where cosmic rays are being accelerated; another explanation is provided by Shaviv *et al.* (2009) in terms of inhomogeneity of CR sources on a scale of the order of 1 Kpc.

Chapter 3

Particle identification

This chapter describes the selection criteria that have been developed for each PAMELA detector for the selection of electrons and positrons in the energy range from 0.2 to 3.0 GeV, from the data collected with the PAMELA experiment between June 7th 2006 and December 31st 2008. An estimation of the contamination from wrongly selected positrons in also described.

3.1 Introduction

The main feature of the PAMELA experiment is its ability to discriminate among particles and antiparticles, exploiting the presence of the magnetic spectrometer. Identical particles with opposite charge, like electrons and positrons, can thus be identified.

Electrons and positrons are not the dominant components of cosmic rays: they amount to the 2% of the cosmic radiation, protons constituting the majority of CR. Among the negatively charged CR particles electrons are the most abundant, while antiprotons are only a small fraction ($\sim 10^{-3}$ at 1 GeV, increasing to $\sim 10^{-2}$ at higher energies) of the negative particles. Thus, it is rather straight-forward to select electrons with a small contamination of other kind of particles, while it is more challenging selecting positrons from the huge background of protons: the proton to positron ratio is $\sim 10^{3}$ at 1 GV and increases to $\sim 10^{4}$ at 100 GV. Moreover secondary particles, like pions, generated from the interaction of primaries in the instrument, constitute an additional source of background.

Figure 3.1 (top panel) shows the particle abundance in the cosmic radiation as a function of velocity and rigidity in the energy range of interest for this thesis. The bands in the plot can be associated to different species, since the mass of a particle is uniquely defined by the rigidity and velocity ($p = mv\gamma$). Only downward-going particles are represented in the figure, so negatively charged particles are in the negative rigidity part of the plot. This sector is dominated by electrons, with a small contribution from negative pions and
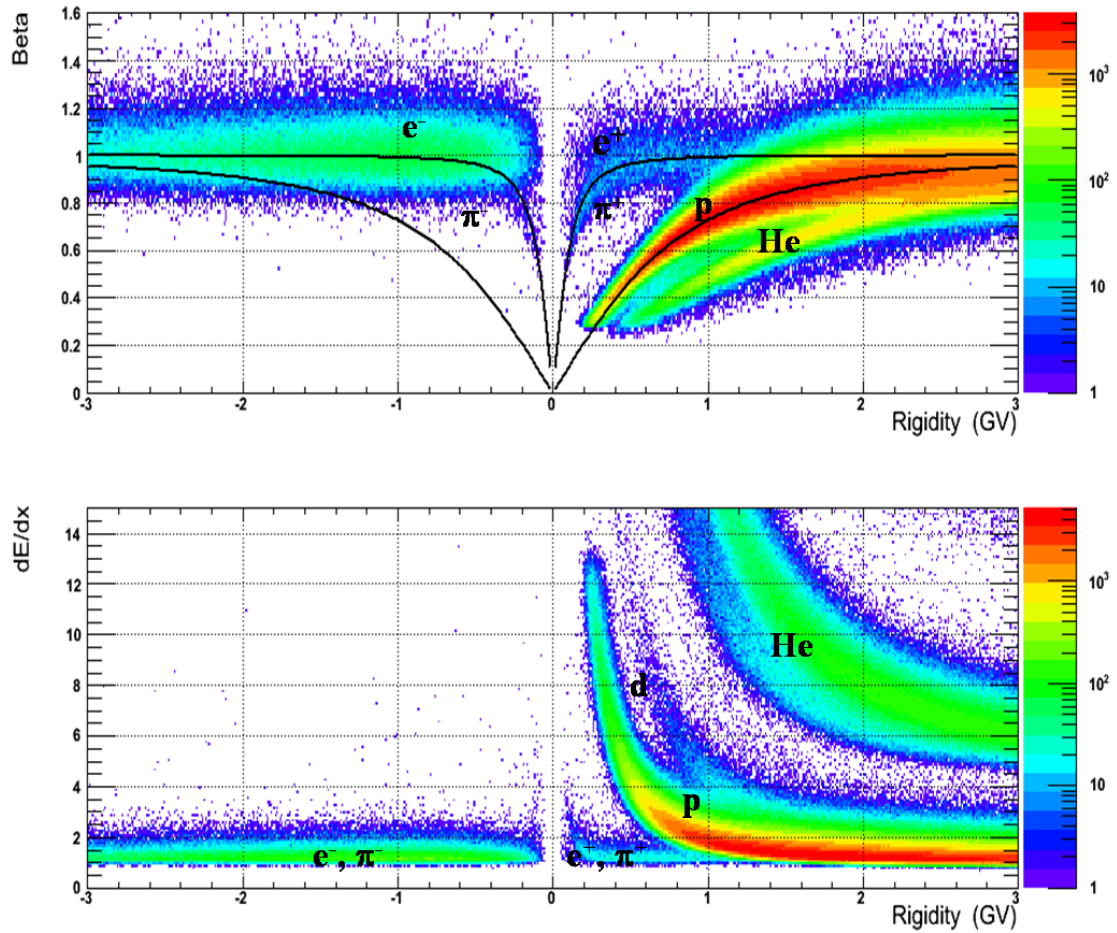
Figure (3.1)   *Top: The β-rigidity distribution of galactic cosmic ray charged particles detected by the PAMELA instrument. On the negative rigidity side the electron band is visible, with some contamination by π^- and a negligible $\bar{p}$ component. On the positive side the positron component is suppressed respect to protons and π^+. Helium and deuterium bands are also visible. The black lines represent the expected theoretical dependence. Bottom: dE/dx-rigidity distribution for the same particle sample.*

antiprotons. On the positive side the positron, proton, deuterium and helium bands are distinguishable. The same populations are illustrated in the bottom panel of Fig. 3.1 as a function of ionization energy loss and rigidity.

The figure clearly illustrates how the positron signal is overwhelmed by the background from positive pions and protons when the mass differences between the different species are not relevant any more respect to their kinetic energy and the respective bands begin to overlap. Massive particles become relativistic at low energy while light particles (electrons, positrons and pions) are relativistic in the whole energy range, moreover non relativistic particles release more than the minimum ionizing particles. Thus, at low energy a first discrimination between massive and light particles can be performed thanks to velocity and ionization measurements, but the situation is complicated by the presence of positive pions. Above ~ 1 GV a big proton contamination can persist and a high proton rejection is thus needed.

An electron and positron sample as clean as possible and a contamination well under control can be achieved by using all the PAMELA subdetectors. The tracker selects clean tracks inside the instrument acceptance measuring their deflection and performs a first e^+ and e^- identification, that the calorimeter will then complete; secondary particles can be identified and rejected from the final electron and positron sample mainly by the use of ToF and AC systems.

The selection steps are summarized as follows:

- Single particle selection.
  This selection allows to reject a large amount of secondary particles, such as pions, that are often accompanied by other interaction products. Compatibility checks among the PAMELA detectors, such as tracker, ToF, calorimeter, are done in order to reject events presenting more than one particle in the instrument acceptance that could compromise the correct identification of a primary particle.

- Track quality selection.
  Conditions on the track reconstruction are applied in order to provide an accurate measure of the particle deflection in the instrument magnetic field and, together with the ToF information, a correct charge sign identification.

- Ionization energy loss measurements on tracker and ToF planes.
  Electrons and positrons are minimum ionizing particles in all the selected energy range. dE/dx measurements, both from tracker and from ToF, are used to separate them from massive particles at low rigidity (see Fig. 3.1).

- Velocity selection.
  The β (velocity in units of c) measured with the ToF system are used to perform

the identification of relativistic, downward-going charged particles, providing an additional criterium for distinguishing electrons and positrons from the background.

- Calorimeter selection.
  Previous selections aim to minimize the contamination of the electron and positron sample, but the real particle identificator is the calorimeter. It provides the necessary rejection power against protons above ~ 1 GV, where dE/dx and β rejection is poor, and against pions in the whole energy range.

- Galactic particle selection.
  Splash albedo particles can be easily rejected from the electron and positron sample thanks to a β measurement; instead, the rejection of reentrant albedos is less straight-forward and requires information about the particle rigidity and the satellite position along its orbit.

In the following sections the selection criteria will be described more in detail, each section dealing with one PAMELA sub-detector.

3.2   Tracker selections

The tracker system is one of the main subjects of the analysis, used to measure the particle curvature inside the PAMELA magnetic field and its energy deposit on the silicon detectors, thus performing the following tasks:

1) It determines the particle sign of charge

2) It accurately measures the particle rigidity

3) It identifies minimum ionizing particles

As mentioned in section 2.2.2, two factors contribute to worsen the tracker resolution: the spillover effect and the multiple scattering. At low energy the track curvature is large,which makes the work of the tracker system significantly easier. Fig. 3.2 shows that the dominant effect affecting the resolution in the energy range of interest is the multiple scattering, that is especially important for light particles which can deviate significantly along their path. Moreover other small track miss measurement that could negatively affect the track recontruction, letting the tracking algorithm associate the wrong trajectory to the incoming particle, can be due to noise on the tracker planes or multiple energy deposits from secondary hits. In order to overcome reconstruction problems that could be due to these effects, a series of quality requirements is applied to the selected track, based for example on the number of points used for the fit or the difference between
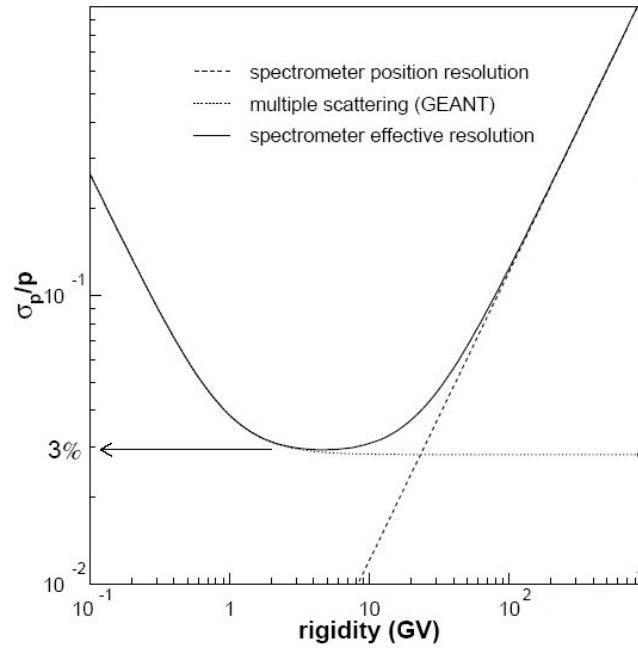
Figure (3.2) *Simulated relative error on the rigidity measure for protons.*

the reconstructed and the measured coordinates of the track. Afterwards, the small miss measurements cannot change the reconstructed sign of charge and the tracker system is able to provide a reliable rigidity reconstruction. Moreover, while in the antiproton analysis even a small fraction of particles with a wrongly reconstructed sign of charge would result in a large background in the antiparticle sample because, of the very small $\bar{p}/p$ ($\sim 10^{-4} - 10^{-5}$), on the positron side the expected e^+/e^- is of the order of $\sim 10^{-1}$, so that this issue is less critical.

The third task of the tracker can be achieved by measuring the energy release on the silicon layers. It provides a criterion to separate electrons and positrons from more massive particles up to ~ 0.8 GV.

The set of selections used for the analysis can be divided in *basic* and *additional tracker cuts*. The former have been developed in order to guarantee the selection of good quality tracks with a reliable rigidity measurement, the latter add an extra rejection for noisy and scattering events and provide a first discrimination of $e^\pm$ from hadrons.

Basic criteria   The basic selections for the reconstructed track are:

1) A single track

2) Number of points in x view ≥ 4

3) Number of points in y view ≥ 3

4) Less than 100 steps for the convergence

5) $\chi^2 > 0$ and $(\chi^2)^{0.25} \leq 2.5 + 1.85 \cdot deflection$

Events having more than one reconstructed track are excluded from the sample of analyzed data. They represent, however, about 5% of the events with track, with the actual data reduction[1].

The second and third selections put a lower limit to the number of points used by the reconstruction algorithm. This number is higher on the x view than on the y view because the rigidity reconstruction is performed on the bending view (x). Selections 4) and 5) deal with the behavior of the fitting algorithm: for each event a χ^2 is calculated on the basis of the difference between the measured impact point on each tracker plane and the reconstructed one. The condition $\chi^2 > 0$ ensures the algorithm convergence, while the fourth selection requires the convergence to be rapid enough. Then, because of multiple scattering, the χ^2 depends on the particle deflection and its distribution assumes higher values at low energy; the upper limit of the χ^2 has a selection efficiency of 98%, constant in the energy range of interest, as determined by flight electron data.

Additional criteria   A set of additional selections have been developed in order to obtain a clean positron sample:

1) A particle track fully contained in the fiducial PAMELA acceptance

2) Consistency between the ToF hit paddles and the tracker reconstructed track

3) A consistent charge release (dE/dx) in the tracker and ToF planes

4) dE/dx < 1.8 MIP[2]

The first cut defines the geometrical acceptance of the instrument, that depends on the magnetic cavity and the ToF plane dimensions. In order to select a clean sample of particles, the considered acceptance is a bit smaller than the nominal one: only particles whose reconstructed track passes through the scintillator and through the tracker planes excluding a border 15 mm large are considered in this analysis.
Moreover an additional test has been performed in order to exclude miss measurements due to energy deposits potentially wrongly associated to the track: the track has been reconstructed several times, recursively excluding each plane from the selection, so that the stability of the rigidity reconstruction has been controlled.
The second condition requires a hit in the ToF paddles in (S11 OR S12) and (S21 OR

---

[1] 8th data reduction.
[2] 1 MIP equals the energy released by a minimum ionizing particle when traversing perpendicularly through the detector.

S22) along the track providing consistency between the tracker reconstruction and the ToF information.

The third selection helps in rejecting events which present a significant amount of energy released on the tracker planes. The cut 3.1 allows to reject interacting events, as demonstrated by a visual inspection performed on a significative sample of events by the use of the PAMELA event-viewer[3]:

$$\frac{dE/dx_{max} - dE/dx_{mean}}{dE/dx_{mean}} < 10 \qquad (3.1)$$

where dE/dx_{max} represents the maximum energy deposit in one of the 12 tracker planes and dE/dx_{mean} the mean energy deposit.

The last condition selects minimum ionizing particles. The cut is able to reject protons below ~ 0.8 GV, where they are not yet relativistic and release more energy than positrons.

3.3 ToF selections

The Time of Flight system contributes to the selection of electrons and positrons from the background of primary and secondary hadrons by measuring the incident particle velocity. The β information, if combined with the tracker rigidity measure, allows to distinguish between positrons and protons below ~ 1 GV. Moreover, thanks to its segmentation, the ToF system provides additional means to reject secondary multi-particles events.

The ToF selections that have been used in the analysis are:

- Multi-particle event rejection

- Relativistic and minimum ionizing particle selection (first lepton selection)

3.3.1 Multiple particle event rejection

Secondaries produced by the interaction of primaries within the instrument or its container which enter the PAMELA acceptance have high probability to be accompanied by other low energy secondary particles, which may hit the anticounter system (see Sec. 2.2.4) and the ToF layers in several points. In order to reject this kind of events an upper limit is put on the number of the ToF hit paddles: not more than one hit on each of the four S1 and S2 planes is required. For a paddle to be hit it is necessary to have a signal from both the

---

[3]The PAMELA event-viewer is a ROOT software package which allows the user to visualize the particle trajectory and interactions in the PAMELA subdetectors. See Fig. 3.13,3.12,3.14 (right panels) for an example.

PMTs associated to the paddle. A maximum number of 3 PMTs hit is allowed outside the track on S11 and S12. No conditions have been applied to S3 as particles interacting below the tracker system should be part of the particle sample.

This selection is not able to identify secondaries in case the particles traverse the same paddle, which can be rejected by a cut on the ToF system dE/dx.

3.3.2   Lepton selection

Electrons and positrons are relativistic minimum ionizing particles also at low energies, so that a cut on the energy released on the ToF paddles and on the particle velocity can help in the discrimination, especially at low energies.

The selection of relativistic, minimum ionizing particles on the ToF system requires:

1) $\beta \geq 0.9$

2) $dE/dx_{S1}^{mean} < 2.0\ MIP$

2) $dE/dx_{S2}^{mean} < 2.0\ MIP$

where dE/dx_{Si}^{mean}, $i = 1, 2$ is the energy release on the i-th ToF plane averaged over the number of layers that compose it and that have signal.

The velocity measure can be obtained by the PAMELA instrument by 12 different combination of the ToF layers. The 12 β measurements are combined to give the mean β to be used and an optimized algorithm allows to define its quality. In this analysis the highest quality β is used, since it makes the particle bands more defined and narrow, which helps in the discrimination and background reduction. Fig. 3.3 is obtained from flight data and shows the fraction of particles with defined and relativistic standard β that are relativistic also according to the higher quality β. The high quality β rejects, as non relativistic, more positive than negative particles; this is not due to some strange charge asymmetry, but because of the higher level of non relativistic particles that contaminate the positive sample.

3.4   AC selections

As already mentioned in Sec. 2.2.4, the aim of the anticoincidence shielding is to reject secondary particles in an off-line analysis. Due to their position the three AC subsystems are sensitive to different kinds of secondaries. CAS is mounted directly above the calorimeter and surrounds the large amount of material of the magnet, it is therefore more sensitive to secondary particles produced in interactions in the tracker or magnet, or backscattered by the calorimeter. On the other hand CAT and CARD are more exposed to
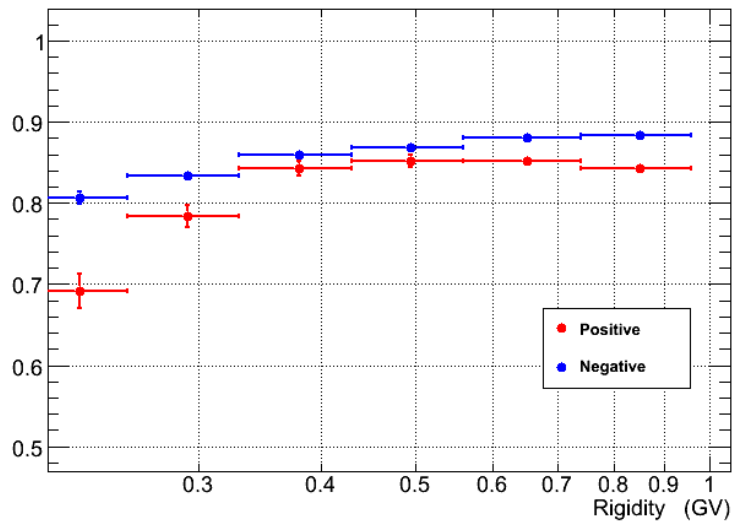
Figure (3.3) *Fraction of flight data positive and negative particles that are relativistic according both to the the standard and to the high quality β.*
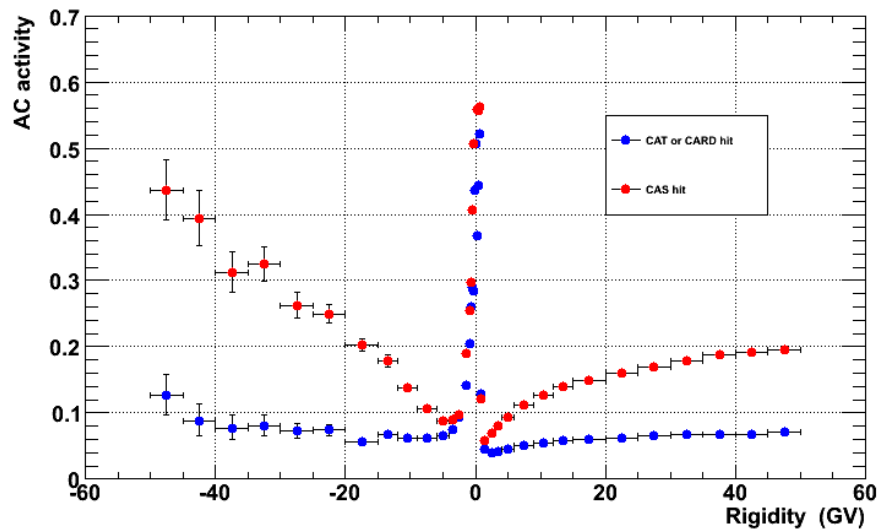

Figure (3.4) *The activity in the anticoincidence system for particles from flight, that fulfill the basic tracker requirements.*

showers of particles coming from the top of the instrument, while they are less affected by back-scattered particles in the calorimeter.

Figure 3.4 shows the fraction of galactic particles, from flight data, passing basic tracker selections described in the previous sections that provoke an activity in (CARD or CAT) - blue dots - and in CAS - red dots. A large spike in the anticounter activity is visible for both positive and negative events at low energy: they have reference to secondary particles produced when primaries hit the satellite payload or interact with the top part of the instrument and create showers of particles, where at least one goes through the PAMELA acceptance while others traverse an anticounter detector. It turns that, expecially at low energy, the AC role is prominent to achieve a clean sample of primary electrons and positrons.

The activity in CAS is generally higher than in (CAT or CARD) which is mostly due to the large number of backscattered particles from the calorimeter. The activity in the anticounters is larger for negatively charged particles such as electrons (the most abundant negatively charged particle) which interact in the first layers of the calorimeter, while protons (the most abundant positively charged particle) interact at an almost random position in the calorimeter, or not at all.

The selection that has been used in this analysis employs CAT and CARD in the whole energy range with the inclusion of CAS only at very low rigidities ρ; below few hundreds GV, the backscattering is not the dominant effect that implicates activity in CAS, as confirmed by a visual inspection of the rejected events. The AC selections used in this work can be summarized as follows:

- CAT and CARD not hit ($\rho \geq 0.4 \ GV$)

- CAT, CARD and CAS not hit ($\rho < 0.4 \ GV$)

3.5   Galactic particle selection

The Earth magnetic field acts as a shield for low energy particles, deflecting and preventing them to be detected by the PAMELA instrument, depending on their energy and instrument latitude. The magnetic field is usually parametrized in terms of a multipole expansion, whose dominant term is the dipolar one: as a first approximation, the Earth magnetic field can be considered a dipole with an inclination of $11.3°$ respect to the Earth rotational axis. A cutoff rigidity can be associated to each PAMELA orbital position, that can be considered as the minimal rigidity for a galactic charged particle to be detected by the instrument. The geomagnetic cutoff is higher at the poles and diminishes at the poles, due to the inclination of the magnetic field dipole. An analytical solution of the equations

of motion in such a magnetic field has been found by Stormer, who expressed the cutoff rigidity as

$$R = \frac{59.6 \; cos^4\lambda}{r^2[1 + (1 - cos^3\lambda \; cos\epsilon \; sin\zeta)^{1/2}]^2},$$ (3.2)

the so called Stormer cutoff; this is the minimum rigidity for a particle coming from a latitude λ from the magnetic equator to reach a distance r from the center of the dipole; the incoming direction of the particle is defined by the zenith and azimuth angles, ζ and ϵ. Eq. 3.2 simplifies in case of a vertically incident particle, becoming:

$$R_{SVL} = \frac{14.9cos^4\lambda}{r^2}.$$ (3.3)

By comparing the particle rigidity and its measurement position it is possible to discriminate among galactic and trapped[4] particles, thus rejecting reentrant albedo events. Reentrant albedo $e^{\pm}$ are particles which escape the atmosphere with rigidity less than the local geomagnetic threshold rigidity and move to the same geomagnetic latitude on the opposite hemisphere entering the atmosphere with a rigidity below the geomagnetic cutoff. While splash albedos are upward-going particles that can be easily rejected by a $\beta < 0$ cut, reentrant albedos enter the instrument acceptance from the top. They could constitute a not negligible background to the galactic e^+ signal since the measured sub-cutoff positron spectrum indicates that sub-cutoff e^+ are about one order of magnitude more abundant than galactic ones (Adriani and et. al., 2009).
The selection that is used to separate galactic from trapped particles is of the form:

$$rigidity > k \cdot R_{SVL}$$ (3.4)

that requires the particle measured rigidity to be a factor k higher than the Stormer vertical cut-off (R_{SVL}). k is a constant to be determined as the minimum values that makes the selection 3.4 efficient in rejecting all trapped particles. A conservative value of $k = 1.3$ has been chosen for this work. This factor was tuned by experimental data to ensure an unambiguous reconstruction of galactic particles: the proton flux measured at the magnetic poles, where the cut-off rigidity value allows to consider all the detected particles to be galactic ($R_{SVL} \sim$ tens MV), is compared with the flux obtained by rejecting sub-cutoff particles by the use of the Eq. 3.4, and found to be compatible (De Simone).

---

[4]Charged particles, decelerating cosmic rays or secondaries produced in interactions with the atmosphere, can be trapped in the magnetosphere and remain there. The charged particle experience a motion along and across the magnetic field lines, bouncing between the magnetic mirror points. They generate the so-called Van Allen belts, high electron and proton intesity toroidal regions that come closer to the Earth where the magnetic field allows it: at the poles and in the so called South Atlantic Anomaly.

3.5.1 Back-tracing in the Earth magnetic field

An additional check has been performed on a significative sample of e^+ data looking for an independent confirm that the selected particles are galactic. A software developed at the Bartol Institute (University of Delaware) has been used to back-trace low energy particles in the Earth magnetosphere, in order to reveal their galactic or trapped origin (Bartol group website).

The software, whose original objective was the determination of the geomagnetic rigidity cut-off for a given location, exploits a fundamental concept of the electromagnetic theory which allows to solve the original problem with no need to illuminate the full magnetopause surface with particles: ignoring drift effects, charged particle dynamics in electromagnetism has an absolute symmetry when simultaneously reversing time and charge sign. If a particle, shot away from Earth at a certain rigidity and angles, crosses magnetopause and enters the interplanetary medium, a particle with the same rigidity, but opposite charge and reversed directional cosines on any point on the trajectory should follow the same path, but in the backwards direction. The input parameters of the code are the following:

- Geographic latitude and longitude where the particle will leave the atmosphere of the Earth

- Kp index, which is a measure of the geomagnetic disturbance level

- Height where the particle will leave the atmosphere of the Earth

- Date and time that the particle will leave the atmosphere of the Earth

- Initial zenith angle, ζ, in degrees

- Initial azimuth angle, η, in 1/10 degrees

The Kp index has been chosen to be the lowest due to the low level of solar activity. The other information can be extracted from the PAMELA data on an event basis. The knowledge of the zenith and azimuth angles requires a coordinate transformation from the instrument reference system to the one defined as follows: let vertical be the z-axis of a polar coordinate system, then the local South is along the x-axis and local East along the y-axis. ζ is simply the polar angle of the reverse incident direction, and η is the azimuth angle of the reverse incident direction, i.e. measured counter-clockwise from South.

The software provides in output the final x, y and z coordinates, measured in Earth radii, of the final point of the trajectory in the GEO reference system[5], as well as a flag which

---

[5]The Geographic Coordinate system (GEO) is defined so that its x-axis is in the Earth's equatorial plane but is fixed with the rotation of the Earth so that it passes through the Greenwich meridian. Its z-axis is parallel to the rotation axis of the Earth, and its y-axis completes a right-handed orthogonal set.
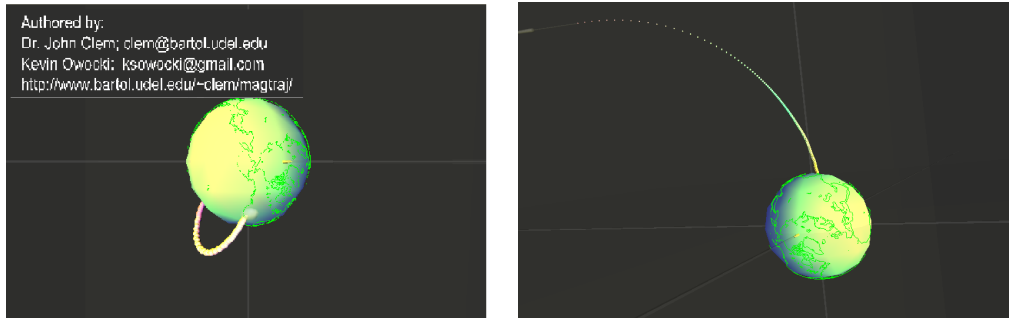
Figure (3.5) *Left: result of the back-tracing algorithm for a low energy positron selected by the PAMELA software as trapped. Right: the same for a galactic positron.*

classificates particles on the basis of their destination. Moreover a VRML representation of particle trajectory, beginning at a specific place on the Earth's surface, navigating through the Earth's magnetosphere is given. Fig. 3.5 shows, as an example, the results obtained for a trapped and a galactic positron according to PAMELA selection and back-traced by the software.

With different types of approaches no contradiction has been found in between what we consider galactic and sub-cutoff particles.

3.6 Calorimeter selections

The PAMELA calorimeter is the real particle identificator of the instrument; in this analysis it is used to identify pions in the whole energy range and higher mass hadrons at energies for which their β and dE/dx distributions do not show significant differences any more respect to the positrons. In Fig. 3.6 the β-rigidity distribution for negatively and positively charged galactic particles is shown at the various stages of the selection chain: in the top panel particles that fulfill the tracker selections are shown, in the middle one those with the additional requirement of no hit in the anticoincidence system and a clean pattern in the ToF system, in the bottom one minimum ionizing particles according to the dE/dx selections on the tracker and ToF system planes. The black dashed line indicates the β selection ($\beta > 0.9$) that adds rejection power to the previous selections.

The separation between positrons and protons worsens with energy and the distributions start to overlap at about 1 GV. At this stage the calorimeter becomes important to remove the remaining protons. Its use exploits the different topology and energy release of the showers that hadrons and leptons origin, being effective also against the residual pion contamination in the whole energy range.

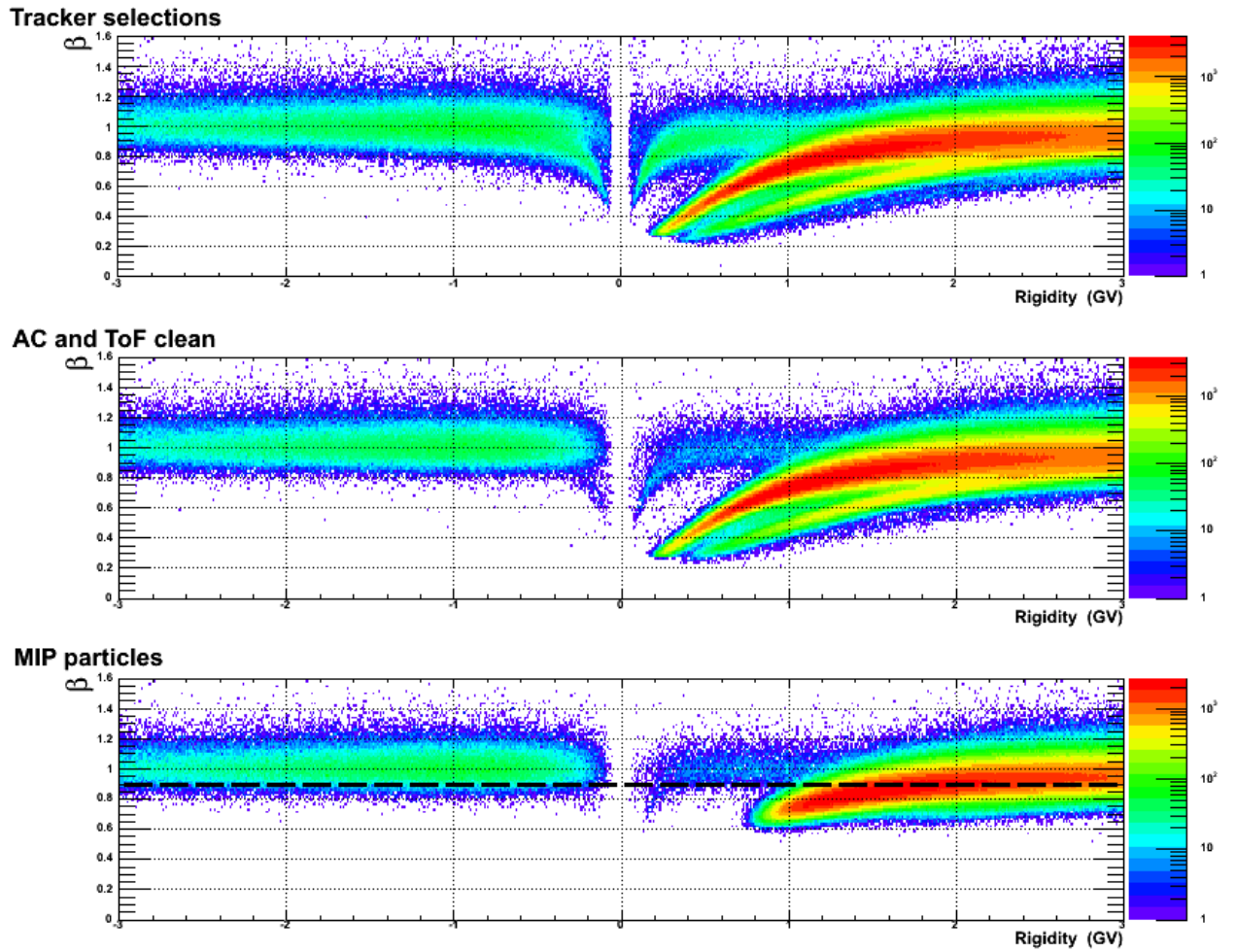The lepton identification power of the cuts that have been described up to now can be

Tracker selections

AC and ToF clean

MIP particles

Figure (3.6) *β-rigidity distribution for particles selected by the tracker (top panel), by the further selections on AC and ToF (except β cut) (middle panel) and by additional dE/dx criteria.*
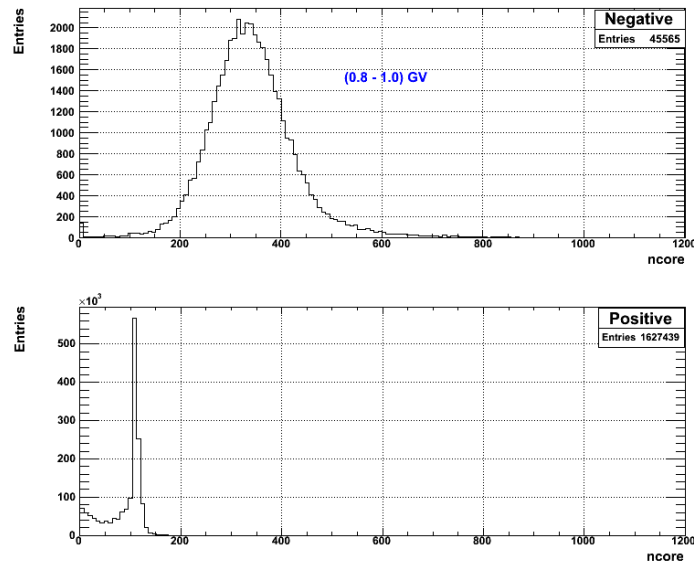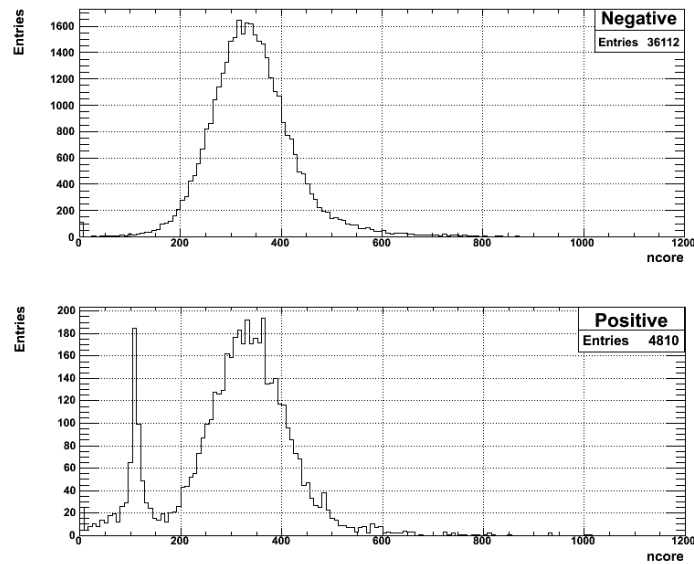
Figure (3.7)   *Distribution of positive (top panel) and negative (bottom panel) tracked events in the rigidity range (0.8-1.0) GV as a function of a calorimetric variable connected to the topologic development of the shower in the calorimeter.*

Figure (3.8)   *Distribution of positive (top panel) and negative (bottom panel) events in the rigidity range (0.8-1.0) GV as a function of a calorimetric variable connected to the topologic development of the shower in the calorimeter. The events have been selected with tracker, ToF and AC as leptons.*

visualized by plotting the distributions of the positive and negative events as a function of a calorimetric variable that will be described in 3.6.2. Following the analysis steps, the e^+ signature arises, as illustrated in Fig. 3.7 and 3.8 for the rigidity range from $0.8 - 1.0$ GV. Fig. 3.7 presents the situation after the cuts on the tracker system which have been previously described, both for negative (top panel) and for positive particles (bottom panel). The negatively charged particle distribution is dominated by electrons and has a peak below 400, while on the positive side it is not possible to distinguish the corresponding positron peak, overwelmed by hadron background. Fig. 3.8 shows the same distributions as obtained after the application of 'all' previously described cuts. The positron signal is now visible, and well separate from the hadron counterpart, so that it is possible to reject the non negligible residual contamination with a selection on this calorimetric variable. However, the effectiveness of this selection at lower and higher rigidities is not as high as in this range; this is the reason why further calorimetric variables have been studied to reduce the hadron component to a negligible value.

In the following a brief overview of the calorimeter response to particle interactions and the description of the developed selections used in this analysis will be given.

3.6.1 Particle interactions in the calorimeter

The passage of charged particles through matter is characterized by a loss of energy by the particle and a deflection of the particle from its incident direction. The major part of the energy loss for heavy particles is due to inelastic collisions with the atomic electrons of the material and can be described by the Bethe-Bloch formula:

$$-\frac{dE}{dx}[\frac{MeV}{g\,cm^2}] = K\rho\frac{Z}{A}\frac{z^2}{\beta^2}[ln(\frac{2m_e^2\gamma^2W_{max}}{I^2}) - 2\beta^2 - \delta - 2\frac{C}{Z}] \tag{3.5}$$

where $K = 2\pi N_a r_e^2 m_e c^2 = 0.1535 MeV\,cm^2/g$, with r_e the classical electron radius, N_a the Avogadro's number, m_e the electron mass. In equation 3.5 ρ, Z and A are respectively the density, the atomic number and the atomic weight of the absorber material, $I \simeq 16XZ^{0.9}$ is the effective ionization potential, z is the charge and β the velocity of the incident particle, δ is a density effect correction and C the shell correction.

Like heavy charged particles, electrons[6] also suffer a collisional energy loss when passing through matter. However, because of their small mass an additional energy loss mechanism comes into play: the emission of electromagnetic radiation arising from scattering in the electric field of a nucleus (*bremsstrahlung*). The bremsstrahlung cross section varies as the inverse square of the particle mass, $\sigma \propto r_e^2 = (e^2/mc^2)^2$, thus below a few hundred GeV electrons are the only particles in which radiation contributes substantially to the energy loss of the particle. The radiation loss for electrons in copper is illustrated in Fig. 3.9.

---

[6]Unless stated the contrary, electrons are interchangeable with positrons.
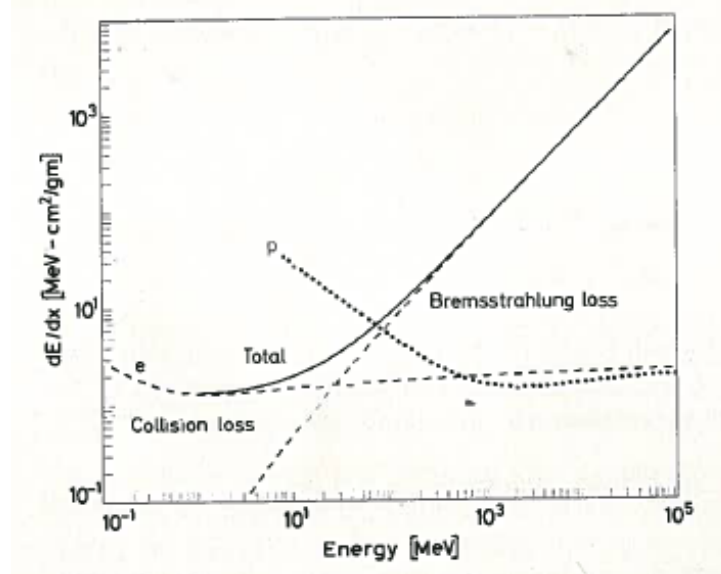
Figure (3.9) *Radiation and collision loss for electrons in copper. For comparison, the dE/dx for protons is also shown.*

For each material it is possible to define a critical energy, E_c, at which the average energy losses from radiation equal those from ionization, that is characteristic of the traversed material. The following expression for the critical energy is recommended by the PDG:

$$E_c = \frac{610 MeV}{Z + 1.24} \tag{3.6}$$

which corresponds to ~ 8 MeV in the PAMELA calorimeter. Another parameter, characteristic of the material, useful to describe electron interactions in matter is known as *radiation length*. It is defined as the distance over which the electron energy is reduced by a factor $1/e$ due to radiation loss only. The radiation energy loss, when expressed in terms of radiation length, is roughly independent of the material type. In a qualitative description it is possible to say that an impinging electron emits a bremsstrahlung photon after approximately one radiation length.

The behavior of photons in matter is different from that of charged particles: their lack of an electric charge makes impossible the many inelastic collisions with atomic electrons characteristic of charged particles. Instead, the main interactions of photons in matter are:

- Photoelectric effect

- Compton scattering

- Pair production

The photoelectric effect involves the absorption of a photon by an atomic electron with the subsequent emission of the electron, the energy threshold being given by the electron atomic binding energy. The Compton scattering is the scattering of photons on free electrons (if the photon energy is high with respect to the binding energy the electrons can be considered free). The process of pair production involves the transformation of a photon into an electron-positron pair and, in order to conserve momentum, it can only occur in the presence of a third body, usually a nucleus. Moreover, to create the pair, the photon must have an energy higher than 1.022 MeV.

While the cross section of the first two processes decreases with increasing energy, the pair production one has the opposite behavior, as shown in Fig. 3.10, which makes it the dominant process at high energy.
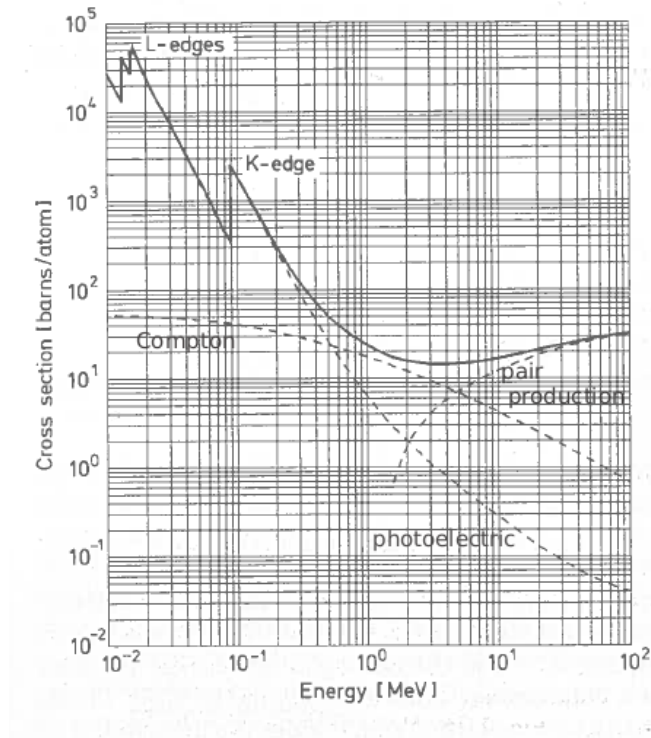
Figure (3.10)   *Total photon absorption cross section for lead.*

3.6.2   Electromagnetic and hadronic showers

One of the most impressive results of the combined effect of pair production by high energy photons and bremsstrahlung emission by electrons is the formation of electromagnetic showers. An electron in matter emits energetic bremsstrahlung photons which in

turns convert into electron-positron pairs. These emit further photons and the result is a cascade of photons, electrons and positrons. This continues until the energy of the pair-produced electrons and positrons drops below the critical energy. At this point, the e^+e^- pairs will preferentially lose their energy via atomic collisions rather than bremsstrahlung emission, thus halting the cascade.

The development of the cascade is a statistical process; however, using the notion of radiation length, it is possible to describe qualitatively the mean number of particles produced and the mean energies as a function of the penetration depth. A simple model[7] assumes that each electron in the shower, when traversing 1 X_0 of material, produces one photon losing half of its energy to the product, and that each photon after 1 X_0 creates in turn an electron and positron pair[8] splitting its energy equally between the two secondaries leptons. In this description, after nX_0 an electron of energy E_0 has produced $N = 2^n$ secondaries, each of energy $E = E_0/2^n$. The maximum of the shower is reached when $E = E_c$, thus at $n = ln(E_0/E_c)/ln2$, with a number of generated particles equal to $N_{max} \simeq E_0/E_c$.

Figure 3.11 shows the longitudinal profile for a 300 GV electron showering in the PAMELA calorimeter. Notice that the shower maximum is well contained event at such a high energy.
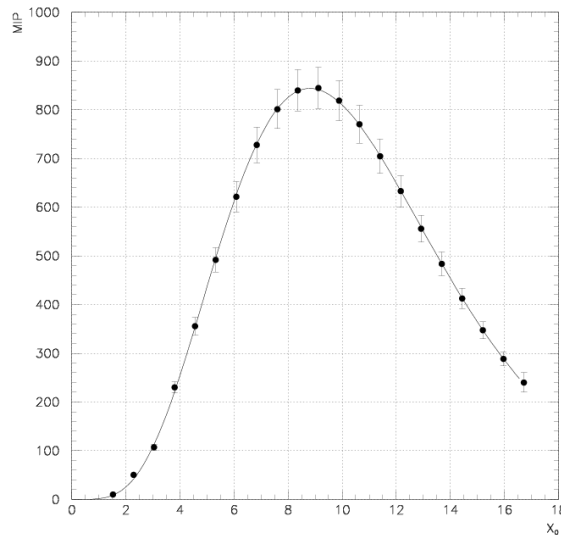

Figure (3.11) *300 GV mean electron longitudinal profile in the PAMELA calorimeter.*

---

[7]A more detailed description of the longitudinal development of the electromagnetic shower and its parametrization has been given by Rossi and Greisen (1941).

[8]The mean free path of a γ ray for pair production is $\lambda_{pair} \simeq \frac{9}{7}X_0$.

As the shower develops, its lateral dimensions also increase due to various effects:

1) The finite opening angle between electron and positron in pair production, as well as their multiple scattering, direct the particles away from the shower longitudinal axis.

2) Photon and electrons produced in isotropic processes (Compton scattering, photoelectric effect) move away from the axis. Also, bremsstrahlung photons emitted by electrons that travel at a considerable angle with respect to the shower axis may contribute to this effect.

The transverse dimensions of electromagnetic showers is mostly conveniently measured in terms of the *Moliere radius*, which is defined as

$$R_M = 21.2 MeV \frac{X_0}{E_c} \tag{3.7}$$

More than 90% of the shower is contained within a distance of about $2R_M$ from the longitudinal axis, almost completely independently of the energy of the incoming particle.
In case of charged hadrons, besides the ionization process, the strong interactions between the particles and the nuclei of the absorbing medium also play an important role: when a charged hadron penetrates a block of matter, it will ionize the atoms of the traversed medium in a continuous stream of events; moreover at some depth, the hadron will encounter an atomic nucleus with which interacts strongly. The particles produced in the first nuclear reaction (mesons, nucleons) may in turn lose their energy by ionization of the medium and/or induce new reactions, thus causing the shower to develop. Conceptually this shower is very similar to the electromagnetic one: the number of shower particles increases as a result of the multiplication process, and so does the energy deposited in a slice of a given thickness. At some depth further multiplication is balanced by the absorption of shower particles (shower maximum) and, beyond this point, the number of shower particles and the deposited energy gradually decrease.
Despite these similarities, there are major differences between electromagnetic and hadronic showers. One concerns the *scale* of the electromagnetic and hadronic shower development that are different to an extent determined by the differences between the cross sections for the electromagnetic and nuclear interactions. The hadronic shower dimension is governed by the nuclear interaction length λ_{int}, defined as the average distance a high-energy hadron has to travel inside that medium before a nuclear reaction occurs. The interaction length is inversely proportional to the total cross section for nuclear interactions, thus it scales with the atomic weight A of the target medium as $A^{1/3}$. The probability that the particle traverses a distance x in this medium without interacting equals

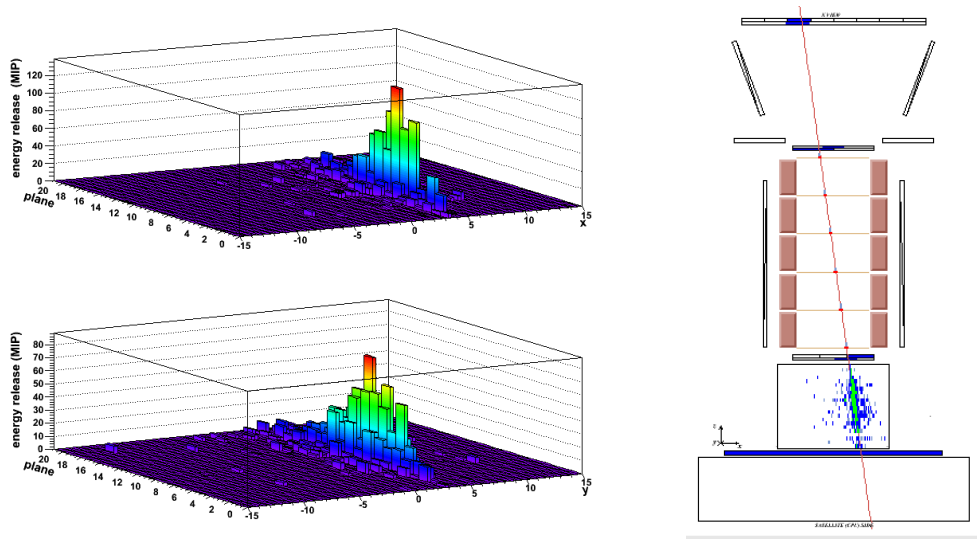$$P(x) = exp(-x/\lambda_{int}) \tag{3.8}$$

Figure (3.12)   *A 19 GV electron from flight data. Left: the calorimeter response to the developed shower (see text). Right: visualization provided by the PAMELA event viewer.*

Hadron showers do not only develop until reaching a much greater depth inside the absorber material, they are also considerably broader than electromagnetic showers. The radial shower profiles, defined as the energy deposited in a radial slice of a certain thickness as a function of the distance between that slice and the shower axis, exhibit in most material a narrow core surrounded by a halo. The narrow core is due to the electromagnetic component of the shower caused by π^0 produced in the shower development. The halo depends on the non-electromagnetic shower component: in hadronic interactions about 50% of the energy is carried away by secondary particles which have large transverse momentum (Wigmans, 2000).

Moreover, while the energy deposit is very regular for electromagnetic showers, large fluctuations can be observed in case of hadronic interactions.

Differences in the energy deposit and shower topology, as detected by the PAMELA calorimeter, are illustrated in left panels of Fig. 3.12, 3.13 and 3.14, which show respectively a 19 GV electron, a 12 GV interacting proton and a 19.5 GV non interacting proton from flight. On the left, the showers generated in the calorimeter are visualized in 3D both on the x (top panel) and y (bottom panel) view. Right panels show the instrument response to the events as visualized by the PAMELA event viewer. In case of a non interacting proton a single track is seen in the calorimeter. Since the PAMELA calorimeter is only $0.6\lambda_{int}$ length (the mean free path in tungsten is 9.6 cm), about 55% of incident protons do not produce a shower in the detector. This case is different from the electron
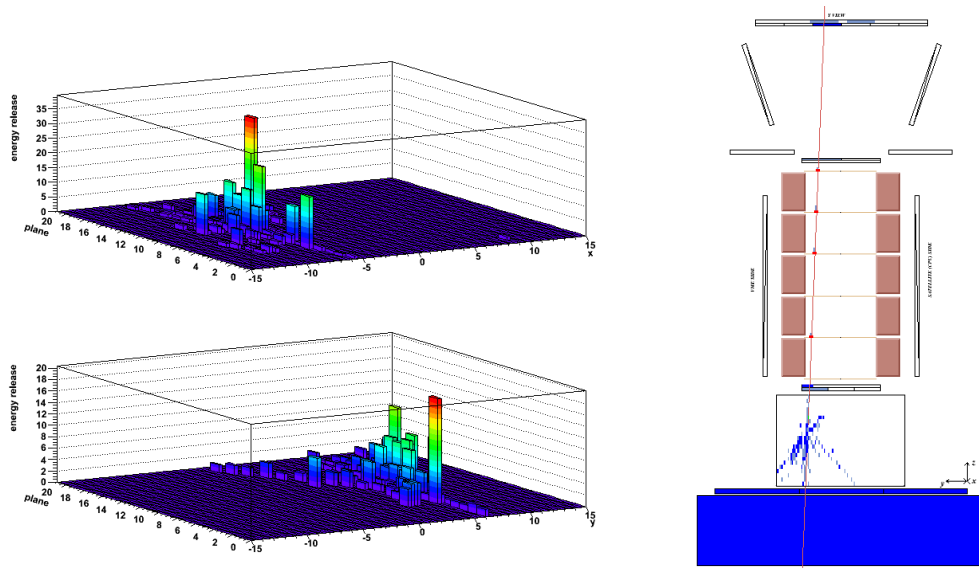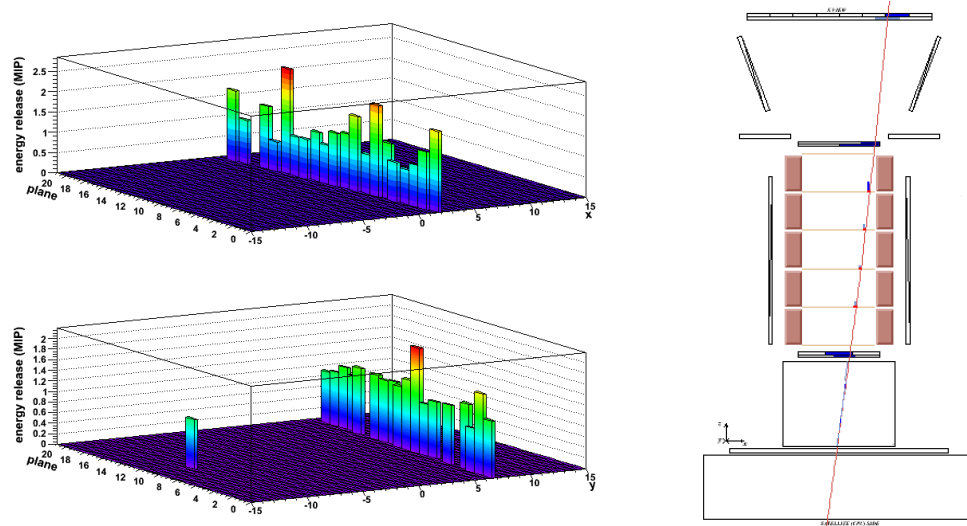
Figure (3.13)   *An interacting 12 GV proton from flight data. Left: the calorimeter response to the developed shower (see text). Right: visualization provided by the PAMELA event viewer.*

Figure (3.14)   *A non interacting 19.5 GV proton from flight data. Left: the calorimeter response along the track (see text). Right: visualization provided by the PAMELA event viewer.*

event shown in Fig. 3.12, which makes non interacting protons a very easily eliminable background from the positron signal. In that figure, the impinging particle interacts in the very first layers of the calorimeter and produces a collimated electromagnetic shower which is fully contained in the calorimeter. On the other side the proton in Fig. 3.13 interacts more deeply in the calorimeter and originates a large shower, where secondaries can be seen as non interacting tracks at large angles from the direction of the incoming particle. The energy release is much more irregular then in the electron case.

These differences can be exploited to remove the residual hadron background from the positron sample. The calorimetric variables used in the analysis can be divided in the following categories:

- longitudinal profile

- lateral profile

- topological development

- starting point.

The selections have been developed by simulation, deriving optimized cuts for the best reduction of the contamination, even if to detriment of the efficiency, which is not a problem in this low energy range where the statistics is abundant enough. Below ~ 1 GV the shower development is not well defined because of multiple scattering, Compton scattering and energy losses, that result in a larger fraction of energy lost in the tungsten and a lower probability to detect and properly parametrize electromagnetic showers as the primary initial energy decreases. Thus, besides some standard variables useful above ~ 1 GV, other new variables optimized for the lower energy range have been developed. Moreover in this rigidity region, due to dependence of cross sections on the energy, the efficiency of the selections results to be more energy dependent than in the higher energy range.

A set of electrons, positrons, protons and pions have been generated isotropically above the PAMELA Al cover; electron and positron events entering the instrument acceptance have been saved. The proton and pion simulation will be described more in detail in Sec. 3.7.2. The software used for the scope is GPAMELA, the official PAMELA Collaboration simulation tool, based on the GEANT package 3.21. It has been opportunely modified in order to save only relevant events and thus computing time.

In order to further clean the sample of selected events, removing secondary interactions or particles not well contained, a fiducial acceptance has been defined in the calorimeter volume, imposing that the strip traversed by the reconstructed track in the first and last plane of both views of the PAMELA calorimeter ranges between strip number 7 and 89 excluded. In the following the developed selections will be illustrated.

Longitudinal profile   As it was explained above, a large fraction of protons is non inter-
acting in the calorimeter and can be easily separed from the positron sample. A variable
that can successfully describe the longitudinal development, highlighting the differences
between leptons and non interacting hadrons, is the number of hit strips in the calorimeter
($nstrip$). The PAMELA calorimeter is constituted by 44 sensitive Si planes, where one
plane is not active. Thus, a hadron which do not produce a shower in the calorimeter
would ideally hit 43 strip. The distribution of the variable *nstrip* is shown in Fig. 3.15 as a
function of rigidity for simulated positrons, positive pions and protons, and in Fig 3.16 for
real data, both positive and negative. Here and in the following, the distributions shown
are constituted by events which have survived the e^+ selections previously described.
Thus, below ~ 0.8 GV, the proton contamination is already considerably reduced.
The distribution of $nstrip$ peaks, for hadrons, around 46 strip, due to inclined tracks
which sometimes hit more than one strip. The behavior of positrons reflects the avalanche
multiplication, being the number of hit strips increasing with rigidity.   The rejection of
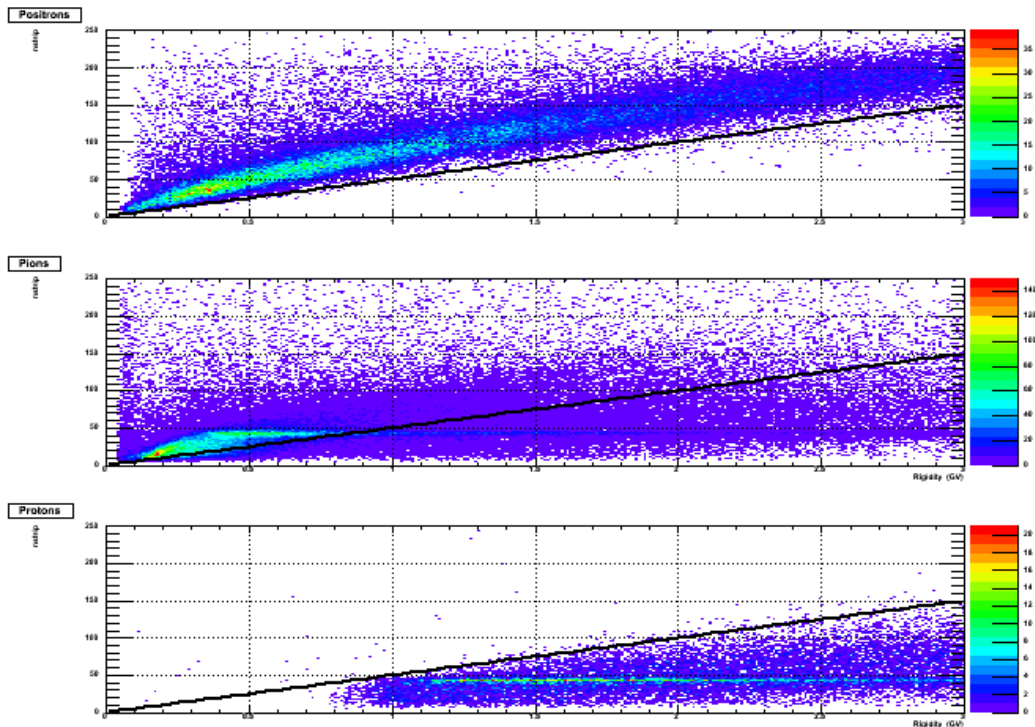

Figure (3.15)   *Distribution of the number of hit strips in the PAMELA calorimeter as
obtained by simulation for positrons (top panel), positive pions (middle
panel) and protons (bottom panel). In black is shown the selection cut*

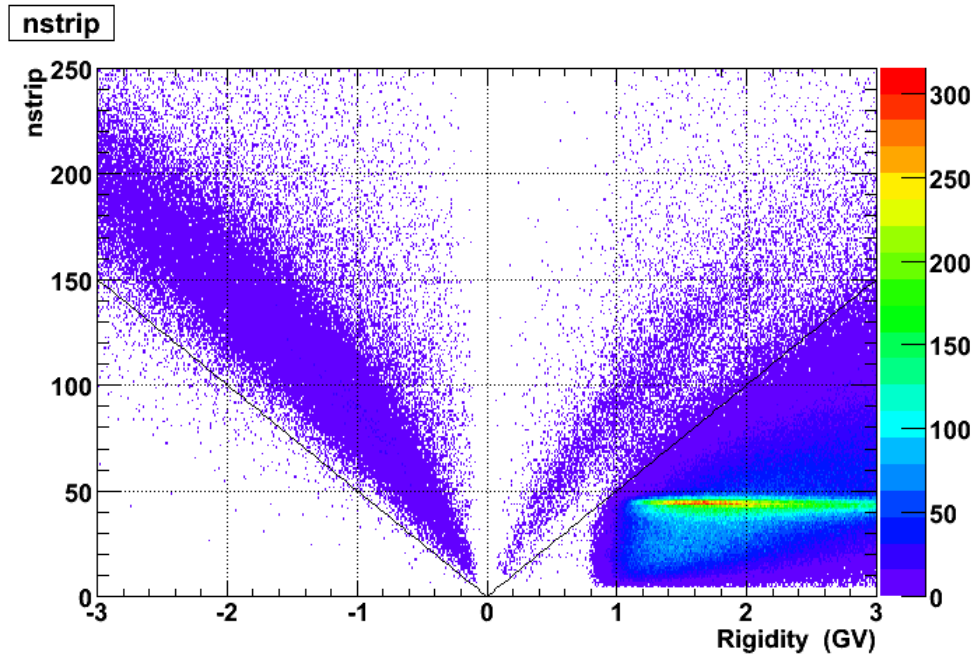some fraction of the not interacting hadrons is obtained thanks to the following cut (black

Figure (3.16) *Distribution of the number of hit strips in the PAMELA calorimeter as obtained by flight data). In black is shown the selection cut*

line in figure), where x stands for rigidity:

$$nstrip > 0.2 + 50 \cdot x \tag{3.9}$$

This simple way to characterize the differences between electromagnetic and hadronic showers allows to eliminate nearly all non interacting particles and hadronic showers with low multiplicity at high energy. Unfortunately a selection based on the number of strip is not effective at rigidities below $\sim 500 MV$, where the electromagnetic showers are so small that the number of hit strip becomes comparable in the leptonic and hadronic interaction case.

In order to extend to lower energies the calorimeter rejection power, the number of planes presenting 0 or only 1 strip hit (npl_0strip, npl_1strip) have been considered. Since low energy electrons and positrons interact immediately and the shower develops and vanishes within few planes, the number of planes with 0 strip hit (see Fig. 3.17) is much higher for positrons than for hadrons, except for the very low energy range where similar values for npl_0strip are generally obtained. Analogously, the number of planes with only 1 hit strip is not high for electrons in the whole rigidity range since the shower develops and stops in the first layers of the detector, while npl_1strip peaks above 40 at rigidities higher than ~ 300 MeV for hadrons. Only events contained between the two black lines in Fig. 3.17

and fulfilling the following requirement on npl_1strip are selected as positrons:

$$3. < npl\_1strip < -3.4 \cdot x + 20.5 \tag{3.10}$$

Additional rejection power can be obtained when considering the different shape of the energy release for positrons and hadrons. The calorimeter has been divided in two independent sectors constituted by its top 7 modules[9] and the remaining 15 ones. The fraction of energy released in the second part of the calorimeter ($qtot\_ratio$) is shown in figure 3.18. For hadrons, large values of this fraction are expected respect to positrons, because they do not interact, interact lately or stop in the calorimeter with a Bragg peak. Indeed, the distribution of $qtot\_ratio$ peaks around 60% for hadrons, and is lower for e^+, providing a criterion for discriminating among them above 300 MV. The splitting of the calorimeter has been tuned to maximize differences among positrons and pions/protons in the rigidity range of interest. Again, only events between the two black lines shown in the plot are not rejected as hadrons.

Additional cuts on some parameters of the longitudinal profile are used, when a fit of the profile can be performed:

1) $t_{max}/lnE_0 < 1.3 - 0.1 \cdot x$

2) $0.04 \cdot x + 0.35 < asym < -0.03 \cdot x + 0.73$

3) $E_0/x > 14 \cdot x + 95$.

The selections exploit the previously illustrated dependence of the shower parameters: the logarithmic dependence of the shower maximum (t_{max}, in radiation lengths) on the particle reconstructed energy E_0, the value of the asymmetry $asym$, defined as the energy released before the maximum to the energy released after the maximum ratio, and the dependence of E_0 on x.

Lateral profile   As previously mentioned, electromagnetic showers deposit about 95% of their energy inside $2R_M$ which, for the PAMELA calorimeter, corresponds to about 1.8 cm or 7.5 strips. On the other hand, in case of hadronic interactions $\sim 95\%$ of the particle originating the shower is released in a cylinder with radius of about one interaction length, which means almost 10 cm for the PAMELA calorimeter. This difference can be exploited to further distinguish between positrons and hadrons by the use of variables built around the trajectory of the incident particle or, when it is possible, the reconstructed longitudinal axis of the shower.

Fig. 3.19 illustrates the measured energy deposited in a cylinder of radius 4 strips around the shower axis. Only particles above the black line shown in figure are not rejected.

---

[9]A module in the PAMELA calorimeter is intended to be composed by two silicon layers and the tungsten plane between them.
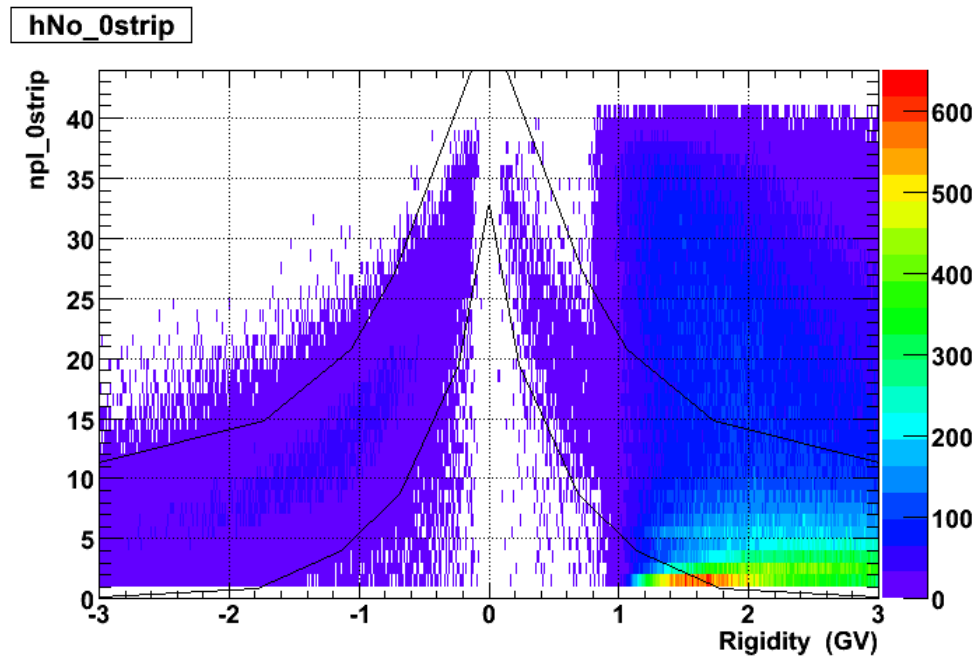
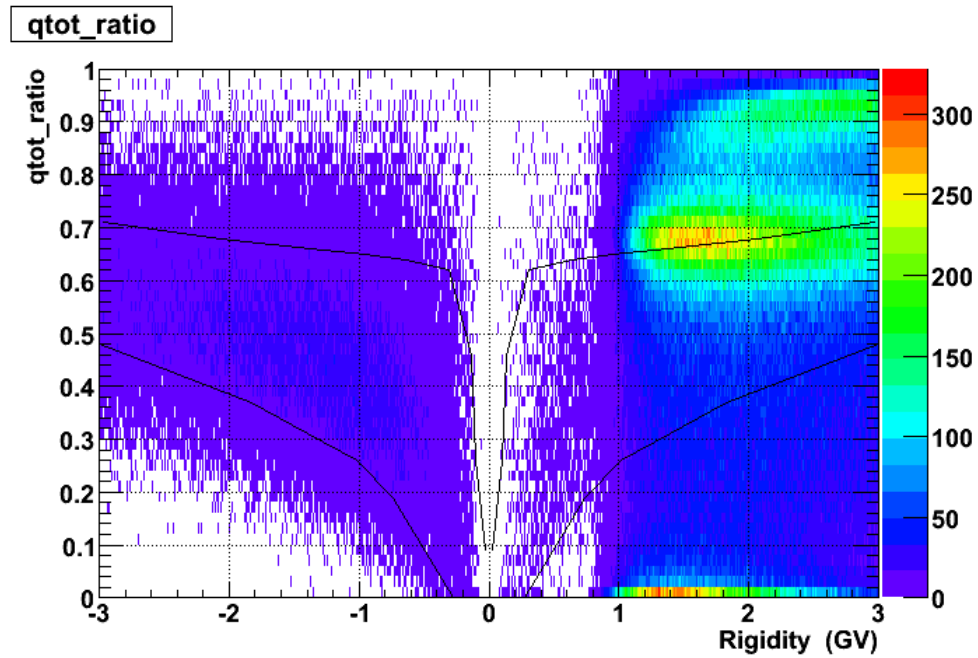**Figure (3.17)** *Number of planes with 0 strips hit for flight data events.*

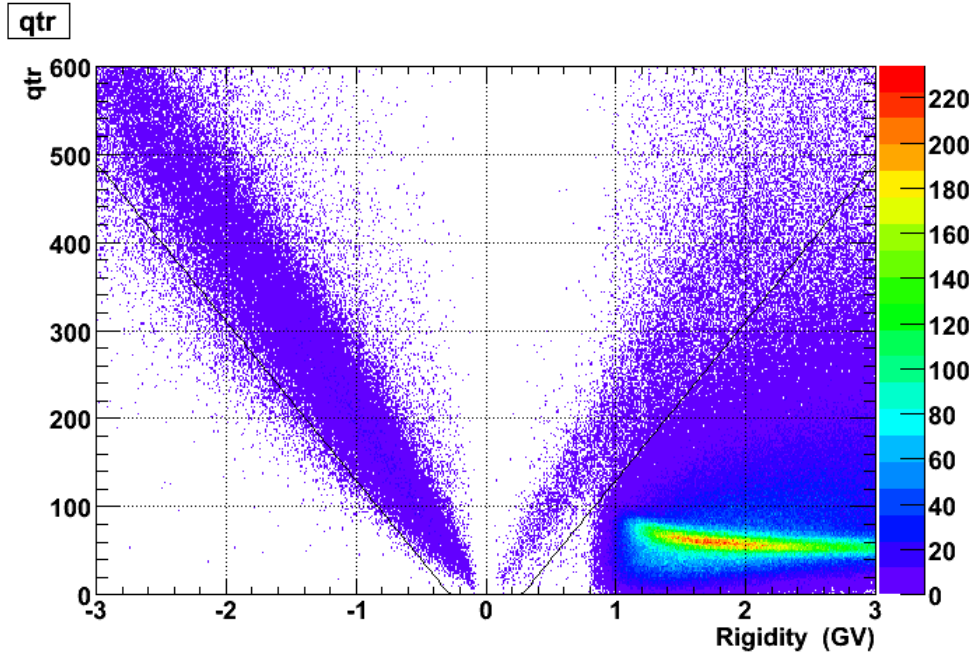**Figure (3.18)** *Fraction of energy released in the last 15 modules of the calorimeter from flight data.*

Figure (3.19)   *Energy released in a cylinder of radius 4 strips around the shower axis.*

Topological development   As mentioned in section 3.6.2, the number of secondaries and the released energy in case of an electromagnetic shower is closely related to the energy of the primary, while no simple relation can be found in the hadronic case. The variable $ncore$, shown in Fig. 3.20, has been developed to separate positrons from hadrons that originate showers with high multiplicity, and thus it is more effective in the higher rigidity range. This quantity is defined as:

$$ncore = \sum_{j=1}^{2} \sum_{i=1}^{PLmax} n_{hit(i,j)} \cdot i$$

where $n_{hit}(i, j)$ is the number of strips hit inside a cilinder of radius $2R_M$ around the track in the i-th plane of the j-th view, where the top plane is number 1 and the sum runs up to plane number $PLmax$, closest to the calculated electromagnetic shower maximum of the j-th view. This quantity strongly emphasizes the multiplication with increasing calorimeter depth and the collimation of the electromagnetic cascade along the track assuming large values, while in the hadronic case the transverse dispersion and the limited number of secondaries usually results in low values of this variable.

Starting point   The probability for a hadron to begin a shower in the first two calorimeter tungsten layers is less than 3%, while it is practically 1 for positrons. A selection based on the shower starting point can discriminate positrons from lately interacting hadrons, but only to an extent determined by the possibility to identificate the shower. Even in this
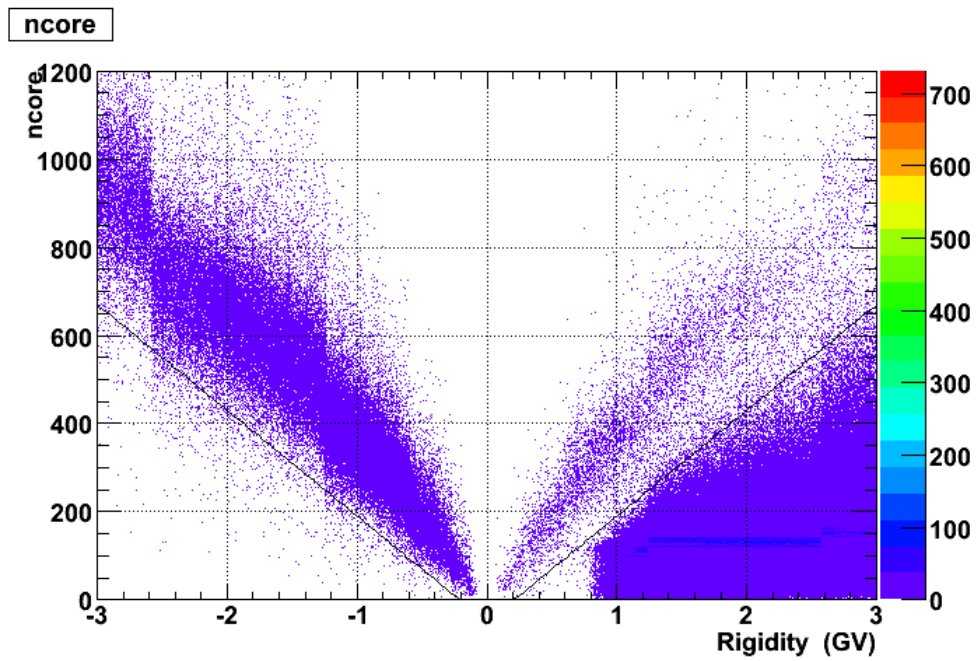
Figure (3.20) *Topological variable that emphasizes differences between hadronic and electromagnetic showers related to their multiplication at increasing depth.*
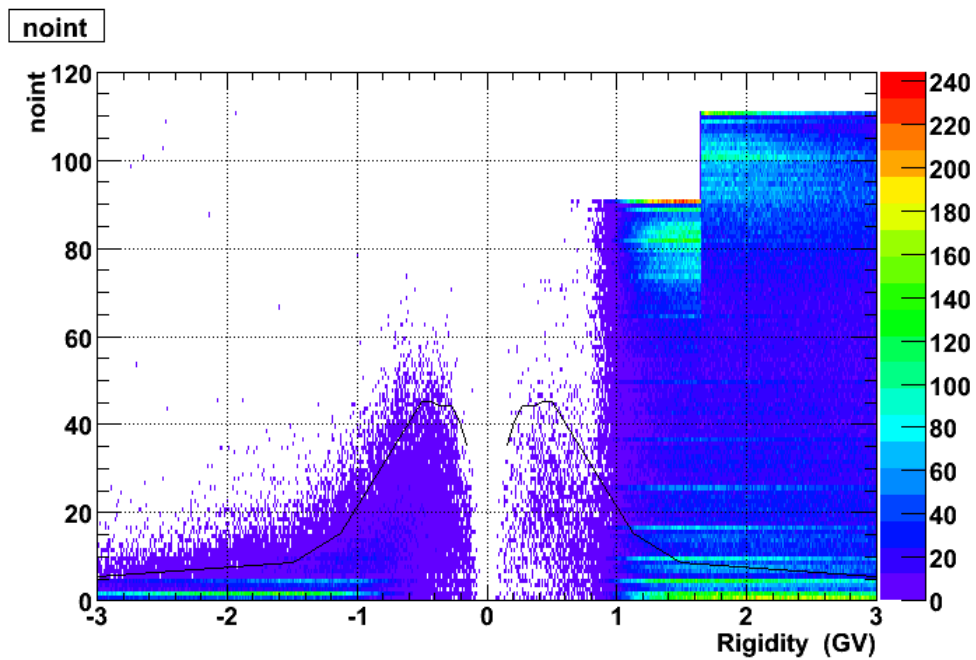

Figure (3.21) *Variable which describes the starting point of the shower. Only particles below the black line are selected as e^+ and e^-.*

case the selection effectiveness gets worse at low rigidities. The corresponding variable, $noint$, is defined as follows:

$$noint = \sum_{j=1}^{2} \sum_{i=1}^{22} TH(i,j) \cdot i$$

where $TH(i,j) = 1$ if the i-th plane of the j-th view has a cluster along (less than 4 mm away) the track with a deposited energy typical of a proton (order of one MIP), otherwise $TH(i,j) = 0$. Its distribution as function of the particle rigidity is shown in Fig. 3.21 together with the function used as upper limit for the selection: a proton/pion interacting after a few planes or non interacting will result in high values of the quantity $noint$, while in the case of electromagnetic showers developing in the first planes this variable will have low values.
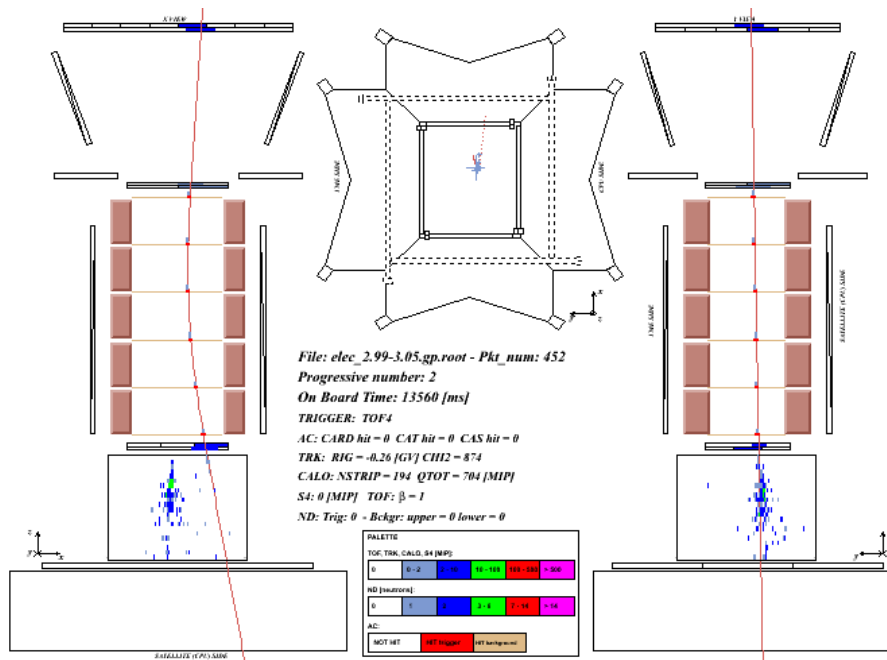
3.6.3   Double showers

Figure (3.22)   *An electron from flight data having a very low reconstructed rigidity value from the tracker. The signature of the emitted bremsstrahlung photon, which carries most of the energy of the incident electron, is clearly visible as a shower in the calorimeter, away from the track.*

The presence of a double shower in the calorimeter, not associated to multiple track in the tracking system, very likely indicates the event to be a positron/electron. The amount of material present above the tracking system is equivalent to $\sim 3 \ g/cm^2$. This implies

that an incident positron has a certain probability to emit a bremsstrahlung photon along its path. In case this happens, the emitted photon could convert above the tracking system, giving rise to a multiple track event in the tracking system, or traverse the tracker length and shower in the calorimeter beneath. When the incident particle energy is high the emitted photon is collimated respect to the primary and the finite spatial resolution of the calorimeter does not allow to distinguish a double shower in the detector. When the energy is lower, the bending of the primary charged particle in the PAMELA magnetic field separates the shower due to the positron/electron from the photon one. Figure 3.22 shows a low energy electron from flight data, which has emitted a photon along its trajectory; the calorimeter reconstructs the electromagnetic shower associated to the photon quite far from the electron track, while the charged particle does not produce any shower (limit case). Because of the bending in the magnetic field, that increases the differences between the photon and electron trajectories, the double shower feature is generally only visible in the calorimeter sensitive planes of the x view.

The rigidity reconstructed by the tracker is obviously not representative of the real particle initial energy, because it can not measure the amount of energy associated to the neutral product of the radiation process. However the calorimeter can measure the total energy deposited by both the particles and it is possible to correctly reconstruct the energy at the top of the payload (see Sec. 5.1.2).

The algorithm used to identify such events has been derived by the Boezio (1998) work, where it was used for the analysis of the CAPRICE94 $e^\pm$ data, and will be briefly described in the following. After a back extrapolation of the electron track in the spectrometer to the ToF upper plane and the cover, the expected direction of the emitted photon is calculated. The opening angles of bremsstrahlung processes are $\theta_{brem} \propto mc^2/E$ with m and E being the mass and the initial energy of the radiating electron, respectively. For energies of 200 MeV and above the θ_{brem} is less than 3 mrad, which corresponds to few millimeters deviation after a path length of 1 meter. Then, the position of the photon inside the calorimeter is obtained. If an electromagnetic shower is found in this position, this event is classified as having an accompanying shower. In case the photon is emitted in S2 or in the tracker system it would induce a shower in a different position inside the calorimeter and, consequently, would not be identified by the previous method. However, such an event can be identified by scanning the calorimeter searching for a second shower, without confining the search to a precise position in the detector.

The method identifies events according to the following categories:

type 1: no second shower found,

type 2: a second shower, which direction points back to the top of the instrument is found,

type 3: a second shower with no defined emission point is found.

Simulation shows that, depending on energy, $\sim 10 - 20\%$ of the electrons belong to type 2 events, and that this is a safe signature of electron/positron event: thus, despite the wrong assigning of the rigidity by the tracker, in this analysis they are not rejected.

3.7   Residual background estimation

The sample of electrons and positrons that survived the described selection chain is constituted of 16279 e^+ and 178151 e^-, detected by the PAMELA instrument in the energy range $0.2 - 3.0$ GeV between July 2006 and December 2008. The β-rigidity distribution of the selected particle sample is shown in Fig. 3.23, where all the selections have been applied except the requirement of relativistic particles. The red line corresponds to the β selection cut, that can reject residual slow particles (pions and protons) at low rigidities. Still some contamination from relativistic pions and protons could be present in the most
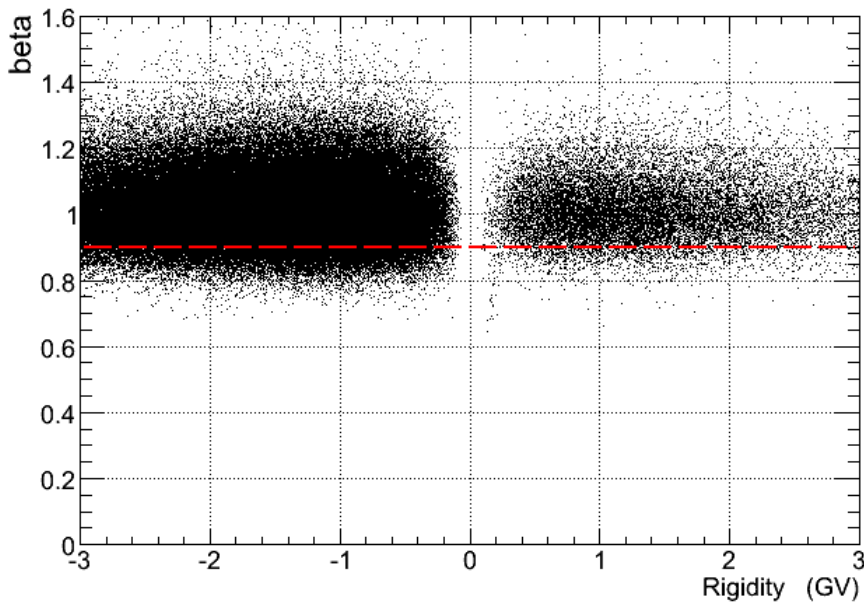

Figure (3.23)   *β-rigidity distribution of particles selected as electrons and positrons with the previous section cuts. The red line shows the relativistic β selection.*

critical sector, the positive particle one. In the following, the evaluation of the residual contamination and the related correction to the selected positron sample are described. While above ~ 1 GV the proton background is the major issue we have to deal with, pion

contamination is present at low rigidities.

Terminology   Before proceeding it is convenient to briefly define some terminology that will be used in the following.

Le us define two sets of events: good events, whose selection we are interested in, belong to the sample of events A, while B is the sample of background events that we want to reject by the use of a set of criteria S. We can define the following entities with reference to S:

- *efficiency ϵ*: fraction of events of A identified as A events by S

- *contamination c*: fraction of events of B identified as A events by S

- *rejection factor R*: ratio between efficiency and contamination (ϵ/c)
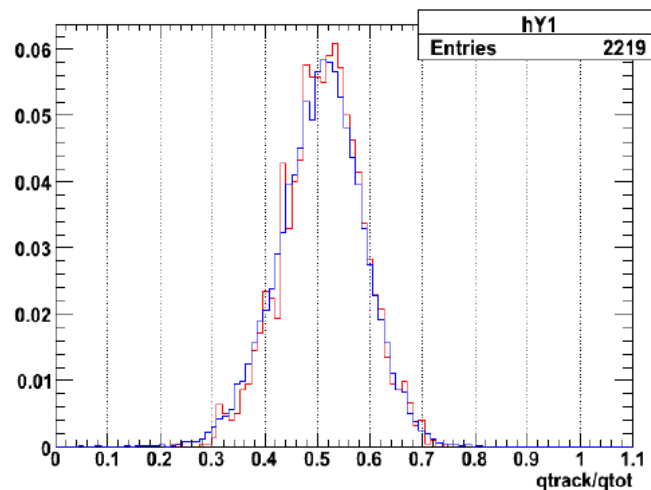
Figure (3.24)   *Fraction of energy released in the strip closest to the track and the neighboring strip for particles in the rigidity interval 0.9 - 1.1 GV.*
.

3.7.1   Proton contamination

Below 0.8 GV protons are rejected using dE/dx and β measurements and the remaining contamination is reasonably assumed to be zero. This is supported by simulation and confirmed by the symmetry between the distributions of calorimetric variables of the final sample of electrons and positrons. At higher energies the calorimeter provides the main contribution to the instrument rejection power.

As a first check, the distributions of the $e^\pm$ candidates selected by the calorimeter have been compared. Fig. 1.24 shows the distribution of the fraction of energy released in the strip closest to the track and the neighbouring strip on each side for positive (red) and negative (blue) particles selected as positrons and electrons in the rigidity range from 0.9 to 1.1 GV. A Kolmogorov-Smirnoff test has been performed to check the compatibility in the various energy ranges, which has given satisfying results. Then, both real data and simulation have been used to evaluate the maximum number of residual contamining protons in the positron sample above 0.8 GV. The sample of positron candidates obtained applying all the selections, calorimeter excluded, contains a large fraction of protons and a small fraction of positrons. Assuming all the particles in the sample to be protons, an upper limit to the proton contamination can be estimated by convoluting the distribution of events with the calorimeter cuts.

A set of protons has been selected from flight data to estimate the contamination of the calorimeter selections. The proton sample has been chosen excluding the lepton component on the basis of the electron data according to the following requirements:

1. a proton-like energy release on S1, S2 and tracker,

2. β not compatible with the velocity distribution of electrons from flight data.

Thanks to these selections, it has been possible to obtain a clean sample of protons with a significant statistics in the rigidity range $0.8 - 1.5$ GV, to be used to study the calorimeter cuts effect on the most abundant particle species in cosmic rays. For each rigidity bin the number of protons of the initial sample, $N^0(\text{p})$, is given in Tab. 3.1. The calorimeter selections leave a residual number of protons, $N(\text{p})$, which corresponds to a contamination that is reported in the third column of the same table, with a confidence level of 68.3% [10].

A simulated set of protons has been generated to compare the result obtained and to extend the energy range up to 3.0 GV. A proton spectrum in the rigidity interval 0.4 to $20.$ GV with a uniform arrival distribution was simulated and all events where the primary particle traversed S3 were saved. The calorimeter contamination has been calculated as the fraction of particles passing the calorimeter cuts, respect to the sample of particles selected by the same conditions posed on real data. The resulting contamination is reported in Tab. 3.1 for the energy bins where a comparison with flight data was possible. The level of the agreement id connected to the statistics of the simulation but can justify the use of it from 1.5 to 3.0 GV.

The upper limit to the number of proton events present in the final positron sample is given in Tab. 3.2 for each rigidity bin from 0.9 to 3.0 GV, together with the corresponding contaminant fraction. Then, this is added as a systematic error.

---

[10]For more about the error calculation see Chapter 4.

Rigidity range (GV)	N^0 (p)	N (p)	Contamination (real data) ($\times 10^{-5}$)	Contamination (simulation) ($\times 10^{-5}$)
0.7 - 0.9	678841	8	$1.18^{+0.47}_{-0.37}$	$1.87^{+2.81}_{-1.37}$
0.9 - 1.1	604498	2	$0.33^{+0.31}_{-0.18}$	< 2.83
1.1 - 1.3	90957	0	< 1.2	< 2.71
1.3 - 1.5	14938	0	< 7.7	< 2.91

Table (3.1) *For each rigidity bin where it was possible, a number $N^0(p)$ of protons has been selected from flight data, and a number $N(p)$ survived the calorimeter cuts. This corresponds to a contamination, for the calorimeter selection, which is reported in the fourth column and compared with that estimated by simulation (last column).*

Rigidity range (GV)	N (p)
0.7 - 0.9	0.06 ± 0.02
0.9 - 1.1	$0.017^{-0.009}_{+0.016}$
1.1 - 1.3	0.19
1.3 - 1.5	5.0
1.5 - 1.7	2.2
1.7 - 2.0	3.8
2.0 - 2.3	11.3
2.3 - 2.6	15.2
2.6 - 3.0	13.7

Table (3.2) *Estimated upper limit to the number of protons present in the final positron sample.*

An independent analysis has been carried on at energies higher than 1.5 GV, which estimates the proton contamination totally independently from simulation, by the use of a statistical method only based on real data (Boezio *et al.*, 2009). The same method does not find an application in the lower energy range due to the necessity of stronger calorimeter selections. The two results have been compared in the overlapping energy range and have been found in good agreement. This is a further confirm about the quality of the selection.

3.7.2   Pion contamination
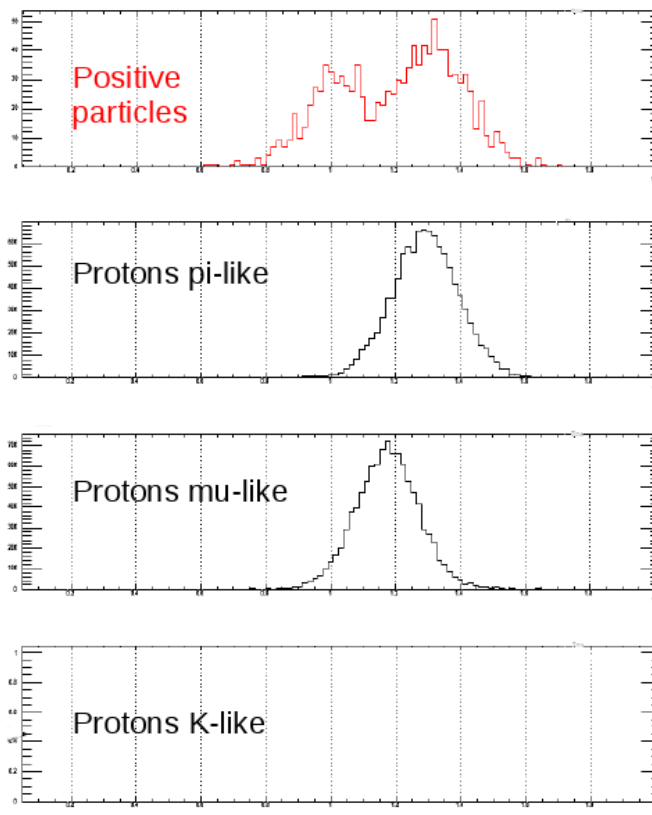
Figure (3.25)   *Beta distributions for positive particles fulfilling the tracker, Tof and AC e^+ selections in the interval 0.1-0.2 GV (top panel). Proton distributions in rigidity ranges beta-equivalent to the mentioned one, are plotted in black for pions, muons and kaons, respectively from top to bottom.*

Besides protons, low energy positively charged particles heavier than positrons, like muons, kaons and pions, could be present in the selected sample. According to their β distribution these particles, non relativistic below 200 MV, are mainly pions: a straightforward calculation shows that the pion, muon and kaon β distributions in the interval

0.1-0.2 GV correspond to the proton β distributions respectively in the rigidity intervals 0.67 - 1.34 GV, 0.89 - 1.77 GV and 0.19 - 0.38 GV. Fig. 3.25 shows such distributions as obtained from flight data, where positive particles selected as positrons with tracker, AC and ToF system (obviously no β cut has been applied) are in red, while protons selected in the above mentioned rigidity intervals are in black.

These pions are not expected to be a primary component of the cosmic radiation, instead, there is some small probability that cosmic-ray primary particles, interacting with the material above PAMELA give rise to a non negligible component of secondary pions. As
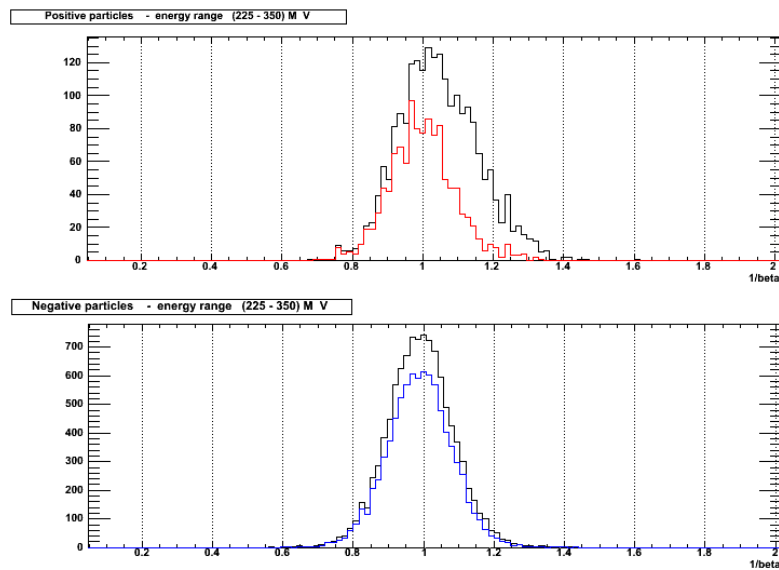
Figure (3.26) *Black lines show the $1/beta$ distribution for positive (top) and negative (bottom) particles after the application of all the selections, except the β and calorimeter ones, in the rigidity range $(225 - 350)$ MV. The distribution of events that fulfill also the calorimeter criteria is shown in red and blue, respectively for positive and negative particles.*

previously shown, the amount of background from secondaries in the positron sample can be substantially reduced by the application of the positron selections on tracker, AC and ToF. The effect of the β and dE/dx cuts on pions is to reject them in the very low part of the energy range (< 200 MeV), where pions are slower than positrons and release more energy in the sensitive planes of ToF and tracker. In case the tracked pion is accompanied by other secondary particles produced in the top part of the instrument, there is high probability that the anticounters can detect them. The residual pion component is constituted by relativistic particles with a clean pattern inside the instrument and no associated detectable secondaries; in this case the rejection power is provided by the calorimeter. Still an irreducible pion background could be present in the final electron and positron

samples.

Fig. 3.26 shows the effect of the calorimeter selections in the energy range $0.225 - 0.350$ GV. Positive (top panel) and negative (bottom panel) particles selected with all the selection criteria except the β and calorimeter cuts, are represented by the black histograms. The distribution of $1/\beta$ should peak at 1 for relativistic particles, as it happens for the negative particle plot while on the positive side a large non gaussian tail is present at $1/\beta > 1$, determined by pions. The blue and red lines show the situation after the calorimeter cuts application, indicating that the positive pion component is still present and to be estimated.

As it will be shown in the following, the amount of residual pion contamination can be considered negligible for negatively charged particles, while this is not the case on the positive side: positive and negative pions are produced mainly by cosmic primary protons at approximately the same rate, while the fluxes they have to be compared with (e^- and e^+) have one order of magnitude of difference.

Both real data and simulation have been used to evaluate the residual pion number in the final positron sample. Let us indicate with S the set of calorimeter selections and the relativistic particle requirement; there is the possibility to measure the pion and lepton yields before S, below 200 MV, where π are not yet relativistic while leptons are. This provides the value of the initial pion contamination[11]. Then, the convolution of the initial pion contamination with the S rejection factor provides an estimation of the residual π^+ contamination on the final e^+ sample. The rejection factor of the calorimeter has been derived by simulation while the effect of the β selection has been studied on real data.

Pion simulation   In order to reasonably estimate the pion contamination in the positron sample, a reliable simulation of the expected positive pion yield is needed. The production of a realistic rigidity and spatial distribution of the pions that can constitute a background for positron measurements requires a large statistic of protons (the main responsible of the pion production through inelastic collisions with the cover and instrument material). A proton yield corresponding to ~ 7 years of PAMELA data taking has been simulated. The input spectrum has been averaged along the PAMELA orbit to take into account the effect of the satellite passage into regions characterized by different geomagnetic cutoff. The contribution from He, as representative of the whole nuclei one, has been also evaluated. Since the interactions that produce pions are rare, the simulation work (Bruno, 2009) has been accomplished in two steps, keeping separate the generation of secondaries by proton interactions in the top part of the instrument and the simulation of their transport in the rest of the instrument, in order to reduce the amount of processing time. In the first

---

[11]Notice that in this context we indicate with *contamination* the amount of pions in the initial positron sample.

step only the top part of the apparatus, which includes the details of the top pressurized container and the S1 scintillators, has been simulated. Only events that could potentially cause a secondary particle have been saved for later processing, namely, those events that fulfill the following requirements: 1) an inelastic reaction occurred, 2) at least a signal is present in S1, 3) at least one secondary produced particle has the trajectory contained in the spectrometer acceptance. During the second step, the secondary particle interaction in the instrument is completely simulated. Among the interaction products, the main component is constituted by $\pi^\pm$ with a minor contribution from K^+ and μ^+.
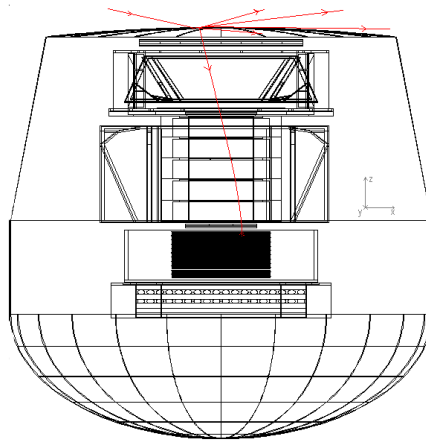
Figure (3.27) *An illustration of a proton interacting with the Al cover above the PAMELA instrument producing secondaries. One of them enters the experiment acceptance without other accompaning particles hitting the anticounter shielding nor producing an additional track. If the particle is relativistic and do not release more than ~ 1 MIP in the ToF and tracker sensitive planes, this kind of event can be rejected from the positron sample only by the calorimeter.*

The simulation has been validated by the work of Hofverberg (2009) and Bruno (2009) in the explored energy range by comparing the pion yield as obtained by simulation with the pion spectrum measured in flight (see next paragraph). The result is reported in Fig. 3.28 showing that the agreement between simulated and flight data is very good.

Pions from flight data In order to evaluate the rejection power of the β selection ($\beta > 0.9$) a pion and an electron sample has been selected from flight data to derive the contamination and the efficiency corresponding to the selection of relativistic particles. The criteria to select electrons in the energy range from 0.2 to 20 GeV will be described in the next chapter; the β-cut resulting efficiency has been found to be constant and equal to 92.2%.
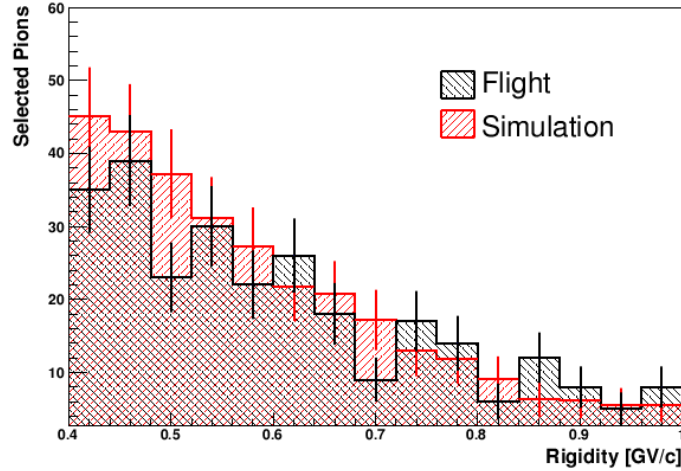
Figure (3.28)   *Selected flight (black) and simulated (red) negative pions from* Hofverberg *(2009) and* Bruno *(2009).*

A sample of negatively[12] charged pions can be unambiguously selected in flight in the interval 0.2-1.0 GV by using the ToF system to reject antiprotons, and the calorimeter against electrons. The selections applied can be summarized as follows:

- single particle,

- non interacting in the calorimeter,

- β not compatible with the proton one.

The selected pions and the contamination corresponding to the β selection are shown in Fig. 3.29. Since pions are already relativistic at approximately 1 GV it is reasonable to extrapolate the contamination at higher rigidities.
The corresponding rejection factor R_β is represented in blue in Fig. 3.30, while the black one, R_{calo}, refers to the calorimeter selections. The final rejection power of S can be obtained as $R = R_\beta \cdot R_{calo}$, since the two detectors involved in the analysis are independent.
  While the β selection is more effective in rejecting low energy pions, as expected, the calorimeter rejection power increases at high energy, where showers are more developed and the hadron-lepton differences are more clear.
Let the residual pion contamination present before the selection S be C^0; then, the fraction

---

[12]We exploit the symmetry between π^+ and π^- in the β-rigidity distribution avoiding to deal with the rejection of a huge amount of protons at rigidities where protons become relativistic, close to the upper edge of the considered range.
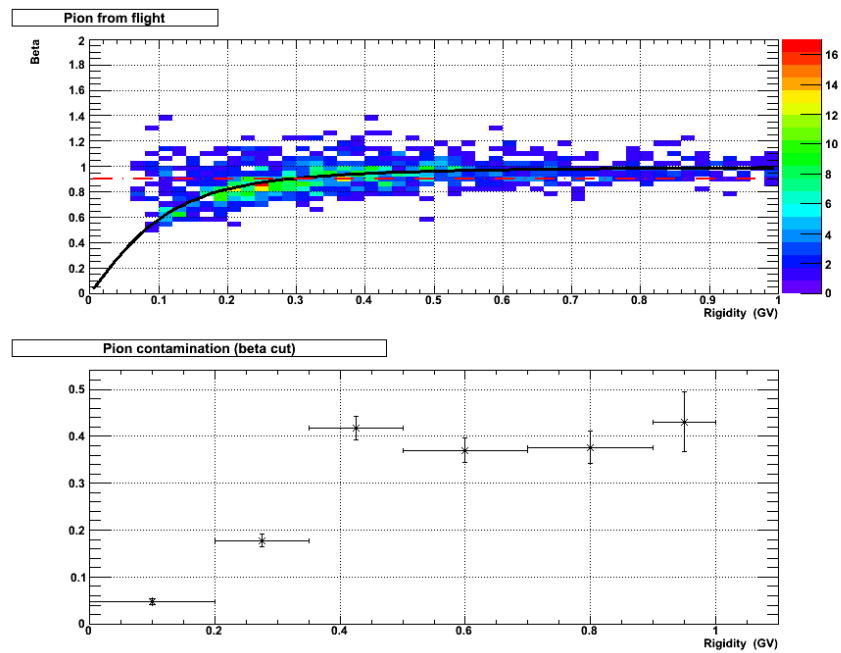
Figure (3.29)   *Top panel: β-rigidity distribution of the negative pions selected in flight. The black line shows the expected relation for pions while the red one represents the selection cut. Bottom panel: contamination relative to the β selection.*
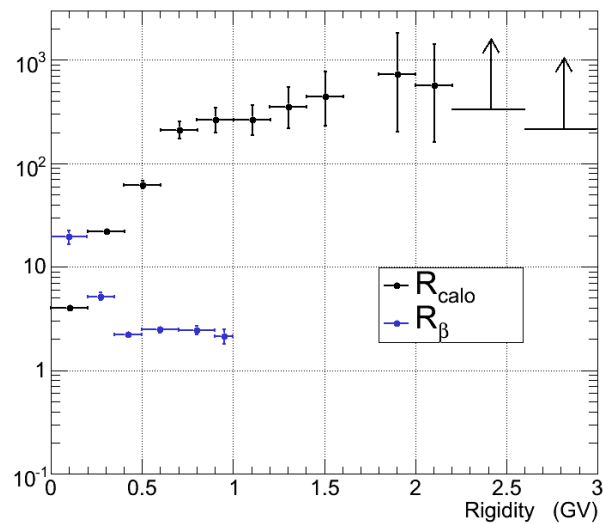

Figure (3.30)   *Rejection factor of the β selection (in blue) and calorimeter selections (in black).*

of π^+ in the final e^+ sample can be calculated as:

$$C(x) = \frac{C^0(x)}{R(x)} \tag{3.11}$$

where each term of the equality depends on rigidity (x).

As mentioned, it is possible to measure C^0 only below 200 MV, where the pion β distribution is rather separated from that of relativistic particles. Since below 2 GV the pion spectrum is definitely steeper than the electron one (see Fig. 3.28), we can reasonably consider the value $C(x) = C^0_{200}/R(x)$ as an upper limit to the *true* value of $C(x)$, being C^0_{200} the contamination below 200 MV.

In figure 3.31 the $1/\beta$ distributions of positive (top) and negative (bottom) particles, for rigidities less than 200 MV, are shown. These events have been already cleaned by the selections that precede the set S. What is soon noticeable on the positive side is the presence of a peak at $1/\beta \simeq 1.27$ due to non relativistic particles, that is almost invisible on the negative side. The π^+/e^+ and π^-/e^- ratios can be obtained by a gaussian double fit. While for relativistic particles the $1/\beta$ distribution is expected to be gaussian whichever energy range is considered, this is not true for non relativistic particles whose gaussianity is distorced due to the β-rigidity shape. However, it has to be noticed that the considered energy bin is not uniformly populated by pions because of the decrease of the instrument acceptance at lower rigidities: most of the detected pions have rigidities close to the upper edge of the interval, so that the effective bin width is smaller than the 'nominal' one. Thus, in first approximation, it is possible to fit with a gaussian even the non relativistic particle peak. The result of the double fit is shown as a black line in figure; the single distribution functions for leptons and pions have been obtained using the parameters of the double gaussian function. The resulting particle ratios are reported in Tab. 3.3, last column.

π^+/e^+	78.6%
π^-/e^-	3.4%
π^+/π^-	3.1

Table (3.3) *Relative $\pi^\pm$ and $e^\pm$ numbers as detected below 200 MV.*

The value of the π^+/π^- ratio reflects the fact that, depending on the primary proton energy, the cross section for π^+ production is greater than for π^-.

The application of Eq. 3.11, with $C^0 = 0.786$ from Tab. 3.3, leads to an estimated number of π^+ in the e^+ sample which is reported in Tab.3.4.

The level of negative pion contamination on the electron sample is already well under control and less than 5 per mil after the β cut, thus it can be safely considered zero when
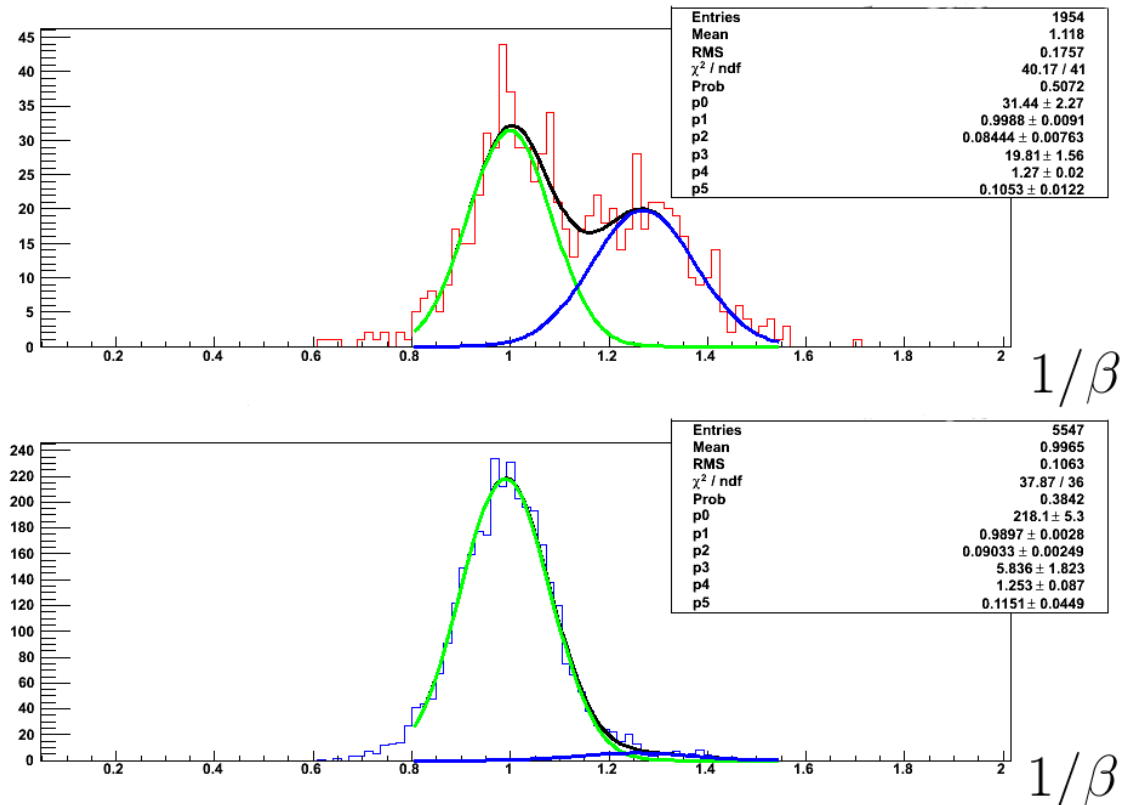
all the selections are applied.

Figure illustration with statistics boxes:

Top panel:

Entries	1954
Mean	1.118
RMS	0.1757
χ^2 / ndf	40.17 / 41
Prob	0.5072
p0	31.44 ± 2.27
p1	0.9988 ± 0.0091
p2	0.08444 ± 0.00763
p3	19.81 ± 1.56
p4	1.27 ± 0.02
p5	0.1053 ± 0.0122

Bottom panel:

Entries	5547
Mean	0.9965
RMS	0.1063
χ^2 / ndf	37.87 / 36
Prob	0.3842
p0	218.1 ± 5.3
p1	0.9897 ± 0.0028
p2	0.09033 ± 0.00249
p3	5.836 ± 1.823
p4	1.253 ± 0.087
p5	0.1151 ± 0.0449

Figure (3.31) *Top panel: $1/\beta$ distribution for positive particles with rigidity less than 200 MV that fulfill the positron selections on tracker, ToF and AC. Bottom panel: the same distribution for negatively charged particles.*

3.8 The final $e^\pm$ sample

Figure 3.32 aims to summarize the effect that the selections described in this chapter have on the detected number of positive and negative particles, each graph referring to a different cut.

The blue line represents a set of events associated to a single track in the magnetic spectrometer, good according to the tracker selection cuts, and not accompanied by secondary particles that produce a shower in the top part of the apparatus, since nor the ToF nor the AC system have detected any multiple particle.

The subsequent cut selects galactic particles and, as expected, mostly rejects events at low
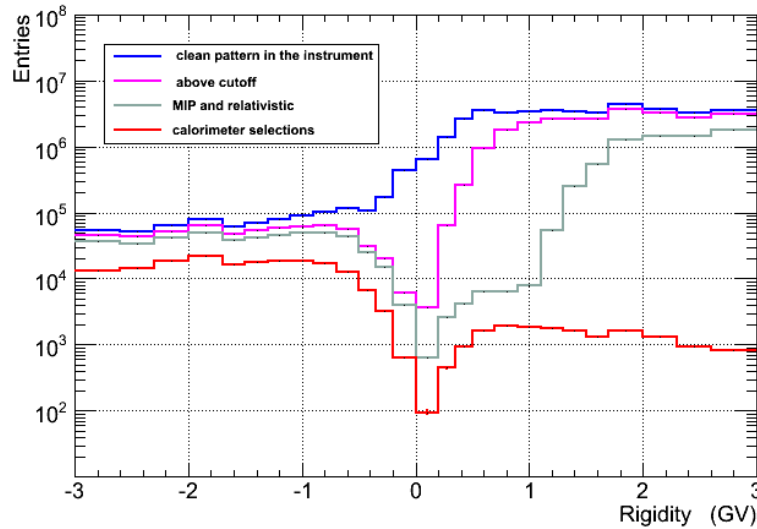
Figure (3.32) *Effect of the selection chain on the negative and positive particle samples.*

energy.

The third selection of the cut cascade acts on the particle velocity and energy release on the Tof system and tracker planes, distinguishing minimum ionizing, relativistic particles. Due to the higher level of contaminating hadrons, the effect of this selection is more visible on the positive particle side, while on the negative (electron-dominated) part the particle number decrease is almost solely due to inefficiency. Above ~ 1 GV this selections have not effect any more in rejecting protons: the number of positive particles starts to rise of about two orders of magnitude and the ratio between positive and negative gets larger and larger. However, the calorimeter selections can successfully clean the positron sample from protons above ~ 0.8 GV, leaving a residual contamination whose upper limit was estimated studying real and simulated data; its value in each rigidity range is reported in the fourth column of Tab. 3.4. At low energy the situation is more complicated due to the fact that pions become relativistic at few hundreds of MV and that they could fake electromagnetic showers when interacting in the calorimeter. It is not possible to get an independent pion sample to estimate the contamination from without the calorimeter, thus the rejection factor was estimated by the use of a simulation, whose reliability was checked.

Table 3.4 summarizes the number of electrons and positrons detected by the PAMELA experiment according to the set of selections defined in this chapter and the estimated contamination from p and π^+. The derived upper limits upper limits to the p and π^+ contamination of the e^+ sample are as systematic errors in the analysis.

In principle looser conditions could be used for the e^- selection because nor the antipro-

Rigidity range (GV)	N_{e^-}	N_{e^+}	N_p	N_{π^+}
$0.2 - 0.35$	3234	443		3.1 ± 0.3
$0.35 - 0.5$	6777	944		5.8 ± 0.6
$0.5 - 0.7$	12596	1643		3.4 ± 0.5
$0.7 - 0.9$	16978	1936	0.06 ± 0.02	$2.6^{+0.7}_{-0.6}$
$0.9 - 1.1$	18331	1869	$0.017^{+0.016}_{-0.009}$	$2.2^{+0.7}_{-0.6}$
$1.1 - 1.3$	18829	1786	0.19	$1.8^{+0.7}_{-0.5}$
$1.3 - 1.5$	17732	1625	5.0	1.3
$1.5 - 1.7$	16134	1311	2.2	0.80
$1.7 - 2.0$	21813	1655	3.8	0.77
$2.0 - 2.3$	18528	1309	11.3	0.83
$2.3 - 2.6$	14159	920	15.2	0.93
$2.6 - 3.0$	13040	838	13.7	1.25

Table (3.4) *This table summarizes the number of electrons and positrons, N_{e^-} and N_{e^+}, detected by the PAMELA experiment from July 2006 to December 2008. The residual contamination of p and π^+ in the e^+ sample was estimated and the upper limits to the number of contamining particles is reported in the last two columns, N_p ans N_{π^+}.*

tons nor negative pions constitute a background and the proton background (spillover p) is not present at this energies. However, for having a better control of systematic errors the same cuts are used both for the positrons and the electron analysis, when deriving the positron fraction. In chapter 5 an electron flux extended to 20 GeV, obtained with cuts loser above 0.5 GV, and hence higher statistics and smaller errors, will also be presented.

Chapter 4

Selection efficiencies

The number of electrons and positrons detected by the PAMELA instrument depends on the particle flux in space and on instrumental characteristics. Thus, the apparatus response has to be carefully evaluated in order to correctly derive the original particle flux from the countings of acquired events. This chapter describes two among several effects that participate to the definition of the PAMELA response: the acceptance and efficiency.

4.1 Efficiency calculation and other instrumental effects

It is possible to summarize two among the main instrumental factors that determine the PAMELA apparatus response to a flux of incident electrons and positrons in the following way:

- **the geometrical factor**: the instrument geometrical factor represents the geometrical constraints of a particle telescope. It does not depend on the particle characteristics; however, if a magnetic field is present as in the PAMELA case, the geometrical factor has a dependence on the particle rigidity;

- **the instrument efficiency**: the detection efficiency is defined as the fraction of incident particles, satisfying the geometrical factor requirements, which are detected and fulfill the whole set of selection criteria. Assuming no correlation between the different detectors it is possible to derive the total instrument efficiency ϵ_{TOT} as the product of the following terms:

    - *tracker efficiency, ϵ_{trk},* in reconstructing the particle trajectory, determining its rigidity and sign of charge;

    - *Time of Flight efficiency, ϵ_{ToF},* which includes not only the positron selection efficiency, ϵ_{ToF}^{sel}, but also the efficiency related to the generation of a trigger signal, ϵ_{ToF}^{trig};

- *anti-counter system efficiency, ϵ_{AC};*

- *calorimeter efficiency, ϵ_{calo},* in the discrimination of leptons from hadrons.

The efficiency ϵ_i of the selections that involve each sub-detector is derived as the fraction of events of an initial sample of electrons that fulfills the selection criteria. The sample of particles to be used for the efficiency determination can be obtained from simulation, test beam or flight data. Which is the best technique to apply is not clear a priori, depending on the experimental setup and on the detector under study. Data from simulations and test beam allow a good control and understanding of the measurement, but on the other hand their result could be not directly applicable to experimental data due to the instrument condition in flight. In this respects, a sample of particles selected in flight would be preferable as representative of the real experimental situation. In this case, the particle selection has to be done with care in order to avoid biases in the initial sample. This can be in some cases an issue, and constitutes the drawback of this method, since the type and momentum of the particles of the initial sample have to be measured by an independent set of detector and, if the efficiencies are correlated, this could give rise to biases. Moreover, sometimes there is only a detector able to select a clean set of a certain type of particle, so that its efficiency have to be calculated by simulation and on ground beam tests.

In this work both flight and simulated data have been used to derive the total selection efficiency combining those obtained for the single detectors.Where it was possible, a set of electrons has been chosen from flight data, leaving to the simulation the sole function to support the result.

The only efficiency that was derived by simulation and corrected, in a second phase, by a factor obtained for comparison with real data, is the tracking efficiency. The approach that has been followed implies, as it will be explained in detail, that this efficiency is convoluted with the PAMELA geometrical factor into the instrument *acceptance*.

The final total efficiency takes into account the following effects and particle characteristics:

1. interactions of the particle with the instrument,

2. energy of the incoming particle,

3. charge of the incoming particle,

4. time dependence.

In the following, we describe a common technique for the calculation of efficiency that has been adopted in this work. An initial sample A of events is chosen for the

efficiency evaluation and a first histogram is built, which plots the distribution of the quantity of interest for this sample of events. A second histogram, identically binned, plots the same distribution only for events (sample B) that satisfy the condition, whose efficiency one is interested in. The best estimate for the unknown efficiency in the i-th bin is $(N_A/N_B)_i$, where N_j is the number of events belonging to the sample j.

Calculation of efficiency error The statistical uncertainties associated to the efficiency estimate can be calculated in several ways; commonly Poisson and binomial errors are assumed. In the Poisson case, the error is defined in such a way that, if the whole set of the events belonging to the initial sample fails the cut, we know with complete certainty that the efficiency is exactly 0, independently on the initial number of events; on the other hand, if all events pass the selection, the error calculation can lead to an efficiency greater than 1. In the binomial case this last eventuality does not happen, but still the case of a certain claim of $\epsilon = 1$ can occur. Thus, both the choices lead to absurd results in limiting cases.

A simple alternative for calculating the efficiency and its statistical uncertainties in a manner that agrees with our reasonable expectations, even in limiting cases, is provided by the Bayes theorem and will be adopted in this work. The most probable value of ϵ, and a confidence interval for it, are determined from data (an observation of k events out of N passing the cuts) by deriving, according to the theorem, the probability that the true efficiency is between ϵ and $\epsilon + d\epsilon$ from the probability that k events will pass the cuts, given the condition that the true efficiency is ϵ and that the process is binomial (see Paterno, 2004, for details). In the following, a 68.3% confidence level is used to assign the errors according to the described method.

4.2 The instrument acceptance

The geometrical factor G of an ideal[1] telescope is the proportionality factor which relates the instrument counting rate, C, to the incident intensity, I_0:

$$C = GI_0 \tag{4.1}$$

where I_0 is isotropic. In the general formulation the geometrical factor is measured in $cm^2 sr$ and can be calculated as (Sullivan, 1971):

$$G = \int_\Omega d\omega \, A(\omega) \tag{4.2}$$

---

[1] the instrument efficiency for the detection of particles of a given type is one.

where $d\omega$ is the element of solid angle and Ω its domain, and $A(\omega)$ is the instrument directional response function. $A(\omega)$ is defined as:

$$A(\omega) = \int_S d\bar{\sigma} \cdot \hat{r}. \tag{4.3}$$

where $\hat{r}$ is the unit vector in the direction ω and $d\bar{\sigma} \cdot \hat{r}$ is the effective element of area looking into ω (see Fig. 4.1). The determination of G is usually handled by
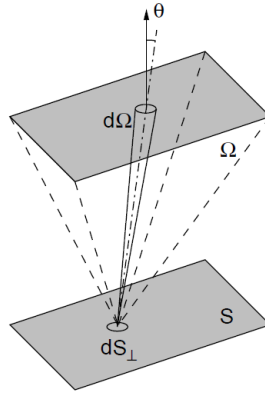

Figure (4.1)   *Schematic view of a particle telescope consisting of two thin detectors and elements for the geometrical factor calculation: S is the detecting surface and Ω is the solid angle seen by each of the surface elements $dS_\perp$ perpendicular to a track incident with an incidence angle θ.*

approximation, however a few explicit formulae are known for the easier cases. It is possible to demonstrate that for a single element telescope, consisting of a single planar detector with area A, the following expression for the geometrical factor holds:

$$G = \pi A \tag{4.4}$$

In order to evaluate the Eq. 4.1, numerical methods or a Monte Carlo approach are usually adopted. In the PAMELA case, both the techniques have been explored, as reported in previous works (Bruno, 2009, and references therein). To make the comparison feasible, the simulation setup has been simplified: the instrument geometry was reduced only to those volumes that define the instrument acceptance (ToF and tracker planes), while both the detector insensitive volumes (boxes, carbon-fiber rails, glue, aluminium frames, etc.) and the physical interactions have been neglected. A more thorough evaluation of G includes not only the influence of the spectrometer magnetic field, but also effects like energy losses, deflection of the

primary particle respect to the original trajectory and production of secondary particles. In this work, a full simulation setup has been used to obtain a geometrical factor G_{PAM} that takes into account the mentioned effects. The calculation procedure will be described in the following:

1. particles were randomly produced on a generation surface S ($70 \times 60 \ cm^2$) placed $5 \ cm$ above the aluminium container of the instrument. Their trajectory is univocally determined by the choice of the generation point (x_0, y_0) and the angles of incidence (θ, ϕ). An isotropic intensity have been simulated by randomly choosing x_0, y_0, ϕ and $\cos^2 \theta$ according to an uniform distribution on S and in a 2π solid angle[2].

2. The particle trajectories have been followed to see if they pass through the detectors of interest, satisfying the conditions that define the instrument acceptance and that will be described in the following. Only in this case the particles were selected as good events.

3. The previous steps are repeated to let a statistical pattern emerge.

Then, the geometrical factor is derived as:

$$G_{PAM} = \frac{n_{sel}}{n_{tot}} G_S \tag{4.5}$$

where n_{sel} is the number of good events, n_{tot} the total number of generated particles and G_S the geometrical factor of the generation surface that can be calculated from Eq. 4.4.

The set of selections which determines the n_{sel} sample consists in: 1) the primary particle hits the ToF planes reproducing the main trigger configuration 2) a good track, according to the basic selections of Sec. 3.2, is associated to the triggering primary. While the first condition makes the sample of selected events dependent on the geometry of the apparatus, on its magnetic field and the interactions of electrons with the detector materials, the second selection adds a dependence on the tracker efficiency in reconstructing the track. Thus, the instrument acceptance calculated according to this procedure convolves the PAMELA geometrical factor and the efficiency of the basic tracker cuts.

A set of $\sim 4 \cdot 10^7$ electrons has been generated in the energy range $(0.05 - 20.0) \ GV$ with GEANT4 simulation. The application of Eq. 4.5 to this data set defines the PAMELA acceptance for electrons and is reported in Fig. 4.2. A fit to the data points is made with the function

$$(x) = (1/f^\alpha + 1/A^\alpha)^{-1/\alpha}, \quad \text{with } f = B + C \cdot \log_{10}(x) \tag{4.6}$$

---

[2] the angular domain has been limited only to downward particles.

Instrument acceptance
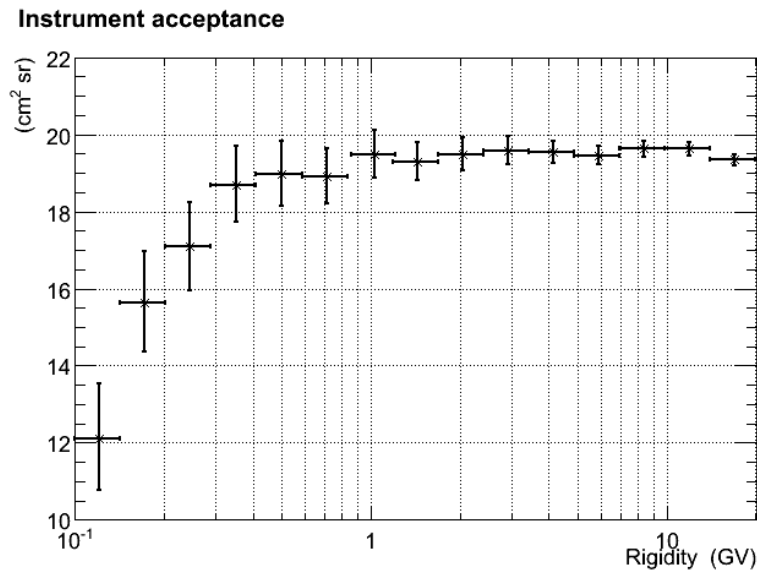
Figure (4.2)   *PAMELA acceptance as derived for electrons from simulation.*

where x is the rigidity in GV. The fit parameters have been found to be: $A = 19.5$, $B = 43.7$, $C = 33.8$, $\alpha = 3.7$.

The plot shows that the acceptance window varies with the incident particle rigidity decreasing at low rigidities, as expected due to the presence of the tracker magnetic field: low energy electrons are bent more than higher energy particles and more likely go out of acceptance, towards the walls of the magnetic cavity, and are lost before they can reach the lower silicon plane or S3.

4.3   The tracker selection efficiency

Once the tracking algorithm has found a track and the rigidity information associated to the event is available, it is possible to explore the energy dependence of the selection efficiencies and effects related to other variables, such as time. In order to do this with a high enough statistics, a set of electrons generated directly into acceptance has been used: as previously mentioned, the simulation of an incident isotropic flux from 2π is necessary to properly derive the instrument acceptance, but the method has the drawback of being very time consuming, due to the large amount of particles that have to be followed along their trajectory with the inclusion of all the physical interactions.

Once selected a set of events with a good track according to the basic tracker selections, the additional requirements of having particles inside the fiducial acceptance

and a deposited mean energy on the silicon planes compatible with MIP was found to present a rather flat efficiency, as shown in Fig. 4.3. The main contribution to the measured inefficiency is related to the definition of the fiducial acceptance. Another effect that influences the PAMELA tracker efficiency is time.
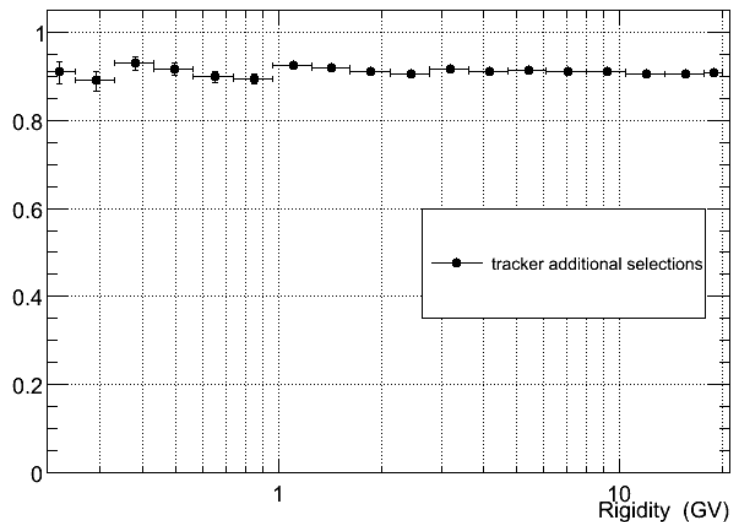
Figure (4.3) *Efficiency of the additional tracker selections (see Sec. 3.2).*

Time dependence The performance of the Viking VA1 chips, responsible of the readout of the tracker, degrades in time; as a consequence, dead areas are created on the tracker planes, where the passage of the charged particle can not be recorded. Due to the reduction of the tracker active area a decrease in the efficiency is expected. Fortunately, since this decrease is related to the electronics, it is possible to monitor it, estimate the entity of the effect and apply a time-dependent correction to the tracker efficiency.

Configurations of malfunctioning chips can be identified in experimental data and reproduced in simulation. The total tracker efficiency, namely the efficiency of the basic and additional cuts (see Sec. 3.2) calculated respect to the number of triggering particles that fulfill the geometrical constraints, is shown in Fig. 4.4 for two different tracker configurations. The two graphs are an example of what was obtained for each month, from July 2006 to December 2008. Simulated data have been produced using the most frequently occurring configuration for each time period, which is an approximation since the pattern of malfunctioning VA1 chips changes within each month; the goodness of this approximation worsens with time accord-

ing to the stability of the most frequently occurring configuration. As visible in figure, for the July 2006 configuration the tracker performance is close to ideal, high and not strongly dependent on rigidity, whereas the simulated tracker efficiency for January 2007 was found to be different in level and structure.

In order not to rely uniquely on the simulation in taking into account the time dependence of the tracker efficiency, a comparison with flight data is needed. A correction factor was calculated on a monthly base for the proton analysis, and has been borrowed in this work[3]. A set of non interacting protons selected by the calorimeter within the PAMELA fiducial acceptance is used as initial sample for the calculation of the monthly variation of the tracker efficiency. The entity of the correction is within few percent. The derived time-dependent factor does not depend on rigidity, since the calorimeter can not provide information about the initial energy of the incoming selected protons. Simulation was used to derive the shape of the dependence on the rigidity.
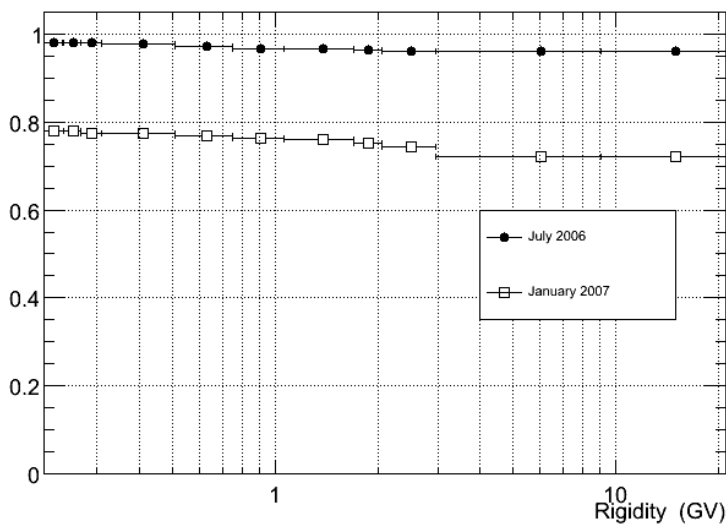
Figure (4.4) *Rigidity and time dependence of the tracker basic selection efficiency as derived from simulation.*

Bias in the calculation of the tracker efficiency. Before applying the acceptance calculated for electrons in Sec. 4.2 even to the positrons data, it is necessary to prove that there is no dependence on the particle sign of charge. Bruno (2009) demon-

---

[3]we assume that the error associated to the use of the same correction factor for electrons and protons is negligible respect to other uncertainties present in the analysis.

strated that the PAMELA geometrical factor is the same for negatively and positively charged particles above 100 MV. Thus, in the energy range explored in this work, the geometrical factor can be considered the same for electrons and positrons. The tracker efficiency could instead present a charge-sign dependent asymmetry due to the different bending of oppositely charged particles in the PAMELA magnetic field. In case of a spatially homogeneous tracker, all arrival directions are equally favored, and the tracking efficiency is expected to be the same. However, if dead areas are present with an inhomogeneous distribution, as for the PAMELA spectrometer, particles with the same rigidity but opposite charge can pass through a different pattern of active regions; this can result in a charge-sign dependent tracker efficiency. The effect is expected to be negligible at high energies, were the par-
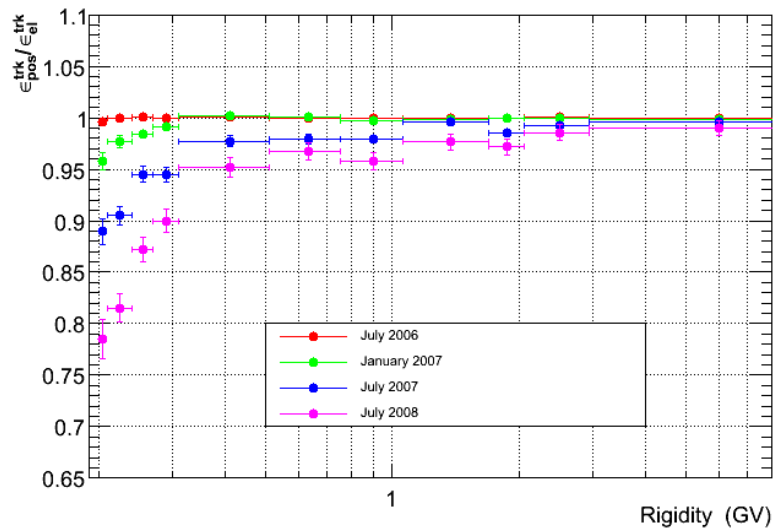
Figure (4.5) *Results from simulated data for the ratio between the tracker basic cut efficiency for positrons and electrons in different time periods. With increasing time the charge-dependent bias in the evaluation of the tracker efficiency emerges, acquiring importance at low energy, where the particles are more bent in the PAMELA magnetic field, according to the increasing inhomogeneity of the tracker sensitive area.*

ticle tracks are close to straight lines, with increasing importance accordingly to the increase of the track curvature. It was verified, studying a sample of electrons and positrons from simulation and real data, that a shift in the distribution of the arrival direction of oppositely charged tracked particles was present at low energy (less than ~ 300 MeV), that was not visible in the higher energy range: this is an

indication of an asymmetry of the tracker efficiency respect to differently charged particles.

The entity of the effect was estimated with simulation: a set of low energy electrons and positrons was generated and the efficiency of the basic tracker selections has been evaluated. Fig. 4.5 shows the ratio of the positron efficiency ϵ_{pos}^{trk} to the electron one ϵ_{el}^{trk}. In July 2006 the ratio is 1 in the whole energy range; electrons begin to be disfavored while time passes and, as expected, the relevance of the effect is larger at low energy. A correction factor was obtained by weighting the curves corresponding to frequent VA1 configurations according to their occurrence into the sample of selected events, resulting of the order of a few percent above 1 GV, increasing at low energy up to $\sim 10\%$.

4.4   The Time of Flight system efficiency

4.4.1   The ToF selection efficiency

The efficiency of the selections that involve the Time of Flight system, ϵ_{ToF}^{sel}, can be evaluated from real data, since it is possible to select a clean sample of electrons with the remaining detectors. The effect of the following criteria, extensively described in Sec. 3.3, has been evaluated:

1. high quality β well defined and positive,

2. $\beta > 0.9$,

3. MIP particles on S1 and S2,

4. clean pattern in the ToF system.

Since these selections are correlated, the total ToF efficiency was not derived as the efficiency product of the single selection efficiencies, but as the efficiency of their chain: the cuts have been applied in cascade and the final efficiency has been evaluated. This avoids possible biases that would probably occur in the other case. The initial sample of particles is selected by the tracker, AC and calorimeter and it is constituted by a clean set of electrons. The following criteria have been used:

- *Clean track*
  The events are selected according to the same tracker quality requirements described in Sec. 3.2 and used in the analysis. In order to avoid possible correlations, the ToF system has not been used for the determination of the track associated to the event. Only negatively charged particles are selected

inside a fiducial area which excludes a border 0.35 cm thick on the silicon planes.

- *Minimum ionizing particle*
  An upper limit to the energy release on the tracker, averaged on the tracker planes, is set. This requirement allows to reject low energy higher mass particles.

- *No AC activity*
  An activity in the anticoincidence system is an indication of the presence of secondary particles produced in interactions of the primaries inside the instrument. CARD and CAT are efficient in rejecting these events that are produced in the top part of the instrument. CAS can add rejection power at low energy (less than 400 MV), where no activity in the scintillator is due to backscattering from the calorimeter.

- *Calorimeter selections*
  As extensively reviewed in Sec. 3.6.2, the PAMELA calorimeter allows to distinguish leptonic from hadronic interactions. Only events presenting a leptonic shower topology are selected, according to the selections described in the previous chapter. Additional conditions are imposed to events with rigidity less than 2.0 GV: they are not included in the initial sample if the energy release on the last silicon plane or in a cylinder of radius 4 strip around the track in the last four planes is different from zero. This selection is able to reject hadrons that do not interact or interact lately, but was developed against splash albedo particles, that cannot be removed from the initial sample by a requirement on β, that would imply the use of the detector under study.

- *Geomagnetic selection*
  Only galactic particles detected in presence of a relatively high geomagnetic field were selected, in order to perform the study in a clean environment, outside the South Atlantic Anomaly.

Fig. 4.6 presents the result of the efficiency evaluation of the ToF selections chain, finally resulting in the total ToF efficiency.

First of all, the efficiency of the selection $\beta > 0$ is evaluated, which is expected to be flat and close to 1. Indeed, this is the case, except for the very low energy where some hadronic contamination is present: below ~ 300 MeV, the calorimeter is not as efficient in rejecting hadrons as at higher energies and the presence of hadrons in the initial sample is confirmed by a visual inspection of the rejected events. On the other hand, an unbiased sample of events can be selected at higher energies.

As mentioned in Sec. 3.3, the β measurements from the different ToF layers can
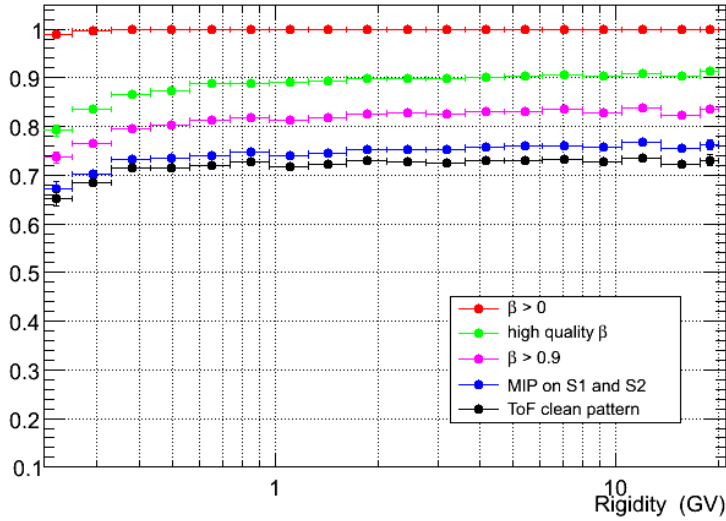
Figure (4.6)   *The Time of Flight selection efficiencies.*

be combined to obtain a final high quality β. The β definition adopted in this work requires a valid measure of the particle time of flight by all the S1-S3 combinations. Due to inefficiencies of single ToF layers, not all the triggering events satisfy this requirement, leading to an overall inefficiency as high as 10%. The energy dependence of the efficiency related to the quality of β is shown in green: it is flat above 0.6 MeV and decreases at lower energies. This shape does not depend on a correlation with the tracker system since the application of stricter conditions for the definition of tracker quality does not affect the result. The additional requirement of relativistic particles (selection $2, 3$ and 4) make the efficiency further decrease, uniformly in the whole energy range.

4.4.2   The trigger efficiency

The product of the trigger efficiency of the single paddles involved in each particular trigger configuration determines the PAMELA trigger efficiency. Ricciarini measured that the trigger efficiency is better than ~ 0.997 with an error of the order of 0.5×10^{-4}. Since the correction related to the trigger efficiency is much smaller than other effects described in this chapter, the trigger efficiency is omitted when calculating the total instrument efficiency.

4.5   The calorimeter efficiency

The calorimeter efficiency ϵ_{cal} was evaluated from a sample of electrons selected from flight and calculated as the fraction of events that fulfill the requirements used to derive the electron flux:

1. particle track inside a fiducial area (7 strips from the sides) on the first and last calorimeter planes,

2. calorimeter selections described in Sec. 3.6 for events with rigidity less than 0.5 GV,

3. $ncore > (240 \cdot rigidity - 50),$ for $rigidity <= 4.\, GV$

4. $ncore > (50 \cdot rigidity + 710),$ for $rigidity > 4.\, GV$.

The initial sample of data was constituted by the events selected as electrons after having applied all the selection cuts on the other PAMELA detectors, as implemented in the analysis. Despite the contamination from secondary particles is expected to be low in the sector of the negatively charged particles detected by PAMELA , and the contamination from antiprotons can be considered negligible, additional requirements are put to further clean the initial sample: a stricter cut on the mean energy released on the tracker planes below 0.4 GV and the exclusion of the South Atlantic Anomaly from the data set.
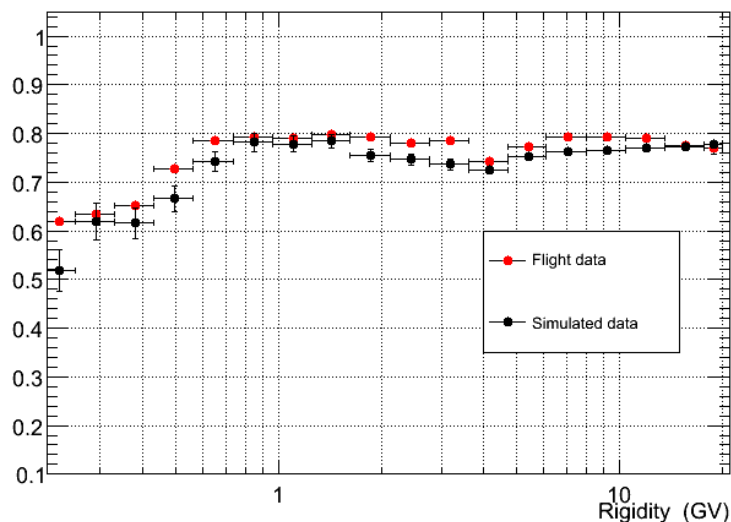
Figure (4.7)   *The efficiency of the calorimeter selections derived from flight data electrons, compared with the results from simulation.*

Fig. 4.7 shows, in black, the resulting rigidity dependence of ϵ_{cal}. It presents a shape almost flat in the whole energy range which decreases below ~ 0.5 GV due to the application of stricter requirements, that where developed to select positrons among the background of secondary pions. The decrease at about 4 GV is connected to the step-like dependence on rigidity of the calorimetric variable $ncore$, which is not perfectly traced by the selection cut.

For comparison, the result from simulation is also reported (red markers). The energy dependence is very similar and differences among flight and simulated data range from few per cent to less than 10%; consequently, a conservative error of 10% was associated to ϵ_{cal}.

Simulation has also confirmed that, in the energy range of interest, no differences are observable between the behavior of electrons and positrons in the PAMELA calorimeter: ϵ_{cal} does not show any dependence on the incident particle charge.

The stability in time of the calorimeter efficiency has also been checked and has been found to be stable, within the statistical error, from July 2006 to December 2008.

4.6 The total efficiency

Fig. 4.8 shows the combination of all the efficiencies of the PAMELA detectors. The plot does not include the trigger efficiency nor that of anti-counters, that have been measured to be close to 100%. The additional tracker selections $\epsilon_{trk}^{additional}$ are shown in blue, while the basic cut efficiency is convoluted with the instrument geometrical factor and not shown here. ϵ_{ToF} and ϵ_{calo} appear respectively in green and red.

The statistical error associated to each efficiency is better than per cent, increasing to $\sim 2\%$ at maximum close to the upper and lower edges of the energy range, where the number of events decreases due to the spectral shape and to the instrument acceptance respectively. More decisive for the final measure is the 10% systematic error associated to ϵ_{cal} and the statistical error associated to the calculated acceptance, which is less than per cent at the plateau but rises up to 8% in the lowest energy bin.

Since the different sets of electrons which have been used to derive the selection efficiencies were selected independently and no evidence of correlation between the sub-detectors under study was found in the analysis, we assume that it is possible to safely multiply the single efficiencies to obtain the total efficiency ϵ_{TOT} of Fig. 4.9.
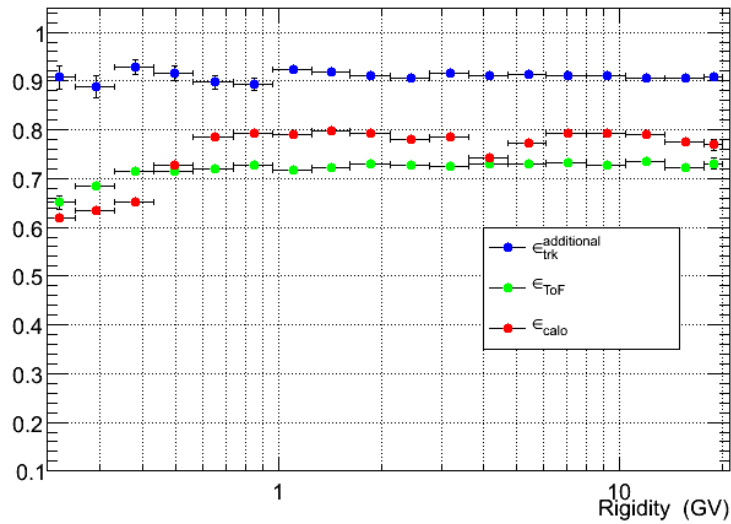
Figure (4.8) *Efficiencies of the single PAMELA sub detectors. The calorimeter and ToF efficiencies, ϵ_{cal} and ϵ_{ToF}, are derived from flight data selected during the whole time period (July 2006 - December 2008), while the efficiency of the additional tracker selections, $\epsilon_{trk}^{additional}$, is from simulation.*

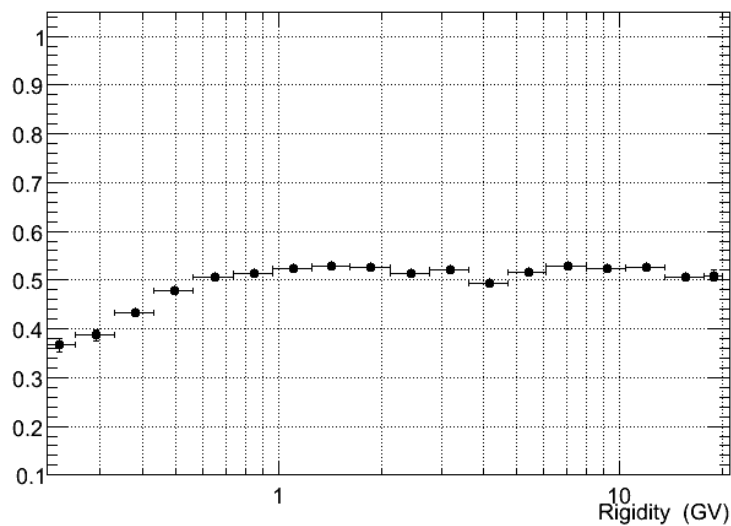**Figure (4.9)** *Total electron efficiency of the PAMELA instrument between 0.2 and 20.0 GV.*

Chapter 5

Positron fraction and fluxes

The corrections discussed in the previous chapters, necessary to obtain the final number of electrons and positrons detected by the PAMELA instrument, are applied here to derive the $e^+/(e^+ + e^-)$ ratio. Then, the further analysis steps that result in the measured electron spectrum are described.

5.1 Experimental results

The selections which have been presented in chapter 3 resulted in a number of e^+ and e^- detected in the energy range $0.2 - 3.0$ GV that has been reported in Tab. 3.4. In order to achieve the final result these numbers have to be corrected for the estimated residual contamination in the positron sample and compensated for the selection efficiencies, taking into account possible biases. These corrections have been discussed in detail in chapter 3 and 4.

5.1.1 The positron fraction

It seems reasonable to assume that the overall instrument response to the interaction of electrons and positrons is the same, but it has been shown in the previous chapter that some instrumental effects can be charge sign dependent; they have to be taken into account when deriving the positron fraction $e^+/(e^+ + e^-)$.
The residual pion and proton contamination and charge dependent instrumental effects have been taken into account. Moreover, to correct for energy losses in the instrument, an unfolding procedure that will be explained in the next section has been applied to e^+ and e^- data. Any difference among electrons and positrons in their

propagation at the top of the payload depends on their different energy spectrum. The uncertainty associated to the final positron fraction, due to this propagation, has been estimated to be equal to 3% and added as a symmetric systematic error. Tab. 5.1 reports the PAMELA positron fraction measured between 0.2 and 3.0 GeV, while in Fig. 5.1 the positron fraction is plotted as a function of energy.

$Energy\ range$ (GeV)	$positron\ fraction$ $\times 10^{-2}$
$0.2 - 0.35$	$12.05^{+0.60+0.64}_{-0.60-0.36}$
$0.35 - 0.5$	$12.23^{+0.42+0.43}_{-0.42-0.37}$
$0.5 - 0.7$	$11.54^{+0.30+0.40}_{-0.30-0.35}$
$0.7 - 0.9$	$10.24 \pm 0.24^{+0.32}_{-0.30}$
$0.9 - 1.1$	$9.25 \pm 0.22 \pm 0.28$
$1.1 - 1.3$	$8.66 \pm 0.21 \pm 0.26$
$1.3 - 1.5$	$8.39 \pm 0.22 \pm 0.25$
$1.5 - 1.7$	$7.51 \pm 0.21 \pm 0.23$
$1.7 - 2.0$	$7.05 \pm 0.18 \pm 0.21$
$2.0 - 2.3$	$6.60 \pm 0.19 \pm 0.20$
$2.3 - 2.6$	$6.10 \pm 0.20 \pm 0.18$
$2.6 - 3.0$	$6.04 \pm 0.21^{+0.21}_{-0.18}$

Table (5.1)   *The PAMELA positron fraction between 0.2-3.0 GeV. The number of positrons has been corrected for the estimated positive pion and proton residual contamination. Charge dependent instrumental effect have been taken into account and uncertainties related to the propagation at the top of the payload have been added as a systematic error. The statistical (first) and systematic (second) errors are reported.*

5.1.2   The electron spectrum

As anticipated in chapter 3, the calorimetric selection cuts used to obtain the number of electrons and positrons can be relaxed, and extended to higher energies, to derive an electron flux. This is done only above 0.5 GV, while the selections are kept unchanged at lower energies. As it was shown, the negative pion contamination on the electron sample can be considered totally negligible. The efficiencies of these selections have been evaluated in Sec. 4.5.

In order to derive the flux $\Phi_{e^-}(E)$, it is necessary to opportunely correct the number
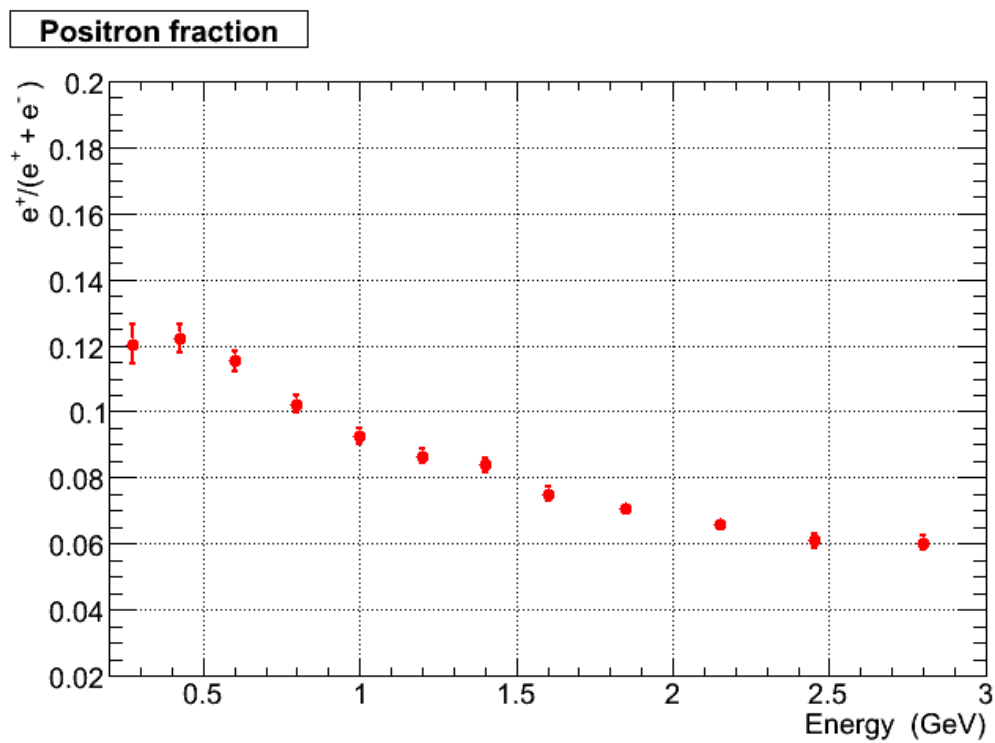
Figure (5.1)   *Positron fraction measured by the PAMELA experiment in the energy range 0.2-3.0 GeV as a function of the energy at the top pf the payload. The residual pion and proton contamination in the positron sample and charge dependent instrumental effects have been taken into account.*

of detected particles, N, for the selection efficiency and the instrument acceptance, ϵG; the resulting number will be divided by the instrument livetime, T, and the bin width, ΔE. Moreover, the number of electrons has to be corrected for energy losses in the payload to derive their number at the top of the payload and the yield of secondary electrons produced in interaction of primaries with the instrument has to be estimated. All the mentioned effects are energy dependent and the related corrections will be described more in detail in the following paragraphs. Simulation has shown that the number of secondary electrons surviving the selection chain is negligible.

The flux $\Phi_{e^-}(E)$ is defined in units of $(cm^2 \; s \; sr \; GeV)^{-1}$, according to the relation:

$$\Phi_{e^-}(E) = \frac{N}{T \times \epsilon G \times \Delta E} \qquad (5.1)$$

Efficiency correction. The instrument acceptance and the selection efficiencies are both rigidity dependent, as evaluated in the previous chapter. Correcting the number of electrons by evaluating ϵG in the center of each bin would give a biased result. The adopted technique makes use of a mean efficiency that is calculated for each bin in the following way:

$$\bar{\epsilon} = \frac{\int \epsilon(x) J(x) dx}{\int J(x) dx} \qquad (5.2)$$

where x is the particle rigidity. $J(x)$ is the flux under study, which obviously depends on efficiencies, thus an iterative procedure is adopted: as a first step the mean efficiencies $\bar{\epsilon}$ are evaluated by the distribution $\epsilon(x)$ and the raw electron spectrum, using a linear interpolation to obtain the value at a given rigidity. The derived mean efficiency can be used to calculate a second spectrum, which we can use for the following step. The iterative procedure is applied only below 0.5 GV, where the total efficiency presents the more significative variations, and is continued until the difference between the obtained spectrum and the spectrum derived with the previous iteration is less than 1%.

Instrument livetime. The experiment livetime is defined as the time the instrument is operational and ready to accept a new trigger. The trigger board stores for each event the livetime elapsed after the preceding acquired event. In order to obtain a flux, by definition, the number of events has to be divided by the instrument livetime; for energies below ~ 15 GV it is not possible to use the total instrument livetime but it is necessary to consider the time spent by the apparatus

at orbital regions characterized by cut-off rigidities lower than the particle energy: once fixed the particle rigidity, different points along the PAMELA orbit are not equivalent since the lower is the particle rigidity the shorter the time available to detect it. Thus, generally, the geomagnetic cut-off poses serious limits to the lower detectable rigidity by satellite and balloon borne experiments. In the PAMELA case, thanks to the high inclination of its orbit, cut-off rigidities of the order of few MeV can be reached and explored for a non negligible amount of time. Instead, the real low energy limit is posed by the acceptance which, as shown in chapter 4, decreases below ~ 300 MeV, due to the bending of charged particles in the instrument magnetic field that makes them go out of acceptance. The spatial distribution of the selected electrons and positrons, plotted as the latitude and longitude of the satellite when the event was collected, is shown in Fig. 5.2. The two panels well illustrate how the orbital region suitable for the measures reduces with lowering the detected particle rigidity, due to the cut-off selection. No anisotropies are evident and the electron and positron distributions match well.
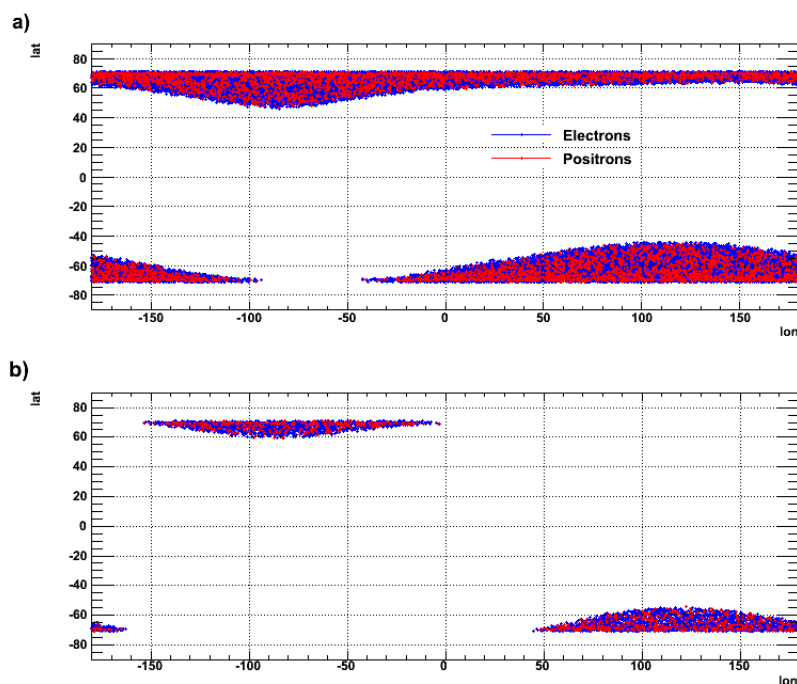
Figure (5.2)   *Region of the PAMELA orbit where positive and negative particles with rigidity between 1.0 and 1.5 GV (upper panel) and between 0.2 GV and 0.3 GV (lower panel) are detected.*

The fraction of livetime spent by PAMELA in orbital regions below a certain cut-off is shown in Fig. 5.3. PAMELA spends less than 40% of its time below 3 GV and in

particular less than 15% below 500 MV.
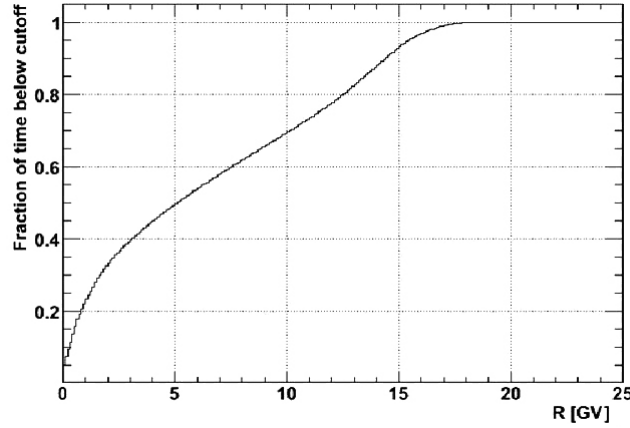
Figure (5.3)   *Fraction of livetime spent by* PAMELA *in regions characterized by cut-off values lower than* R.

Energy losses in the instrument.   The tracker can measure the particle rigidity after it has passed through the equivalent of $\sim 3 \ g/cm^2$ of material (dome, S1 and S2 scintillators and their support structures), thus losing part of its energy. There exist in literature a number of different methods to compensate for such an energy loss, in the e^+ and e^- case mostly due to radiation, and to reconstruct the particle spectrum at the top of payload.

In this thesis we use the iterative unfolding method based on the Bayes' theorem proposed by D'Agostini, G. (1995). Thanks to this procedure it is possible to determine the best estimate of the *true* distribution from the measured one, which is smeared because of experimental effects. Namely, the effects that we can correct for are related to energy losses and tracker resolution.

The Bayes' theorem is stated in terms of several independent *causes* $(C_i, i = 1, 2, ..., n_C)$, in our case the passage of particles of given rigidities through the apparatus, which can produce an observable response in the detector - measured rigidities - that is the *effects* $(E_j, j = 1, 2, ..., n_E)$. It it usually presented in the form:

$$P(C_i|E_j) = \frac{P(E_j|C_i)P_0(C_i)}{\sum_{l=1}^{n_C} P(E_j|C_l)P_0(C_l)}. \tag{5.3}$$

The formula links the probability $P(C_i|E_j)$ that the single observed event E_j has been due to the cause C_i, to the probability $P(E_j|C_i)$ that the cause ith produces the jth effect, times the probability of the cause $P_0(C_i)$.

If we observe, in the jth energy bin, $n(E_j)$ events, the best estimate of the expected number of events assignable to each of the cause is

$$\hat{n}(C_i) = \frac{1}{\epsilon_i} \sum_{j=1}^{n_E} n(E_j) P(C_i|E_j), \quad \epsilon_i \neq 0 \tag{5.4}$$

where ϵ_i is the efficiency of detecting the cause C_i in any of the observed effects and is defined as follows:

$$\epsilon_i = \sum_{j=1}^{n_E} P(E_j|C_i). \tag{5.5}$$

Simulation suggests to use iteratively formula (5.4) in order to obtain the final $\hat{P}(C_i)$ as close as possible to the true one, being $P(\hat{C}_i) = n(C_i)/\sum_{i=1}^{n_C} \hat{n}(C_i)$. The probabilities $P(E_j|C_i)$ can be estimated with Monte Carlo methods and constitute the elements of the *smearing matrix* **S**, while an assumption has to be done about the initial probability $P_0(C)$. The iteration goes through the following steps:

1. choose the initial distribution $P_0(C)$ and evaluate the initial expected number of events $n_0(C_i) = P_0(C_i)N_{obs}$, where N_{obs} is the number of experimental observations,

2. calculate $\hat{n}(C)$ and $\hat{P}(C)$,

3. make a χ^2 comparison between $\hat{n}(C)$ and $n_0(C)$,

4. replace $P_0(C_i)$ by $\hat{P}(C)$ and $n_0(C)$ by $\hat{n}(C)$ and start again.

The iteration is stopped when the value of χ^2 is less than a fixed value.
This method presents many advantages respect to other approachesand it can be succesfully applied to data if a reliable choice of the smearing matrix is done and if the Monte Carlo properly simulates the particle energy losses in the instrument (Percossi, G., 2005). In order to prove this, a crosscheck with real data has been done. The electron spectrum measured by the PAMELA tracker has been compared with what is obtained by a calorimetric measure of the particle energy. The calorimeter can measure the total energy of the incident lepton and reconstruct, with good approximation, the particle initial energy. The same comparison has been done using the simulation. The differences between the spectrum reconstructed by the tracker and the calorimeter from real and simulated data are compared, resulting in good agreement. Thus, we can conclude that the simulation well reproduces energy losses in the instrument and can be used for the deconvolution.
A set of simulated data has been generated in the energy range $(0.025 - 20.0)$ GV and primary triggering particles which fulfill the basic tracker criteria have been selected to build the smearing matrix. Their energy distribution is flat below 1 GeV
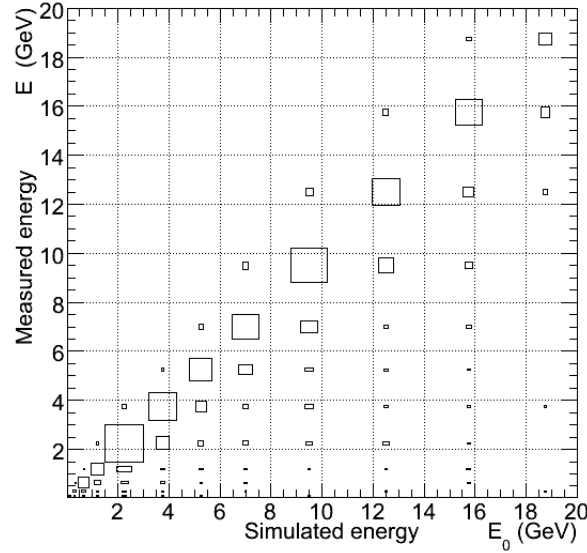
Figure (5.4)   *Smearing matrix. The true and the measured energies are plotted in abscissa and ordinate respectively.*
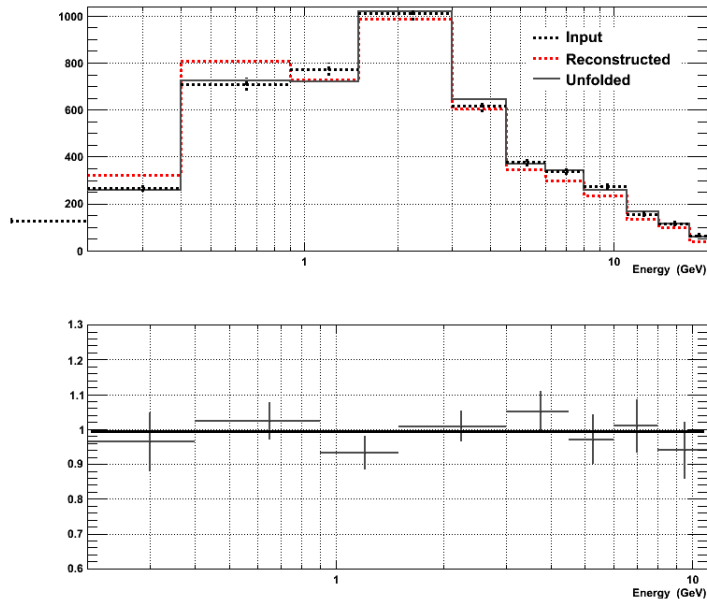
Figure (5.5)   *In order to evaluate the performance of the unfolding algorithm is has been executed a test on simulated data. The result of the procedure is shown in the top panel. The lower panel represents the unfolded to true distribution ratio (see text).*

and a power law above[1]. Fig. 5.4 shows the obtained smearing matrix, whose elements represent the probability for an electron of energy E_0 to be reconstructed with energy E.

Before using the unfolding method on the PAMELA data it is necessary to prove that the algorithm is working properly. A performance test is accomplished in the following way: two independent sets of simulated data are prepared, one is necessary to build the smearing matrix S while the other is used to create a known *true* distribution distribution to be unfolded. If the algorithm works correctly, it converges to an unfolded distribution that is identical to the simulated (*true*) one. We assume a power law distribution as initial probability:

$$P_0(C_i) = KC_i^{-\gamma} \tag{5.6}$$

where K can be found imposing $\sum_{i=1}^{n_C} P_0(C_i) = 1$. After each step we perform a smoothing of the unfolding result, by a polynomial fit of 3rd degree, before using it as input for the following step.

The result after a number of iterations corresponding to $\chi^2 < 0.001$ is shown in Fig. 5.5 (top panel). It is possible to see how the *true* distribution (black dotted line) would appear after the measure (red dotted line) and how the result of the unfolding (grey line) is in agreement with the *true* one. The ratio between the unfolded distribution and the *true* one, fitted by a constant, is shown in Fig. 5.5 (bottom panel), and gives the feeling of the goodness of the agreement.

$$f(x_0) = \frac{1}{x_2 - x_1} \int_{x_1}^{x_2} f(x)dx \tag{5.7}$$

where $x_{1,2}$ are the bin edges and $f(x) = Ax^{-\gamma}$ is the power law spectrum. The described approach resulted in the electron spectrum that is shown in Fig. 5.6 and reported in Tab. 5.2, refering to data collected in 2006.

Data points are centered, in each bin above 1 GeV, according to a technique developed by D. Lafferty and R. Wyatt (1995). Each value (x_0) is determined as the abscissa value at which the measured spectrum is equal to the expectation value of the 'true' spectrum. This can be expressed as:

Rigidity range (GV)	*E* (GeV)	Φ_{e^-} $(GeV\ cm^2\ s\ sr)^{-1}$
$0.2 - 0.3$	0.25	$(2.20 \pm 0.18 \pm 0.06) \cdot 10^{-3}$
$0.3 - 0.4$	0.35	$(2.90 \pm 0.25 \pm 0.09) \cdot 10^{-3}$
$0.4 - 0.5$	0.45	$(2.77 \pm 0.23 \pm 0.08) \cdot 10^{-3}$
$0.5 - 0.6$	0.55	$(2.68 \pm 0.23 \pm 0.08) \cdot 10^{-3}$
$0.6 - 0.8$	0.7	$(2.30 \pm 0.14 \pm 0.07) \cdot 10^{-3}$
$0.8 - 1.0$	0.9	$(1.95 \pm 0.09 \pm 0.06) \cdot 10^{-3}$
$1.0 - 1.3$	1.15	$(1.53 \pm 0.06 \pm 0.05) \cdot 10^{-3}$
$1.3 - 2.0$	1.65	$(1.04 \pm 0.04 \pm 0.03) \cdot 10^{-3}$
$2.0 - 3.0$	2.5	$(5.13 \pm 0.20 \pm 0.15) \cdot 10^{-4}$
$3.0 - 4.0$	3.43	$(2.35 \pm 0.10 \pm 0.07) \cdot 10^{-4}$
$4.0 - 5.0$	4.44	$(1.22 \pm 0.05 \pm 0.04) \cdot 10^{-4}$
$5.0 - 6.0$	5.45	$(7.4 \pm 0.4 \pm 0.2) \cdot 10^{-5}$
$6.0 - 8.0$	6.86	$(3.25 \pm 0.21 \pm 0.1) \cdot 10^{-5}$
$8.0 - 10.0$	8.89	$(1.48 \pm 0.11 \pm 0.04) \cdot 10^{-5}$
$10.0 - 20.0$	13.33	$(3.37 \pm 0.26 \pm 0.10) \cdot 10^{-6}$

Table (5.2) *This table summarizes the electron flux measured from 0.2 to 20 GeV in 2006. The statistical (first) and systematical (second) errors are reported.*
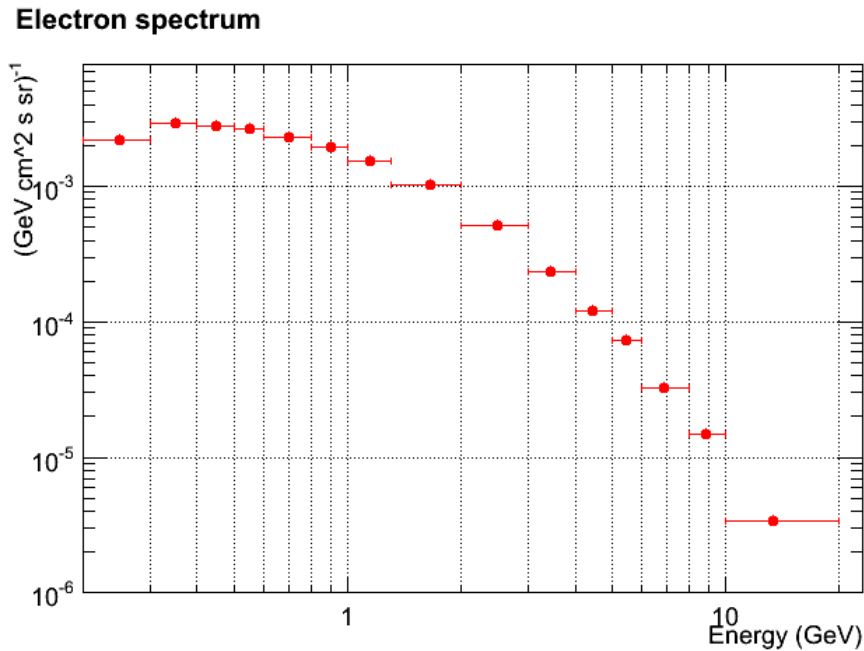
Figure (5.6) *Electron flux as measured by the PAMELA experiment in the energy range $0.2 - 20$ GeV.*

5.2 Experimental and theoretical comparison

5.2.1 The electron spectrum

Fig. 5.7 shows the PAMELA electron flux together with other experimental measures obtained in the last decades. All these spectra present a minimum detected energy below few GeV and are obtained with experiments able to distinguish the charge of the particles, separating electrons from positrons using magnets. Besides PAMELA , only AMS (Alcaraz *et al.*, 2000) collected data at altitudes higher than ~ 300 km, where the residual atmosphere does not constitute an issue to deal with. The other, balloon borne, experiments usually fly at about 4.0 g/cm^2 and have to apply corrections to take into account the contamination by secondary electrons that are produced by conversion of bremsstrahlung photons from primaries interactions. There is not a standard recipe to correctly evaluate the spectra at the top of the atmosphere: as an example for the CAPRICE94 (Boezio *et al.*, 2000) experiment the e^- spectra were extrapolated by solving iteratively the cascade equations that describe the propagation of e^-, e^+ and γs resulting from bremsstrahlung of

---

[1] the spectral index used is -2.0 below 5.0 GeV and -3.0 above, a compromise between good statistics in each bin and a non uniform filling.

Electron spectrum
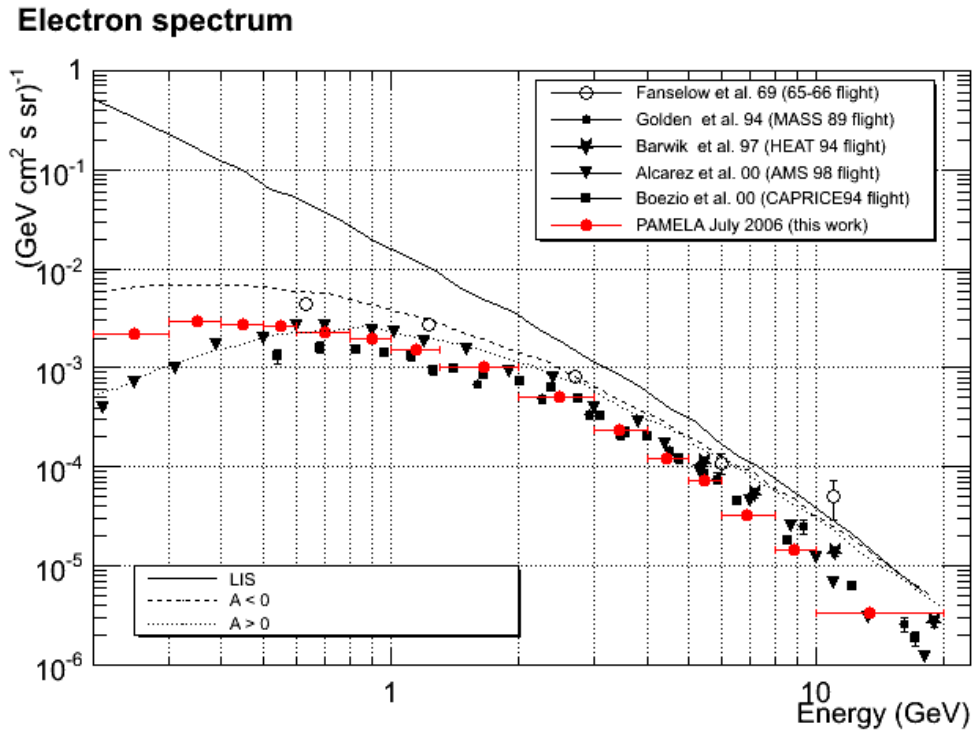
Figure (5.7)   *Electron flux as measured by the PAMELA experiment in the energy range $0.2 - 20$ GeV in 2006, together with electron data provided by experiments operating in the last decades (Golden and et al., 1994; Barwick et al., 1998; Boezio et al., 2000; Alcaraz et al., 2000) and the only available measure of electron spectrum in A- epoch (Fanselow et al., 1969).   The solid line represents the electron local interstellar spectrum as calculated by Langner et al. (2001), while the dashed and dotted lines result by the work of Langner and Potgieter (2004).*
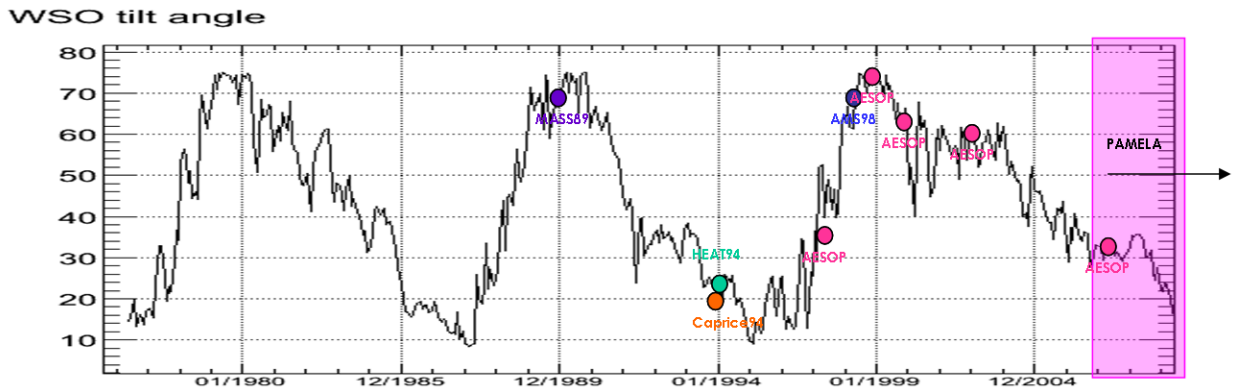
Figure (5.8) *The classic tilt angle measured at the Wilcox Solar Observatory and the period of data taking of experiments mentioned for a comparison with the PAMELA electron spectrum and positron fraction.*

the electron component; for the HEAT (Barwick *et al.*, 1998) data the atmospheric contribution was evaluated by Monte Carlo and cross-checked by comparison with an empirical estimate from flight data. The uncertainty related to this correction can be as high as $\sim 5\%$ and is not present in the PAMELA data.

As it can be seen in the figure, the measurements differ as much as a factor of about 2 at high energy and PAMELA is in line with the existing measurement. At low energy a comparison is more difficult because of the effect of the solar modulation. All the experimental spectra are distorted at energies lower than few GeV respect to the unmodulated local interstellar spectrum that is represented in figure by the solid line. The CR electron local interstellar spectrum has been calculated by Langner *et al.* (2001) on the basis of sophisticated models of propagation of CRs in the Galaxy and on comparison with a variety of data sets (radio synchrotron indices and γ-rays).

The only existing data collected during an A- solar minimum are those by Fanselow *et al.* (1969); only their data points that surely not affected by a reentrant albedo component are reported in figure. Fig. 5.8 shows how the experiments which have provided the existent e^+ and e^- data are distributed in time along the recent solar cycles. Respect to the AMS-01 spectrum (June 1998) the PAMELA data at low energy are higher, as expected for an experiment performed during a period of lower solar modulation. If compared with the CAPRICE94 results, the PAMELA data are higher as well, despite the solar activity level at the time of the CAPRICE flight was low as the current one, or even lower according to the data of the WSO (WSO website). However this would not contradict the drift model expectations: the dotted and dashed lines in figure represent theoretical calculations in case of A+ and A- so-

lar polarity respectively, as derived by Langner and Potgieter (2004) at 1 AU. As reviewed in section 1.4, drift models predict a clear charge sign dependence for the heliospheric modulation of cosmic ray charged particles; as a consequence, the electron spectral shape below ~ 1 GeV is calculated to be flatter during A- epochs than during A+.

Moreover, thanks to the high statistics collected by the PAMELA experiment, it
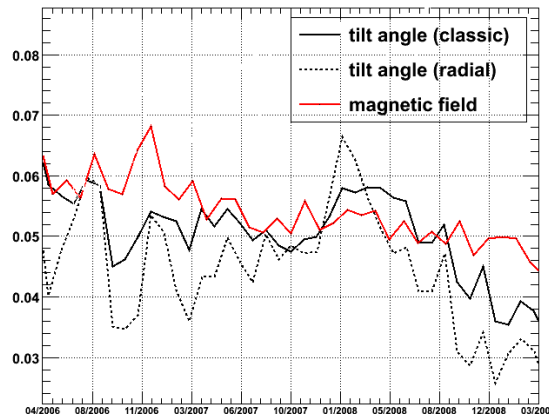
Figure (5.9)   *The tilt angle and the value of the solar magnetic field monitored by the WSO observatory and the OMNI spacecraft during the period of the PAMELA data taking.*

was possible to derive the electron energy spectrum at different times during more than two years of data taking and thus to monitor in time its evolution. The time dependence of the instrument efficiencies has been taken into account, as described in chapter 4, and the resulting spectra are plotted in Fig. 5.10 for two time periods. In red the differential energy spectrum measured between September and November 2006 is shown ,while the blue one refers to the period from October to December 2007. The spectral shape and intensity remains stable in the higher energy part of the electron spectrum, while at low energy it is observable a significant increase from 2006 to 2007. This would be in line with the expectation in case of a decreasing solar modulation.

The current solar minimum is one of the deepest in almost a century. In terms of sunspots, the number of spotless days during a typical solar minimum is 485; since 2004 we had 772 spotless days, and no sunspots have been observed for the 73% of 2008 and 87% of 2009. Moreover data from the WSO observatory and the OMNI spacecraft, that are reported in Fig. 5.9 suggest that the Sun has been very stable during the period in which the PAMELA data analyzed in this work have been col-

lected. The solid lines represent the tilt angle calculated using two potential field models applied to photospheric magnetic field observations from WSO; the dotted line shows the evolution of the average magnetic field magnitude measured at 1 AU in the ecliptic (OMNI M website); the data have been normalized in order to make the reading easier. Nevertless, it takes time (about one year) for the conditions at the Sun to propagate and influence the global heliosphere. Thus, despite the stable situation observed at the Sun, the time dependence of the low energy electron intensity at Earth could be seen as the consequence of the relaxation of the whole heliospheric condition. An analogous time behavior of the spectral shape has been observed in the PAMELA proton measurements. This data can be fruitfully used to
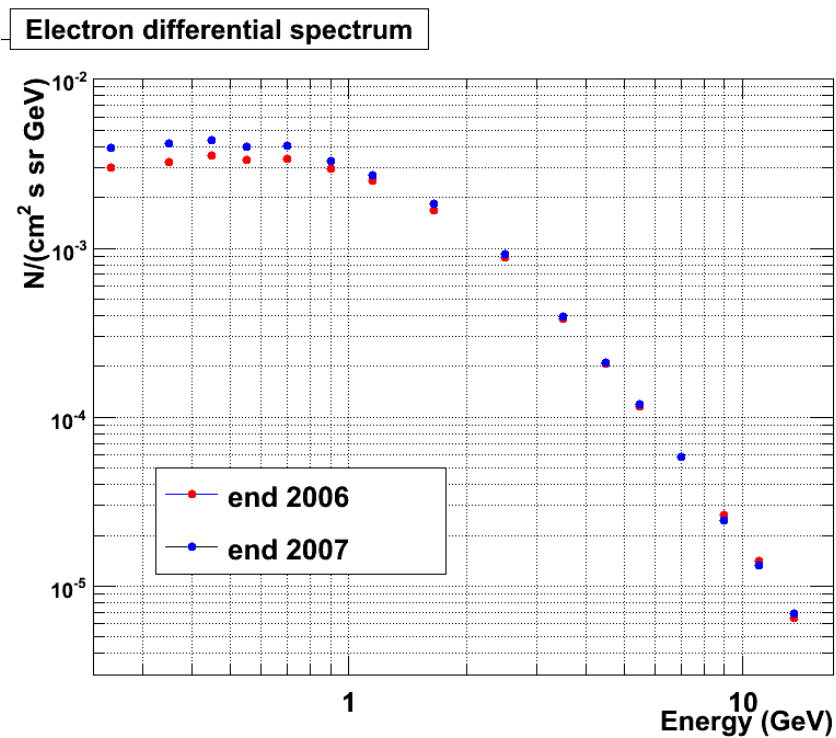
Figure (5.10) *The electron flux as measured by the PAMELA experiment in the energy range $0.2 - 20.$ GeV. In red, data from September to November 2006, in blue those from October to December 2007.*

fine tune the parameters of the solar modulation theoretical models: the modulation of cosmic ray electrons, in particular, provides a useful tool to study the diffusion tensor related to the heliospheric modulation. In fact, electron modulation responds directly to the assumed energy dependence of the diffusion coefficient below ~ 0.5 GeV, in contrast to protons which experience large adiabatic energy losses below this energy. As a result, conclusions can be made about the appropriate diffusion

coefficients.

Additional information about solar modulation can be obtained by comparing particles characterized by a different sign of charge.

5.2.2   The positron fraction

As we have seen, it is experimentally more straightforward to derive the positron fraction than the absolute particle flux, since one can reliably assume the efficiencies to be the same for e^- and e^+, so that they do not appear in the calculations. Thus more experimental data exist. In Fig. 5.11 the PAMELA $e^+/(e^+ + e^-)$ data measured between July 2006 and December 2008 are reported in comparison with the results from previous observations and some theoretical predictions. Most of the
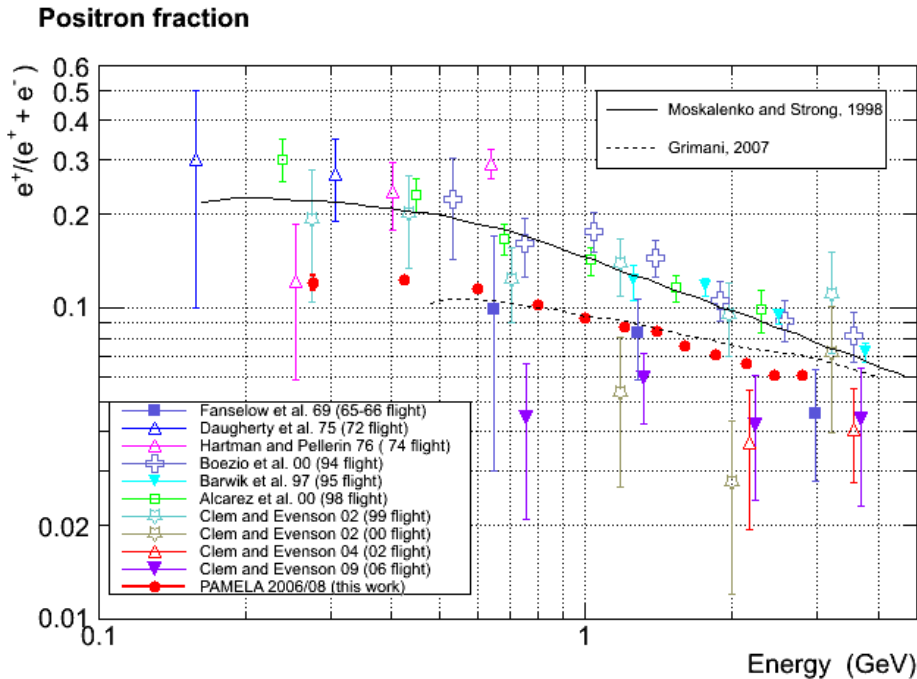
Figure (5.11)   *The positron fraction measured by the PAMELA instrument compared to previous available data.   The solid line represent the expectation of a model wich does not include drift (Moskalenko and Strong, 1998), while the dashed line takes into account the charge dependent solar modulation (Grimani, 2009).*

existing data refer to A+ epochs (open markers) and there are only two experiments that have been taking data in the same PAMELA polarity epoch (solid markers):

the balloon borne AESOP(Clem and Evenson, 2009) instrument has been in flight for 5 days since 2 June 2006 and it has provided a positron fraction measurement in the energy range $0.6 - 4.5$ GeV, while the first data taken in A- polarity date back to 1965-66 (Fanselow *et al.*, 1969). Considering the size of the error bars, the **PAMELA** results are in agreement with these data within 2σ, while they are significantly and systematically lower than all those from flights performed in A+ polarity.

The solid line in figure is the prediction from Moskalenko and Strong (1998) that does not take into account the effect of the charge dependent solar modulation. This is, instead, done by Grimani (2009) (dashed line) who infered the role of solar modulation and, in particular, drift from experimental data gathered by the same experiment in different conditions of solar modulation and solar polarity, on the incipit of a force field approximation model. The comparison with the results of models that, instead, numerically solve the transport equation of charged particles in the heliosphere will be shown in the following.

If we calculate the positron abundance at ~ 1.25 GeV (energy bin 1.09 - 1.5 GeV), we can plot the **PAMELA** results together with other measurements in chronological order, as shown in Fig. 5.12. As already observed by (Clem and Evenson, 2009), the plot reveals a significant decrease between 1999 and 2000 from a level that remained relatively constant during the previous, opposite, magnetic polarity cycle. The black line represents a model developed by Clem *et al.* (1996); it is based on the leaky box model and on the observed systematic difference in the correlation between the electron flux measured in space by the ICE experiment and the neutron monitor observations. The most recent AESOP measurements run in July 2006 indicate that the predicted magnitude of the change may be too large, and the **PAMELA** data presented in this work strongly support this as well. New analysis are currently ongoing to understand this difference and seem to be promising (Pei C., 2009).

A different modeling approach is followed by Langner and Potgieter (2004). In order to compare the data with their calculation it is worthwhile to put them in terms of e^-/e^+ ratios. Fig. 5.13 shows the predicted e^-/e^+ ratio for solar minimum ($\alpha = 10°$) both for A+ and A- polarity epochs. The experimental data follows the predicted slope at high energy, while in the lower part of the explored energy range some difference is evident and has to be understood.

The **PAMELA** results can be used to fine tune the model and have a better understanding of the role assumed by their parameters. In particular, during solar minimum the drift effects are at their largest respect to the other mechanisms that define the transport of charged particles in the heliosphere, thus, the **PAMELA** data are ideal for this scope. Moreover, the investigation of the leptonic channel is par-
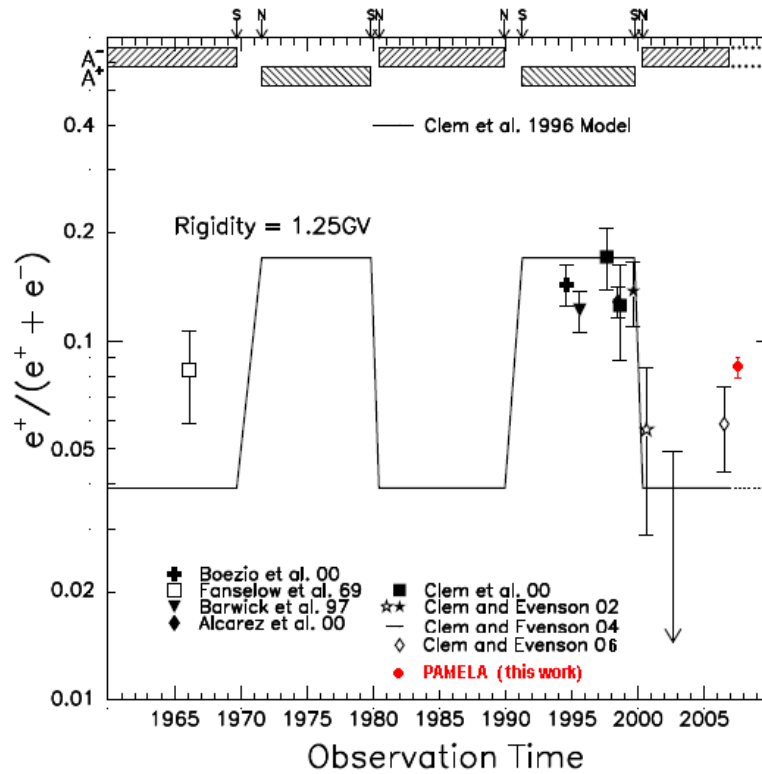
Figure (5.12)   *The time profile of the positron fraction observations as reported in Clem and Evenson (2009). Solid symbols show data collected in A+ epochs while the open symbols refer to data collected in A- polarity state. The PAMELA data, averaged in the time period spanning from July 2006 to December 2008 are in red. The polarity phase is indicated by the shaded rectangles in the topmost part of the figure while the black line represent the prediction from Clem et al. (1996).*

ticularly promising: since electrons and nuclei have greatly different charge/mass ratios, the relation of velocity and magnetic rigidity is very different for these two particle species; thus, the study of the behavior of cosmic ray positrons, relative to electrons (which have identical relationships between velocity and rigidity), has the merit to separate effects due to charge sign from those arising in velocity differences for the same particle rigidity.

In the next section the PAMELA e^-/e^+ measurements are compared with the data from the Ulysses spacecraft, in a first attempt to measure the electrons latitudinal gradients. This preliminary work is in part the basis of a future collaboration.
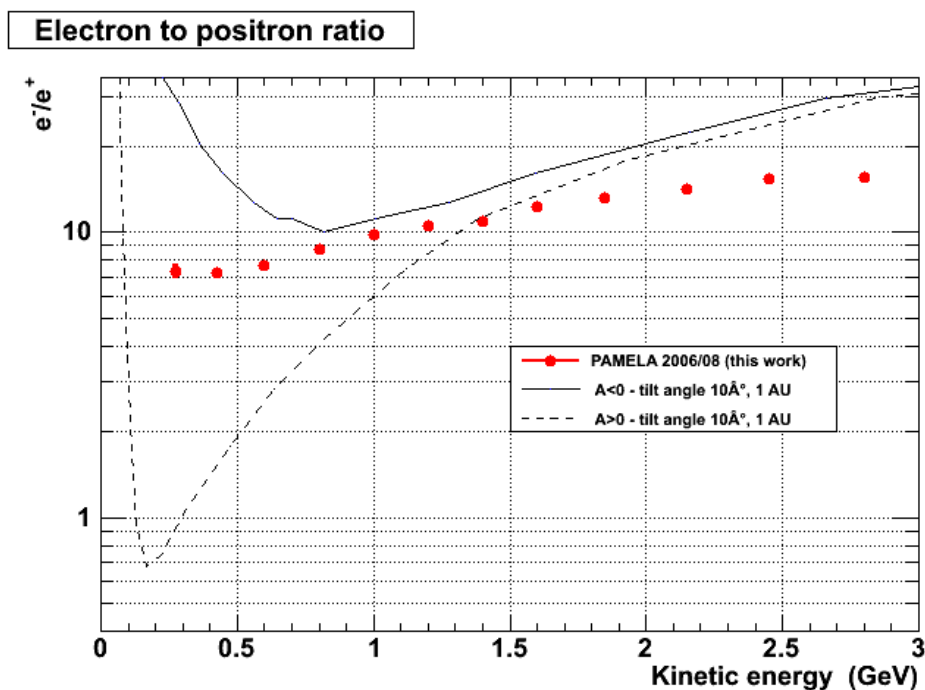
Figure (5.13) *e^-/e^+ ratio from PAMELA data compared with the results of drift models.*

5.2.3 Comparison with the Ulysses data - a first approach

The Ulysses spacecraft was launched on October 6, 1990, and placed in February 1992 into a trajectory inclined by $80.2°$ with respect to the ecliptic plane by a swing-by manuver at Jupiter. It was turned off at the end of May 2009 after 18 years and 8 months of successful exploration of the heliosphere, being up to now the only probe of the heliospheric high latitudes. Measurements of the charged particle distribution provided by Ulysses can give information about the spatial variation of their

intensity along its orbit. We will refer to these variations as to latitudinal and radial gradients.

Of special interest is the rigidity dependence of the latitudinal gradient in the range from below 1 GV to several GV. During the 1990s, Ulysses performed a so-called fast latitude scan: it reached its highest heliographic latitude of $80.2°$ south in September 1994, then, within one year the spacecraft scanned the region from highest southern to northern latitudes and was at $80.2°$ north in August 1995. During that period it was possible to determine the rigidity dependence of gradients for protons and He using the IMP 8 spacecraft as a baseline at Earth. The fast latitude scans have since then repeated from 2000 to 2001 and 2007 to 2008 (see Fig. 5.14 for an illustration of the third Ulysses orbit). The third fast latitude scan occurred during the declining phase of solar cycle 23, when the solar activity was comparable to that of the first latitude scan, but the Sun magnetic polarity was reversed. The effects of drifts are expected to change the spatial gradients and one might expect to compare the behavior of electrons in this phase with that of protons in A+. The IMP 8 spacecraft was lost in 2006. Later on, the spatial gradients have been measured during the following fast latitude scans for protons and electrons, but the measurements utilized carbon from ACE as a baseline close to Earth instead of p/He, or were based on Ulysses data (e/p) solely (see Heber *et al.*, 2008, and references therein). Now, PAMELA can represent a suitable baseline at 1 AU. First results from the Ulysses-PAMELA combined data are reported in the following.
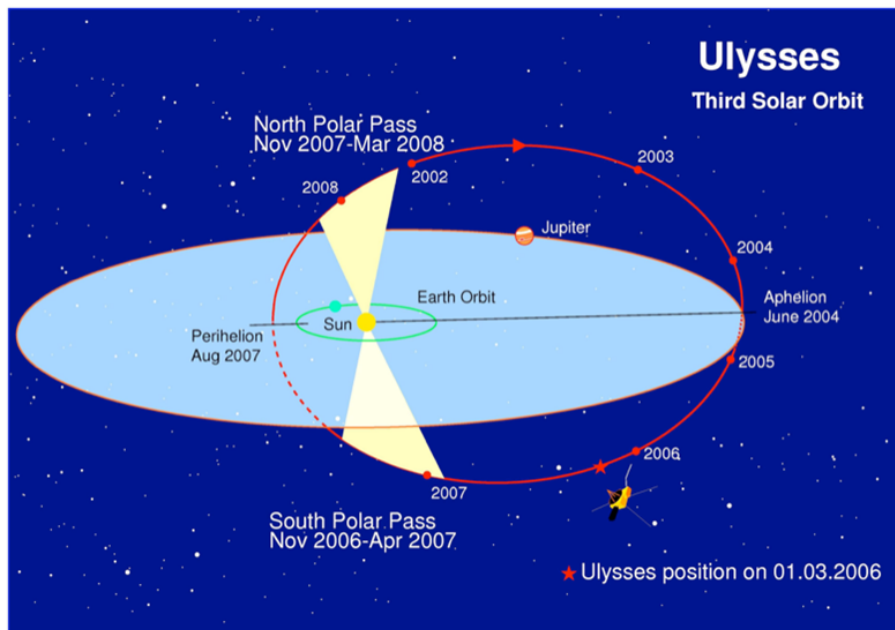
Figure (5.14)   *Illustration of the Ulysses orbit together with the of the Earth.*
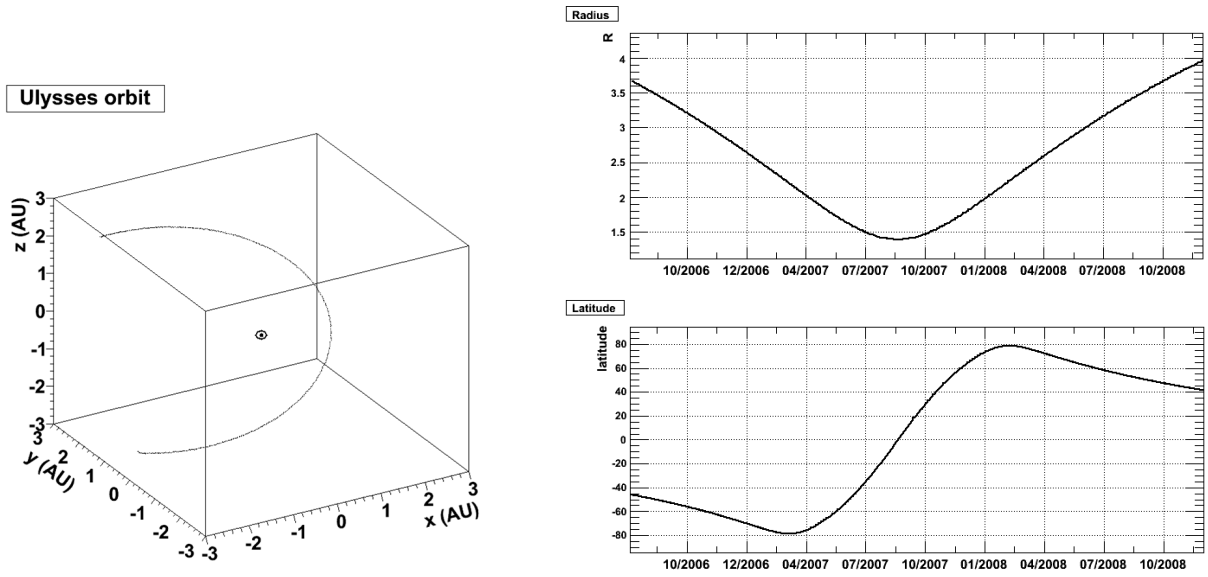
Figure (5.15) *Left panel: The Ulysses trajectory during the time in which the data comparison with the PAMELA experiment is possible. The Sun positio (point) is also reported. In July 2006 Ulysses was in the south heliospheric hemisphere at 3.7 AU and $\sim 55°$, going to the highest northern latitudes, concluding its third fast latitude scan in 2008. Right panel: The radial (top) and latitudinal (bottom) variation along the Ulysses orbit. The ecliptic crossing happened at a distance of about 1.4 AU in August 2007 and the closest approach was at about 1.39 AU and 7° North.*

Along the Ulysses orbit, fortunately, radial and latitudinal changes do not occurr in phase (see Fig. 5.15), then there is a possibility to disentangle the two components and measure both the effects. In this work we focus on the latitudinal component. We define the radial and latitudinal gradients, respectively G_R and G_θ, according to the following relation:

$$I_{ULYSSES} = I_{PAMELA}e^{G_R R}e^{G_\theta \theta} \tag{5.8}$$

where R and θ are the radial distance and the absolute value of the helio-latitude respectively, while $I_{ULYSSES} = I(t, R, \theta)$ is the intensity at the Ulysses position and $I_{PAMELA} = I(t, R = 0, \theta = 0)$ the intensity at the position of PAMELA . Under a series of assumption, it is possible to measure the latitudinal gradients of electrons[2] by comparing the $(e^+ + e^-)/p$ ratio at Ulysses site and the PAMELA

---

[2]Namely $(e^+ + e^-)$.

$(e^+ + e^-)/e^+$ at 1 AU. For simplicity we will refer to the measured quantities by the two experiments as to e/p ratio. The data have been compared from July 2006 and December 2008, applying a normalization factor obtained by comparing the data where the two instruments were at the same heliolatitude, in August 2007. The top panel of Fig. 5.16 shows the results from both the experiments in rigidity intervals characterized by similar mean rigidity (~ 2.5 GV), as a function of time. The bottom panel reports the Ulysses to **PAMELA** data ratio[3]. The measures have been averaged in time each 52 days for the Ulysses case and twice the time for the **PAMELA** data, and the energy range has been choosen to be:

ULYSSES: $(0.9 - 4.0)$ GV[4] .

PAMELA : $(0.9 - 3.0)$ GV.

The quality of the comparison can be enhanced by a fine tuning of the rigidity ranges on the basis of the single instrument response. The following statements have been assumed to be valid:

1. $(e^+ + e^-)/e^+$ should vary as $(e^+ + e^-)/p$.

2. The radial gradients are the same for all the species.

3. No latitudinal gradients for protons.

As mentioned, the intensity measured by Ulysses $I_{ULYSSES}$ is influenced not only by spatial but also temporal variations: thus, it is essential to know the intensity changes for a stationary observer in the heliosphere in order to separate time- and space-related effects. The first among the above conditions guarantees that **PAMELA** can be such a baseline at 1 AU and that it is possible to succesfully compare $(e^+ + e^-)/e^+$ with $(e^+ + e^-)/p$. Assumption 2) ensures that the ratio variations along the Ulysses orbit depend only on latitude. This is reasonable according to the work of Gieseler *et al.* (2008) and Clem *et al.* (2002), who found that electron radial gradients are nearly the same as the proton ones. The third hypothesis makes the variation only dependent on the electron $(e^+ + e^-)$ latitudinal gradients. Under this assumptions we can write:

$$\ln\left(\frac{I(t, R, \theta)}{I_{PAMELA}}\right) = G_\theta \theta \tag{5.9}$$

---

[3]The Kiel Electron Telescope (KET) aboard Ulysses measures protons and helium nuclei in the energy range from 6 MeV/nucleon to above 2 GeV/nucleon and electrons in the energy range from 3 MeV to a few GeV using two silicon detectors, an aerogel Cherenkov detector and PBF2-calorimeter.

[4]The analyzed data channel is E300. For the estimation of the corresponding mean energy and the proton background subtraction (see the work of Rastoin *et al.*, 1996).

Then, gradients would emerge as deviations from 0. Eq. 5.9 results in the plot in Fig. 5.17. The different size of the x axis error bars depends on the geometry of the Ulysses trajectory. The result of a linear fit provides:

$$G_\theta = (0.15 \pm 0.04)\%/degree \tag{5.10}$$

This result is consistent with that previously obtained for electrons in the same fast latitude scan, estimated by the Ulysses data solely ($G_\theta = (0.2 \pm 0.05)\%/degree$) and with that of protons in A+ polarity, measured during the first latitude scan ($G_\theta = (0.29 \pm 0.08)\%/degree$) (Heber *et al.*, 1996). Heber *et al.* (2008) pointed out that these gradients are much smaller than would be predicted without an enhanced perpendicular transport, and could conclude that the cause of this enahncement is present both in the A+ and A- polarity epochs.
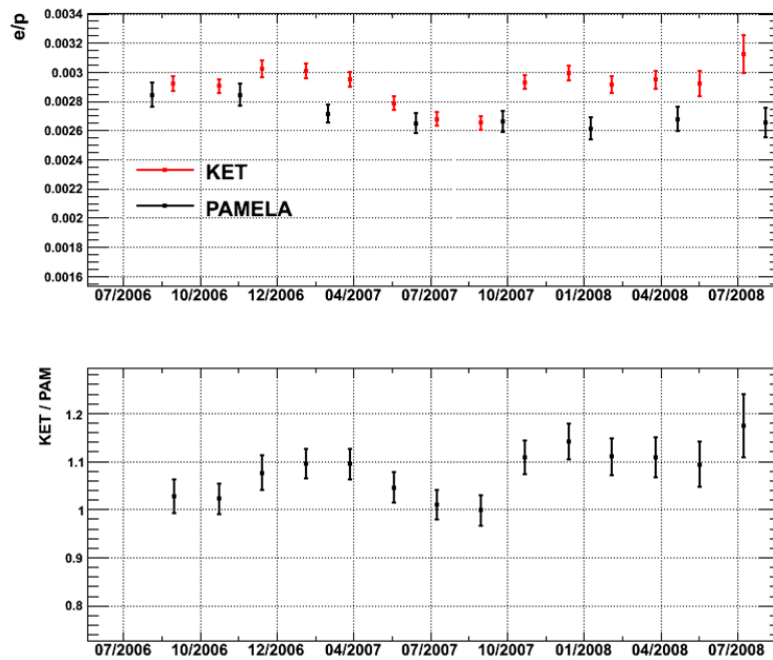
Figure (5.16)   *Top panel: e/p PAMELA and Ulysses-KET measures in time. The values have been normalized one to the other in August 2007, when the Ulysses spacecraft was approximately at latitude $0°$.*
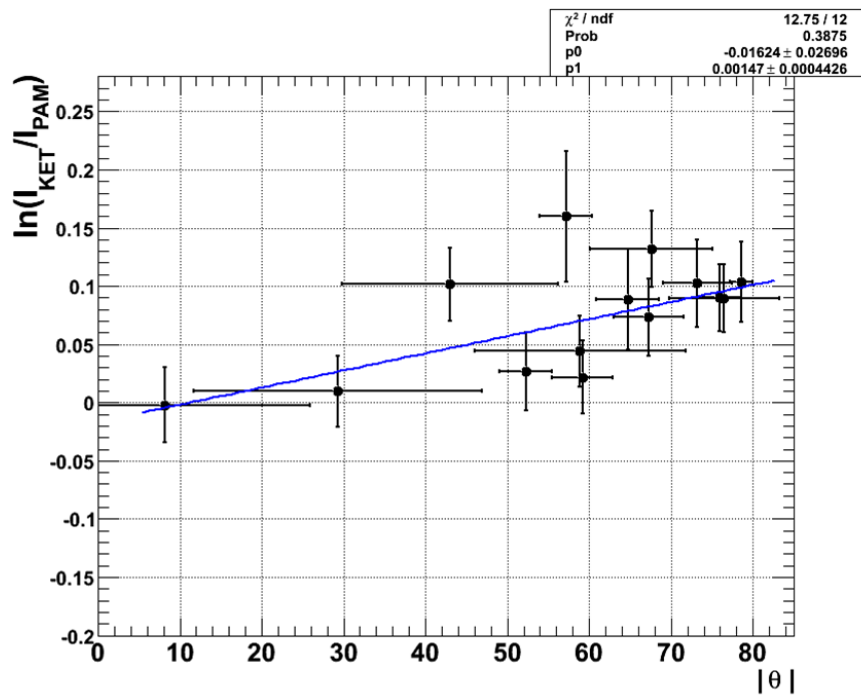
Figure (5.17)   *Measure of the electron $(e^+ + e^-)$ latitudinal gradient.*

Conclusions and perspectives

The PAMELA experiment, designed to perform accurate measurements of cosmic rays, has revealed antiprotons and positrons up to 100 GeV, providing important constraints for the existence of exotic processes and information about mechanisms of production, acceleration and propagation of CRs in the Galaxy. In this thesis, data at low energy, related to effects of solar modulation, have been analyzed and a new measurement of the lepton component of cosmic rays is presented. The analysis of data collected from July 2006 to December 2008 resulted in the measure of the the positron fraction in the energy range from 0.2 to 3.0 GeV and of the electron spectrum up to 20.0 GeV.

PAMELA was launched on June 15th 2006 in an elliptical quasi-polar orbit, and explores high latitude, low cutoff regions for a reasonable fraction of its livetime. The characteristics of its orbit, combined with the long flight duration, result in data distinguishing for the high statistics and precision respect to the existing measurements, and they allows to quantitatively evaluate the solar modulation effects, and in particular its charge-sign dependence.

The PAMELA data have been collected during an A- polarity solar minimum and found to be in agreement, within the error bars, with the less precise previous data from balloon experiments performed during the same polarity epochs, while they are significantly and systematically lower respect to data collected during the opposite polarity epoch.

The $e^+/(e^+ + e^-)$ results are in agreement with the trend predicted by drift models that calculate a suppression of the positron fraction in A- epochs related to charge dependent solar modulation effects. Low energy $\bar{p}/p$ PAMELA data support drift models as well. The precision of the reported data allows them to be used for a fine tuning of the model parameters which describe the propagation charged particles in the heliosphere.

With respect to the electron spectrum, the energy dependence of the particle intensity derived in this work is in good agreement with the results from previous experiments at high energy, where the influence of the solar modulation is less

prominent. At low energy the solar influence is clearly visible, making the spectrum deviate respect to a power law energy dependence. The PAMELA data have been compared with the theoretical expectations of drift models for A+ and A- solar minimum epochs, resulting in agreement with the calculated spectral shape at low energy. This data can be used to determine diffusion parameters by fitting them to models. Electrons are particularly suited to this scope since, being not affected by adiabatic cooling at low energy as protons, they respond directly to variations of the diffusion coefficients.

Moreover, thanks to the long duration of the mission and the high statistics collected, it was possible to compare the electron spectrum observed in 2006 and 2007; the comparison indicates the presence of an increase, with time, of the measured intensity below few GeV, that would be in line with the expectations in case of a decreasing solar modulation. The time-dependence of the PAMELA proton data confirm the observed trend. The investigation of any difference in the temporal variation of the low energy spectra between protons and electrons, in extent and shape, will be object of the future work. Of particular interest is the perspective to extend this kind of measure in time to eventually observe a rise in the e/p ratio, which is expected to occur when leaving the solar minimum toward the solar maximum and has been already measured during the previous solar cycle. Moreover, PAMELA can monitor in time the ratio e^-/e^+, allowing to disentangle effects due to charge sign from those arising in velocity differences for the same particle rigidity. The interest in this possibility of investigation constitutes one of the main reasons why the mission duration, initially scheduled to end by 2009, has been prolonged to 2011.

An other result presented in this thesis is about the comparison of the $(e^+ + e^-)/e^+$ ratio from PAMELA with the e/p ratio from Ulysses, which resulted in a first determination of the electron latitudinal gradients. A forthcoming work aims to combine the measurements of electron to proton ratio from the two spacecrafts, including the determination of the spatial distribution of galactic protons, to improve the obtained result on the electron gradients.

Publications

O. Adriani et al., *Observation of an anomalous positron abundance in the cosmic radiation*, Nature, vol. 458, pp. 607-609, (2009).

M. Boezio et al., *PAMELA and indirect dark matter searches*, New Journal of Physics, vol. 11, (2009).

O. Adriani et al., *Measurements of quasi-trapped electron and positron fluxes with PAMELA*, Journal of Geophysical Research, vol. 114, (2009).

V. Di Felice et al., *PAMELA observational capabilities of Jovian electrons*, Advances in Space Research vol. 41, Issue 12, pp. 2037-2042, (2007).

M. Casolino et al., *Magnetospheric and solar physics observations with the PAMELA experiment*, Nucl. Instrum. Methods Phys. Res., Sect. A, 588, pp. 243-246 (2008).

M. Casolino et al., *Launch of the space experiment PAMELA*, Advances in Space Research, vol. 42, pp. 455-466 (2008).

P. Papini et al., *In-flight performances of the PAMELA satellite experiment*, Nucl. Instrum. Methods Phys. Res., Sect. A, 588, pp. 259-266 (2008).

Presentations

M. Boezio, V. Di Felice on behalf of the PAMELA Collaboration, *Cosmic ray electrons and positrons measured by PAMELA during the A- magnetic solar minimum*, $31^{s}t$ International Cosmic Ray Conference, Lodz, Polonia, July 2009.

V. Di Felice, J. Gieseler, N. De Simone, on behalf of the Pamela and the Ulysses COSPIN/KET collaborations, *Pamela and Ulysses observations of 2.5 GV electron*

and protons during the recent solar minimum, 31st International Cosmic Ray Conference, Lodz, Polonia, July 2009.

V. Di Felice for the PAMELA Collaboration, *The positron fraction at low energy with the PAMELA space experiment and solar modulation effects*, 37th COSPAR 2008, Montreal, Canada , July 2008.

V. Di Felice for the PAMELA Collaboration, *Measurement of solar cosmic rays at 1 AU with PAMELA experiment*, 36th COSPAR 2006, Beijing, Cina, July 2006.

V. Di Felice, M. Casolino, N. De Simone, P. Picozza, *PAMELA observational capabilities of Jovian electrons*, 36th COSPAR 2006, Beijing, July 2006.

List of Figures

List of Tables

Bibliography

Adams F C, **Freese** K, **Laughlin** G, **Schwadron** N and **Tarle** G, **1997**. "Constraints on the Intergalactic Transport of Cosmic Rays". *Astrophys J* **491** 6–+.

Adriani O and **et. al.**, **2009**. "Measurements of quasi-trapped electron and positron fluxes with PAMELA". *Journal of Geophysical Research (Space Physics)* **114**(A13) 12218–+.

Adriani O *et al.*, **2009**. "Observation of an anomalous positron abundance in the cosmic radiation". *Nature* **458** 607–609.

Alcaraz J *et al.*, **2000**. "Leptons in near Earth orbit". *Physics Letters B* **484** 10–22.

Arkani-Hamed N, **Finkbeiner** D P, **Slatyer** T R and **Weiner** N, **2009**. "A theory of dark matter". *Phys Rev D* **79**(1) 015014–+.

Asaoka Y, **Shikaze** Y and **Abe** K e a, **2002**. "Measurements of Cosmic-Ray Low-Energy Antiproton and Proton Spectra in a Transient Period of Solar Field Reversal". *Physical Review Letters* **88**(5) 051101–+.

Atoyan A M, **Aharonian** F A and **Völk** H J, **1995**. "Electrons and positrons in the galactic cosmic rays". *Phys Rev D* **52** 3265–3275.

Bartol group website. "Bartol group". `http://neutronm.bartol.udel.edu/~clem/magtraj/`.

Barwick S W, **Beatty** J J and **Bower** C R e a, **1998**. "The Energy Spectra and Relative Abundances of Electrons and Positrons in the Galactic Cosmic Radiation". *Astrophysical Journal* **498** 779–+.

Barwick S W *et al.*, **1997**. *Astrophys J* **482** L191+.

Bergström L, **2009**. "Dark matter candidates". *New Journal of Physics* **11**(10) 105006–+.

Bergström L, **Bringmann** T and **Edsjö** J, **2008**. "New positron spectral features from supersymmetric dark matter: A way to explain the PAMELA data?" *Phys Rev D* **78**(10) 103520–+.

Bertone G, ed., **2009**. *Particle Dark Matter*. Cambridge University Press.

Bertone G, **Fornasa** M, **Taoso** M and **Zentner** A R, **2009**. "Dark matter annihilation around intermediate mass black holes: an update". *New Journal of Physics* **11**(10) 105016–+.

Bertone G, **Hooper** D and **Silk** J, **2005**. "Particle dark matter: evidence, candidates and constraints". *Phys. Rept* **405** 279–390.

Blasi P, **2009**. "Origin of the Positron Excess in Cosmic Rays". *Physical Review Letters* **103**(5) 051104–+.

Boezio M, **1998**. Ph.D. thesis, KTH, Stockholm.

Boezio M, **Carlson** P, **Francke** T and **et al.**, **2000**. "The Cosmic-Ray Electron and Positron Spectra Measured at 1 AU during Solar Minimum Activity". *Astrophysical Journal* **532** 653–669.

Boezio M, **Pearce** M, **Picozza** P and **et al.**, **2009**. "PAMELA and indirect dark matter searches". *New Journal of Physics* **11**(10) 105023–+.

Bogomolov A E, **Vasilyev** I G and **et al.**, **1990**. "New Antiproton Studies in the 2-5 GeV Range". In *International Cosmic Ray Conference*, vol. 3 of *International Cosmic Ray Conference*, pp. 288–+.

Bogomolov E A and **et al.**, **1979**. "a Stratospheric Magnetic Spectrometer Investigation of the Singly Charged Component Spectra and Composition of the Primary and Secondary Cosmic Radiation". In *International Cosmic Ray Conference*, vol. 1 of *International Cosmic Ray Conference*, pp. 330–+.

Bottino A, **Donato** F, **Fornengo** N and **Scopel** S, **2008**. "Interpreting the recent results on direct searches for dark matter particles in terms of relic neutralinos". *Phys Rev D* **78**(8) 083520–+.

Bruno A, **2009**. *Cosmic ray antiprotons measured in the PAMELA experiment*. Ph.D. thesis, Università degli Studi di Bari.

Burger R A, **1999**. "The Effect of Large Heliospheric Current Sheet Tilt Angles in Numerical Modulation Models: A Theoretical Assessment". In *International Cosmic Ray Conference*, vol. 7.

Burger R A, **2005**. "Cosmic-ray modulation and the heliospheric magnetic field". *Advances in Space Research* **35** 636–642.

Burger R A, **Hattingh** M and **Bieber** J W, **1997**. "The effect of magnetic helicity on the propagation of galactic cosmic rays". *Advances in Space Research* **19** 897–900.

Büsching I, **de Jager** O C, **Potgieter** M S and **Venter** C, **2008**. "A Cosmic-Ray Positron Anisotropy due to Two Middle-Aged, Nearby Pulsars?" *ApJL* **678** L39–L42.

Cane H V, **Wibberenz** G, **Richardson** I G and **von Rosenvinge** T T, **1999**. "Cosmic ray modulation and the solar magnetic field". *Geophysical Research Letters* **26** 565–568.

Chenette D L, **Conlon** T F and **Simpson** J A, **1974**. "Burst of relativistic electrons from Jupiter observed in interplanetary space with the time variation of the planetary rotation period." *Journal of Geophysical Research* **79** 3551–3558.

Cheng H, **Feng** J L and **Matchev** K T, **2002**. "Kaluza-Klein Dark Matter". *Physical Review Letters* **89**(21) 211301–+.

Cholis I, **Dobler** G, **Finkbeiner** D P, **Goodenough** L and **Weiner** N, **2008**. "The Case for a 700+ GeV WIMP: Cosmic Ray Spectra from PAMELA, Fermi and ATIC". *ArXiv:0811.3641* .

Cirelli M, **Kadastik** M, **Raidal** M and **Strumia** A, **2009**. "Model-independent implications of the e^+, e^-, anti-proton cosmic ray spectra on properties of Dark Matter". *Nuclear Physics B* **813** 1–21.

Clem J and **Evenson** P, **2004**. "Observations of cosmic ray electrons and positrons during the early stages of the A- magnetic polarity epoch". *Journal of Geophysical Research (Space Physics)* **109** 7107–+.

Clem J and **Evenson** P, **2009**. "Balloon-borne observations of the galactic positron fraction during solar minimum negative polarity". *Journal of Geophysical Research (Space Physics)* **114**(A13) 10108–+.

Clem J, **Evenson** P and **Heber** B, **2002**. "Cosmic electron gradients in the inner heliosphere". *Geophysical Research Letters* **29**(23) 230000–1.

Clem J M, **Clements** D P and **et al.**, **1996**. "Solar Modulation of Cosmic Electrons". *Astrophysical Journal* **464** 507–+.

Clem J M, **Evenson** P, **Huber** D, **Pyle** R, **Lopate** C and **Simpson** J A, **2000**. "Charge sign dependence of cosmic ray modulation near a rigidity of 1 GV". *Journal of Geophysical Research* **105** 23099–23106.

Clem J M and **Evenson** P A, **2002**. "Positron Abundance in Galactic Cosmic Rays". *Astrophysical Journal* **568** 216–219.

Cohen A G, **de Rujula** A and **Glashow** S L, **1998**. "A Matter-Antimatter Universe?" *Astrophysical Journal* **495** 539–+.

D. Lafferty G and **R. Wyatt** T, **1995**. "Where to stick your data points: The treatment of measurements within wide bins". *Nuclear Instruments and Methods in Physics Research A* **355** 541–547.

D'Agostini, G., **1995**. "A Multidimensional unfolding method based on Bayes' theorem". *Nucl Instrum Meth* **A362** 487–498.

Daugherty J K, **Hartman** R C and **Schmidt** P J, **1975**. "A measurement of cosmic-ray positron and negatron spectra between 50 and 800 MV". *Astrophysical Journal* **198** 493–505.

De Simone N. Private communication.

Delahaye T, **Lineros** R, **Donato** F, **Fornengo** N, **Lavalle** J, **Salati** P and **Taillet** R, **2009**. "Galactic secondary positron flux at the Earth". *Astron. Astrophys.* **501** 821–833.

Dolgov A D, **2008**. "Cosmic antimatter: models and observational bounds". *arXiv:0806.4554v3* .

Fanselow J L, **Hartman** R C, **Hildebrad** R H and **Meyer** P, **1969**. "Charge Composition and Energy Spectrum of Primary Cosmic-Ray Electrons". *Astrophysical Journal* **158** 771–+.

Ferreira S, **2002**. *The heliospheric transport of galactic cosmic rays and jovian electrons*. Ph.D. thesis, Potchefstroomse Universiteit vir Christelike Hor Onderwys, Potchefstroom, South Africa.

Ferreira S E S and **Potgieter** M S, **2004**. "Long-Term Cosmic-Ray Modulation in the Heliosphere". *Astrophysical Journal* **603** 744–752.

Fisk L A, **1996**. "Motion of the footpoints of heliospheric magnetic field lines at the Sun: Implications for recurrent energetic particle events at high heliographic latitudes". *Journal of Geophysical Research* **101** 15547–15554.

Garcia-Munoz M, **Meyer** P, **Pyle** K R and **Simpson** J A, **1987**. "The Dependence of Solar Modulation on the Sign of the Cosmic Ray Particle Charge : Further Study of a 22 Year Solar Magnetic Cycle". In *International Cosmic Ray Conference*, vol. 3 of *International Cosmic Ray Conference*, pp. 303–+.

Gieseler J, **Heber** B, **Dunzlaff** P and **et al.**, **2008**. "The radial gradient of galactic cosmic rays: Ulysses KET and ACE CRIS Measurements". In *International Cosmic Ray Conference*, vol. 1 of *International Cosmic Ray Conference*, pp. 571–574.

Gleeson L J and **Axford** W I, **1968**. "Solar Modulation of Galactic Cosmic Rays". *Astrophysical Journal* **154** 1011–+.

Golden R L and **et al.**, **1987**. "Observation of cosmic ray positrons in the region from 5 to 50 GeV". *Astron. Astrophys.* **188** 145–154.

Golden R L and **et al.**, **1994**. "Observations of cosmic-ray electrons and positrons using an imaging calorimeter". *Astrophysical Journal* **436** 769–775.

Golden R L, **Horan** S and **et al**, **1979**. "Evidence for the existence of cosmic-ray antiprotons". *Physical Review Letters* **43** 1196–1199.

Goodenough L and **Hooper** D, **2009**. "Possible Evidence For Dark Matter Annihilation In The Inner Milky Way From The Fermi Gamma Ray Space Telescope". *ArXiv:0910.2998* .

Grimani C, **2007**. "Constraints on cosmic-ray positron excess and average pulsar parameters". *Astron. Astrophys.* **474** 339–343.

Grimani C, **2009**. "Origin of cosmic-ray positrons". In *International Cosmic Ray Conference*, International Cosmic Ray Conference.

Hartman R C and **Pellerin** C J, **1976**. "Cosmic-ray positron and negatron spectra between 20 and 800 MeV measured in 1974". *Astrophysical Journal* **204** 927–933.

Heber B, **Droege** W, **Ferrando** P and **et al.**, **1996**. "Spatial variation of 40MeV/n nuclei fluxes observed during the ULYSSES rapid latitude scan". *Astron. Astrophys.* **316** 538–546.

Heber B, **Gieseler** J and **et al.**, **2008**. "Latitudinal Gradients of Galactic Cosmic Rays during the 2007 Solar Minimum". *Astrophysical Journal* **689** 1443–1447.

Heber B, **Kopp** A, **Gieseler** J and **et al.**, **2009**. "Modulation of Galactic Cosmic Ray Protons and Electrons During an Unusual Solar Minimum". *Astrophysical Journal* **699** 1956–1963.

Heber B and **Marsden** R G, **2001**. "Cosmic Ray Modulation over the Poles at Solar Maximum: Observations". *Space Science Reviews* **97** 309–319.

Heber B and **Potgieter** M S, **2006**. "Cosmic Rays at High Heliolatitudes". *Space Science Reviews* **127** 117–194.

Heber B, **Wibberenz** G, **Potgieter** M S and **et al.**, **2002**. "Ulysses Cosmic Ray and Solar Particle Investigation/Kiel Electron Telescope observations: Charge sign dependence and spatial gradients during the 1990-2000 A > 0 solar magnetic cycle". *Journal of Geophysical Research (Space Physics)* **107** 1274–+.

Hofverberg P, **2009**. *A New Measurement of Low Energy Antiprotons in the Cosmic Radiation*. Ph.D. thesis, KTH, Stockholm.

Hooper D, **Blasi** P and **Dario Serpico** P, **2009**. "Pulsars as the sources of high energy cosmic ray positrons". *Journal of Cosmology and Astro-Particle Physics* **1** 25–+.

Ibe M, **Murayama** H, **Shirai** S and **Yanagida** T T, **2009**. "Cosmic Ray Spectra in Nambu-Goldstone Dark Matter Models". *ArXiv:0908.3530* .

Jokipii J R, **Levy** E H and **Hubbard** W B, **1977**. "Effects of particle drift on cosmic-ray transport. I - General properties, application to solar modulation". *Astrophysical Journal* **213** 861–868.

Jungman G, **Kamionkowski** M and **Griest** K, **1996**. "Supersymmetric dark matter". *Phys. Rept* **267** 195–373.

Kane G, **Lu** R and **Watson** S, **2009**. "PAMELA Satellite Data as a Signal of Non-Thermal Wino LSP Dark Matter". *ArXiv:0906.4765* .

Komatsu E and **et al.**, **2009**. "Five-Year Wilkinson Microwave Anisotropy Probe Observations: Cosmological Interpretation". *Astrophys. J. Suppl.* **180** 330–376.

Langner U W, **de Jager** O C and **Potgieter** M S, **2001**. "On the local interstellar spectrum for cosmic ray electrons". *Advances in Space Research* **27** 517–522.

Langner U W and **Potgieter** M S, **2004**. "Effects of the solar wind termination shock on charge-sign dependent cosmic ray modulation". *Advances in Space Research* **34** 144–149.

Langner U W, **Potgieter** M S, **Fichtner** H and **Borrmann** T, **2006**. "Modulation of anomalous protons: Effects of different solar wind speed profiles in the heliosheath". *Journal of Geophysical Research (Space Physics)* **111** 1106–+.

Lavalle J, **Yuan** Q, **Maurin** D and **Bi** X, **2008**. "Full calculation of clumpiness boost factors for antimatter cosmic rays in the light of ΛCDM N-body simulation results. Abandoning hope in clumpiness enhancement?" *Astron. Astrophys.* **479** 427–452.

Lineros R, **2009**. "Galactic positrons and electrons from astrophysical sources and dark matter". *ArXiv:0910.2671* .

Maurin D, **Taillet** R and **Donato** F, **2002**. "New results on source and diffusion spectral features of Galactic cosmic rays: I B/C ratio". *Astron. Astrophys.* **394** 1039–1056.

McComas D J, **Gosling** J T and **Skoug** R M, **2000**. "Ulysses observations of the irregularly structured mid-latitude solar wind during the approach to solar maximum". *Geophysical Research Letters* **27** 2437–2440.

Moskalenko I V and **Strong** A W, **1998**. "Production and Propagation of Cosmic-Ray Positrons and Electrons". *Astrophysical Journal* **493** 694–+.

Moskalenko I V, **Strong** A W, **Ormes** J F and **Potgieter** M S, **2002**. "Secondary Antiprotons and Propagation of Cosmic Rays in the Galaxy and Heliosphere". *Astrophysical Journal* **565** 280–296.

Ndiitwani D C, **Ferreira** S E S, **Potgieter** M S and **Heber** B, **2005**. "Modelling cosmic ray intensities along the Ulysses trajectory". *Annales Geophysicae* **23** 1061–1070.

OMNI M website. "OMNI spacecraft data". `http://cohoweb.gsfc.nasa.gov/form/omni_m.html`.

PAMELA official web page. "PAMELA official web page". `http://pamela.roma2.infn.it`.

Parker E N, **1964**. "The Scattering of Charged Particles by Magnetic Irregularities". *Journal of Geophysical Research* **69** 1755–1758.

Parker E N, **1965**. "The passage of energetic charged particles through interplanetary space". *Planetary and Space Science* **13** 9–+.

Paterno M, **2004**. "Calculating efficiencies and their uncertainties" FERMILAB-TM-2286-CD.

Pato M, **Pieri** L and **Bertone** G, **2009**. "Multi-messenger constraints on the annihilating dark matter interpretation of the positron excess". *ArXiv:0905.0372* .

PDG. "Particle Data Group". `http://pdg.lbl.gov/`.

Pei e a C, **2009**. "On a stochastic approach to cosmic-ray modulation". In *International Cosmic Ray Conference*, International Cosmic Ray Conference.

Percossi, G., **2005**. *PAMELA data analysis: a bayesian unfolding method*. Ph.D. thesis, University of Rome Tor Vergata.

Picozza P *et al.*, **2007**. *Astroparticle Physics* **27** 296–315.

Pospelov M and **Ritz** A, **2009**. "Astrophysical signatures of secluded dark matter". *Physics Letters B* **671** 391–397.

Potgieter M, **2008**. "Solar cycle variations and cosmic rays". *Journal of Atmospheric and Solar-Terrestrial Physics* **70** 207–218.

Potgieter M S, **Burger** R A and **Ferreira** S E S, **2001**. "Modulation of Cosmic Rays in the Heliosphere From Solar Minimum to Maximum: a Theoretical Perspective". *Space Science Reviews* **97** 295–307.

Profumo S, **2008**. "Dissecting cosmic-ray electron-positron data with Occam's Razor: the role of known Pulsars". *ArXiv:0812.4457* .

Rastoin C, **Ferrando** P and **et al.**, **1996**. "Time and space variations of the Galactic cosmic ray electron spectrum in the 3-D heliosphere explored by Ulysses." *Astron. Astrophys.* **307** 981–995.

Ricciarini S B. Private communication.

Rossi B and **Greisen** K, **1941**. "Cosmic-Ray Theory". *Rev Mod Phys* **13**(4) 240–309.

Sakharov A, **1967**. "Violation of CP invariance, C asymmetry and baryon asymmetry in the universe". *JEPT Lett* **5** 24.

Serpico P D, **2009**. "Possible causes of a rise with energy of the cosmic ray positron fraction". *Phys Rev D* **79**(2) 021302–+.

Shaviv N J, **Nakar** E and **Piran** T, **2009**. "Inhomogeneity in Cosmic Ray Sources as the Origin of the Electron Spectrum and the PAMELA Anomaly". *Physical Review Letters* **103**(11) 111302–+.

Sitenko a T V K A G, ed., **1972**. *Lektsii po teorii iadra*. Edizioni Mir.

Smith E J, **2001**. "The heliospheric current sheet". *Journal of Geophysical Research* **106** 15819–15832.

Sullivan J D, **1971**. "Cosmic-Ray Theory". *Nuclear instruments and methods* **95** 5–11.

Tuska E, **Evenson** P and **Meyer** P, **1991**. "Solar modulation of cosmic electrons - Evidence for dynamic regulation". *ApJL* **373** L27–L30.

Wigmans R, ed., **2000**. Oxford University Press.

WSO website. "Wilcox Solar Observatory". http://wso.stanford.edu/.

Yüksel H, **Kistler** M D and **Stanev** T, **2009**. "TeV Gamma Rays from Geminga and the Origin of the GeV Positron Excess". *Physical Review Letters* **103**(5) 051101–+.